THE KÖSTER'S INTERFEROMETER FOR GAUGE BLOCK LENGTH MEASUREMENTS

A THESIS SUBMITTED TO
THE GRADUATE SCHOOL OF NATURAL AND APPLYIED SCIENCES
OF
MIDDLE EAST TECHNICAL UNIVERSITY

BY

DAMLA ŞENDOĞDU ÇUHADAR

IN PRACTICAL FULFILLMENT OF THE REQUIREMENTS
FOR
THE DEGREE OF DOCTOR OF PHILOSOPHY
IN
PHYSICS

SEPTEMBER 2007

Approval of the thesis:

THE KÖSTER'S INTERFEROMETER FOR GAUGE BLOCK LENGTH MEASUREMENTS

submitted by **DAMLA ŞENDOĞDU ÇUHADAR** in partial fulfillment of the requirements for the degree of **Doctor of Philosophy in Physics Department, Middle East Technical University** by,

Prof. Dr. Canan Özgen _____
Dean, Graduate School of **Natural and Applied Sciences**

Prof. Dr. Sinan Bilikmen _____
Head of Department, **Physics**

Assoc. Prof. Dr. Akif Esendemir _____
Supervisor, **Physics Dept., METU**

Examining Committee Members:

Prof. Dr. Ali Gökmen _____
Chemistry Dept., METU

Assoc. Prof. Dr. Akif Esendemir _____
Physics Dept., METU

Prof. Dr. Mehmet Parlak _____
Physics Dept., METU

Assoc. Prof. Dr. Serhat Çakır _____
Physics Dept., METU

Assoc. Prof. Dr. Selim Osman Selam _____
Astronomy and Space Science Dept., Ankara University

Date:

I hereby declare that all information in this document has been obtained and presented in accordance with academic rules and ethical conduct. I also declare that, as required by these rules and conduct, I have fully cited and referenced all material and results that are not original to this work.

Name, Last name: Damla, Şendoğdu Çuhadar

Signature :

ABSTRACT

THE KÖSTER'S INTERFEROMETER FOR GAUGE BLOCK LENGTH MEASUREMENTS

Şendoğdu Çuhadar, Damla
Ph.D., Department of Physics
Supervisor: Assoc. Prof. Dr. Akif Esendemir

September 2007, 128 pages

This thesis describes the design, construction and testing of a new interferometer for the absolute measurement of length standards. It is assumed that this study mainly formed of three parts. Firstly, it starts with an introduction to the subject of length standards and length measurement by interferometry. The design of the new interferometer is given in detail, including the stable lasers used as light sources, fiber, optical and opto-mechanical components.

In the second part of this study, the mechanical construction of the interferometer chamber is presented with temperature stabilization and controlling system. The temperature variations inside the chamber at different points in air and along the surface of the length standard are given. After that, the techniques for measurement of the refractive index of the air inside the interferometer chamber are summarized.

In the last part of the thesis, a review of fringe analysis techniques is given,

with an emphasis on 5 position phase-stepping algorithms. The data processing of images digitized in the interferometer is described, including the techniques developed for discontinuity removal and surface fitting. The measurement of the variation in length and flatness of the measuring faces of the length standards is described and the experimental results are given. The automated method of multiple wavelength-exact fractions is used to combine phase measurements at three wavelengths to allow accurate calculation of the length of the length standards. The experimental results are given for length standards. The uncertainty budget of whole system is calculated and presented in a table.

Keywords: Köster interferometer, absolute length measurement, temperature controlling, refractive index of air, fringe analysis.

ÖZ

KÖSTER İNTERFEROMETRESİ İLE MASTAR BLOKLARIN
UZUNLUK ÖLÇÜMLERİ

Şendoğdu Çuhadar, Damla
Ph.D., Department of Physics
Supervisor: Doç. Dr. Akif Esendemir

September 2007, 128 sayfa

Bu tez, uzunluk standartlarının mutlak ölçümleri için hazırlanan yeni bir interferometre sisteminin tasarımı, yapı ve testini içermektedir. Bu çalışmanın temel olarak üç kısımdan oluştuğu düşünülebilir. Öncelikle tez, uzunluk standartlarının ve interferometrik yöntemle yapılan uzunluk ölçümlerinin anlatıldığı giriş bölümü ile başlamaktadır. İnterferometrenin tasarımı, kaynak olarak kullanılan kararlı lazerler, fiberler, optiksel ve opto mekaniksel bileşenlerle beraber detaylı olarak anlatılmıştır.

Çalışmanın ikinci kısmında, interferometre kapalı kutusunun mekanik yapısı, sıcaklık kontrol ve stabilizasyon sistemi ile beraber verilmiştir. Kutu içindeki farklı noktalardaki ve uzunluk standardının yüzeyindeki sıcaklık dağılım değerleri sunulmuştur. İnterferometre içindeki havanın kırılma indeksinin direkt hesaplama ve refraktometre ile ölçülme yöntemleri anlatılmış ve karşılaştırılmıştır.

Son olarak, girişim desenleri analiz teknikleri, 5-pozisyonlu faz adımlama algoritması ile anlatılmıştır. İnterferometrede dijital hale getirilen görüntülerin veri işleme prosesleri süreksizlik giderme ve yüzey fit etme teknikleri ile beraber anlatılmıştır. Uzunluk standartlarının ölçüm yüzeylerindeki düzlemsellik ve uzunluktaki değişim (paralellik) ölçümleri tanımlanmış ve deneysel sonuçları verilmiştir. Çok dalgaboylu otomatik metot üç dalgaboyunu da içine alacak ve uzunluk standardının uzunluğunu hesaplamamızı sağlayacak faz ölçümlerinin gerçekleştirilmesinde kullanılmıştır. Deney sonuçları, uzunluk standartları için verilmiştir. Belirsizlik bütçesi tüm sistem için hesaplanmış ve bir tabloda sunulmuştur.

Anahtar Kelimeler: Köster interferometresi, mutlak uzunluk ölçümleri, sıcaklık kontrolü, havanın kırılma indeksi, girişim deseni analizi

To My Parents and Family

ACKNOWLEDGMENTS

I would like to express my sincere gratitude to Dr. Ramiz Hamid the head of Wavelength Standards Laboratory for allowing me to submit this work for my Doctorate thesis and for letting me study at UME (National Metrology Institute).

I would like to thank my supervisor, Assoc. Prof. Dr. Akif Esendemir for his guidance and help throughout this work.

I intensely acknowledge my colleagues, especially Cihangir Erdoğan for his extensive help, encouragement, discussions and suggestions throughout this thesis.

A special word of thanks goes to H.İbrahim Emre for realizing mechanical structure of the interferometer chamber.

I also wish to thank my family, Kerem and Haluk Şendoğdu for their patience and worthy supports during my entire study.

TABLE OF CONTENTS

ABSTRACT……..…….. iv
ÖZ…….. vi
ACKNOWLEDGMENTS…….……ix
TABLE OF CONTENTS…….….. x
LIST OF FIGURES……..…….……. xiv
CHAPTERS
1. INTRODUCTION 1
1.1 Traceability Chain of Gauge Block Length Measurements..... 1
1.1.1 The Brief History of the Definition of the Meter…….. 2
1.1.2 The Primary Length Standards and Their Traceability……..……... 4
1.1.3 The Secondary Length Standards……..5
1.2 Definition of Metrology…….……...…... 6
1.3 Contents of the Thesis……...…... 7
2. LENGTH MEASURING INTERFEROMETERS 9
2.1 The Design of Michelson Interferometer……...…..9
2.2 The Design of Köster Interferometer……... 12
2.3 Length Calculation of the Gauge Block……... 13
3. THE DESIGN OF THE INTERFEROMETER 16
3.1 Lasers……..…. 17
3.1.1 He-Ne/I_2 Laser..... 17
3.1.2 Nd:YAG/I_2 Laser……...……... 18
3.1.2.1 Nd:YAG Laser Theory…….. 18
3.1.2.2 Nd:YAG/I_2 Laser (532/1064 nm) Optical Frequency Standards……20
3.1.3 ECDL/Rb Laser……...……21

3.2 Fiber, Optical and Opto-Mechanical Components ……..…….... 24
3.2.1 Fiber Cables, Laser to Fiber Couplers and WDM Coupler.....24
3.2.2 Attenuations in the Fiber Components……..26
3.2.3 Collimating Telescope……...……... 29
3.2.4 De-Collimating Telescope …….…….……...….. 30
3.2.5 Köster's Interference Double Prisms…… 32
3.2.6 Reference Mirrors……...…….. 33
3.2.7 PZT and DPT Controlled Stages and Optical Mounts…….. 34
4. TEMPERATURE MEASUREMENT SYSTEM OF INTERFEROMETER 36
4.1 The Importance of Temperature Measurement in Interferometer...…...… 36
4.2 The Surface Temperature Measurements……...……...…….. 37
4.2.1 The Factors Effecting Surface Temperature Measurements……. 37
4.2.2 The Main Types of the Surface Thermometers…….38
4.2.3 The Surface Thermometers in Gauge Block Temperature Measurements……...……..... 39
4.3 Temperature Measurement System in UME-Köster Interferometer……40
4.3.1 The Construction of the Thermistors ……..……. 40
4.3.2 The Places of the Thermistors in the Interferometer…..…..…….41
4.3.3 The Measurement Principle and Calibration Techniques of Thermistors……...…… 43
4.3.4 Thermostat of the Köster Interferometer.…….…..…..…….44
4.4 The Results of Temperature Measurements……..….. 46
5. REFRACTIVE INDEX OF AIR 54
5.1 Introduction …….……...……54
5.2 The Calculation of Refractive Index of Air by Using Edlén Equations……...…...55
5.2.1 The Original and Modified Edlén Equations…..…….. 55
5.2.1.1 The Original Edlén Equations……55
5.2.1.2 Modification for Water Vapour and Conversion to the SI System…… 56
5.2.1.3 Modification for CO_2 and Application of ITS-90 Temperature Scale……...…….. 57
5.2.1.4 Modification for Wavelengths over Visible Range……...… 58

5.2.1.5 Modification for Compressibility……..... 58
5.2.1.6 The Result Modified Edlèn's Equations…….……..... 58
5.2.2 The Experiment Results for Edlèn's Equations..…….. 59
5.3 The Measurement Of Refractive Index Of Air By Using Refractometer.... 61
5.3.1 The Design of the Refractometer……...…….. 61
5.3.2 The Measurement Method ……..……...……...…….. 62
6. DATA PROCESSING 67
6.1 Interferogram Analysis…...……..…..…. 67
6.1.1 Interference Fringes and Phase Calculation …...…….. 67
6.1.2 Phase Measurement Methods……...…...……..68
6.2 Phase Stepping Interferometry (PSI)……...…….…….…. 68
6.2.1 Five-Frame Technique……..……...…...…….. 68
6.2.2 Removal of Phase Ambiguities….……...…...…….. 69
6.2.3 Phase Unwrapping Method.…….……...…...…….. 70
6.3 Experiment……...… 72
6.3.1 Theoretical Interference Fringes..……...…...…….. 72
6.3.2 Experimental Interference Fringes……...…...…….. 76
6.3.2.1 13 mm Gauge Block ……..……...… 76
6.3.2.2 3D Profile for Central Part of the 13 mm Gauge Block…..... 78
6.3.2.3 3D Profile for Whole Surface of the 13 mm Gauge Block… 81
6.3.2.4 Flatness and Variation in Length Measurements……... 84
6.3.3 Multiple Wavelength Calculation..……...…...…….. 86
6.3.4 The Flow Diagram of Data Processing…...…...…….. 91
7. UNCERTAINTY OF MEASUREMENTS 93
7.1 The Uncertainty Calculations……..…… 93
7.1.1 The Combined Uncertainty ……...…...…… 93
7.1.2 The Expanded Uncertainty ……...……94
7.1.3 The Uncertainties Due to Length Dependence and End Effects..… 94
7.1.4 The Model Equation…….....… 95
7.2 Uncertainty Evaluation……...……...…….....… 96
7.2.1 Uncertainty Evaluation of ℓ_{fit} …...……...… 96

7.2.2 Uncertainty Evaluation of ℓ_t ……..……...… 98

7.2.2.1 Uncertainty in the Thermal Expansion Coefficient …….. 98

7.2.2.2 Uncertainty in the Gauge Block Temperature Measurement 99

7.2.3 Uncertainty Evaluation of ℓ_n …...……..… 99

7.2.3.1 The Experiment Results for Edlen and Refractometer…….. 102

7.2.4 Uncertainty Evaluation of ℓ_v …...……..… 103

7.2.5 Uncertainty Evaluation of ℓ_Ω …...……...… 105

7.2.6 Uncertainty Evaluation of ℓ_ϕ …...……...… 105

8. CONCLUSION and DISCUSSION 107

REFERENCES 111

APPENDICES

A. DETAILED TECHNICAL PROPERTIES OF THE INSTRUMENT USED IN INTERFEROMETER ……... 115

B. SOME PICTURES OF UME (National Metrology Institute) HOME MADE KOSTER INTERFEROMETER……. 118

C. PUBLICATIONS……..…….. 120

LIST OF FIGURES

Figure 1.1 Traceability chain for length measurements 2

Figure 1.2 The schematic diagram of (a) gauge block and (b) length bar……5

Figure 2.1 The Michelson interferometer in schematic diagram…….… 10

Figure 2.2 The schematic diagram of Twyman- Green interferometer for length measurement of gauge blocks ……..…….. 12

Figure 2.3 The schematic diagram of Kösters interferometer …..……...13

Figure 2.4 The schematic diagram of reflections from the surfaces of the platen and gauge block ……..13

Figure 2.5 The schematic diagram of the exact and fractional multiples of *λ/2* through the length of the gauge block……..14

Figure 2.6 The schematic diagram of the interferogram with *a* and *b* values. 15

Figure 3.1 The schematic diagram of the interferometer with optical and opto-mechanical parts ……..…… 16

Figure 3.2 Energy levels in the Nd:YAG laser ……19

Figure 3.3 The schematic diagram of Nd:YAG laser in our experiment. The laser has two outputs as visible (532 nm) and IR (1064 nm)…… 20

Figure 3.4 The schematic diagram of UME Nd:YAG Laser Optical Frequency Standard……21

Figure 3.5 The schematic diagram of the External Cavity Diode Laser (ECDL)…….. 23

Figure 3.6 WDM coupler in schematic diagram.…… 25

Figure 3.7 The schematic diagram of the laser beam's paths from lasers to the output of the WDM coupler's output fiber. A, B, C, D and E points corresponds to the points where the power of the laser beam calculated. (778 nm laser is not shown in the figure)…… 27

Figure 3.8 The schematic diagram of inside the collimating telescope……...29

Figure 3.9 The schematic diagram of inside the de-collimating telescope….. 31

Figure 3.10 The Köster's double prism …….. 32

Figure 3.11 The placements of the reference mirrors at the reference arm of the interferometer ……...33

Figure 3.12 The placements of PZT stages …… 35

Figure 4.1 The schematic diagrams of the main types of the surface Thermometers……38

Figure 4.2 The schematic figures of air and surface thermistors. 1) 4 pieces of copper wires, 2) Al cap, 3) polyamide, 4) 2 Nickel wires with diameter of 0,2 mm, 5) epoxy glue, 6) glass sheath, 7) the layer of thermo conductive paste, 8) copper plate covered by silver, 9) stainless steel sheath, 10) thermistor sensitive element. (The diagram is not in scale)……41

Figure 4.3 The placements of the airy points and surface temperatures of the 1-meter gauge block. L; length of the gauge block. A_1 and A_2 airy points. The two surface thermistors placed at the airy points. B_1 and B_2; placements of the other two surface thermistors at points 10 cm away from the airy points ……42

Figure 4.4 The cross section of the main body and cover part including Aluminum boxes, isolation materials, Nyloil and copper pipes (the diagram is not to scale)……...45

Figure 4.5 The temperature readings from all thermistors (the first four ones are surface thermistors whereas the other six ones are air thermistors) at about 20 ^{0}C for (a) about 20 hours, (b) about 2 hours. The temperature fluctuations of all thermistors remains in the range of 2 mK……...47

Figure 4.6 The temperature readings from all thermistors (the first four ones are surface thermistors whereas the other six ones are air thermistors) at about 15 ^{0}C for about 15 hours. The temperature fluctuations of all thermistors remains in the range of 9 mK……. 48

Figure 4.7 (a) The placements of the surface thermistors for examining the temperature difference of upper and lower parts of the gauge block, (b) the results of the temperature measurements. The temperature difference, which corresponds to the temperature gradient of upper and lower parts of the block, between the sensors (t1and t3, t2 and t4) is smaller than 0.5 mK..50

Figure 4.8 (a) The placements of the surface thermistors over the gauge block with the platen for influence of the platen to the temperature gradient of the block, (b) the temperature measurement results at 20 ^{0}C and (c) at 15 ^{0}C. The difference of

the measured temperature values at airy points in the experiment at 20 °C or 15 °C with or without platen is about 2 mK…… 51

Figure 4.9 (a) The temperature data for one thermistor at 20 ^{0}C for about 7 hours (b) the histogram graph of the measurement (c) the stability graph of Allan variance analysis……..… 53

Figure 5.1 (a) The refractive index, (b) the pressure, (c) the temperature and (d) the humidity of the air inside of the chamber for about 2 hours…….. 61

Figure 5.2 The placement of refractometer inside of the interferometer…….62

Figure 5.3 (a) The schematic diagram of the refractometer in more detail (attached windows are not shown here) and (b) the interference fringes due to the refractometer (the fringes due to the gauge block is not shown here)…… 64

Figure 5.4 The output signals detected by a voltmeter when the fringes were passing…… 65

Figure 5.5 The output signals detected by voltmeter for the first 750 data. The data points in the graphs correspond to the voltmeter readings. Each peak corresponds to one passing fringes……65

Figure 5.6 The output signals detected by voltmeter for the last about 1500 data. The data points in the graphs correspond to the voltmeter readings. Each peak corresponds to one passing fringes. 66

Figure 6.1 (a) Example of a phase distribution having discontinuities that are due to the principal-value calculation; (b) offset phase distribution for correcting the discontinuities in (a); (c) continued profile of the phase distribution. The y axis is normal to the figure.. ……..……..71

Figure 6.2 The examples of theoretic interferograms correspond to different surface shapes. The upper parts represents 2D cross-sections of the surfaces, the lower parts represents the possible interference fringes correspond to these cross sections. (a) Flat surface (i.e. gauge block), (b) convex surface ..…… 72

Figure 6.3 The examples of theoretic interferograms corresponds to different number of the fringes in one image. (a) Two fringes (b) Six fringes (c) Ten fringes…… 73

Figure 6.4 The examples of five frames for five step phase stepping method (a) ϕ_R=0 (0^0), (b) $\pi/2$ (90^0), (c) π (180^0), (d) $3\pi/2$ (270^0), and (e) 2π (360^0). The images in first column represent interferograms obtained by theoretically; the figures in second column represents the 3D intensity profiles respectively……74

Figure 6.5 The calculated phase (ϕ), (a) for between -90^0 and 90^0 (b) for between 0^0 and 360^0……..…… 75

Figure 6.6 The phase map corresponds to gauge block and platen surface… 76

Figure 6.7 The images of interference fringes (a) ECDL/Rb (780 nm), (b) He-Ne/I_2 Laser (633 nm) (c) Nd:YAG/I_2 Laser (532 nm)……77

Figure 6.8 The interference fringes for five steps by using He-Ne/I_2 laser and by applying "Phase Stepping Method". (a)0^0 (0), (b)90^o ($\pi/2$), (c)80^0 (π), (d)270^0 ($3\pi/2$) and (e)360^0 (2π)……...78

Figure 6.9 3D phase graphics obtained from the frames by using He-Ne/I2 lasers. They cover the platen and the gauge block. (a) between -$\pi/2$ and $\pi/2$, (b) 0 and 2π, (c) 0^0 and 360^0…….. 79

Figure 6.10 2D picture of 3D phase values after changing to intensity Values…….79

Figure 6.11 3D profile of gauge block and platen after phase unwrapping….. 80

Figure 6.12 (a) The image of intensity values corresponds to one step for 633 nm (b) The phase values of the fringes as intensity image for 633 nm wavelength after phase stepping method.....…… 81

Figure 6.13 3D profile of block and platen. Concaveness is seen…….82

Figure 6.14 Fitted surface to the left part of the platen…… 83

Figure 6.15 Subtracting (Figure 6.13) form (Figure 6.14). Tilt removed. However concaveness is observed. …… 83

Figure 6.16 3D profile of the gauge block measurement surface……..84

Figure 6.17 Deviation fd from flatness……..85

Figure 6.18 Variation in Length. Nominal length l_n; central length l_c; variation v with f_o and f_u; limit deviations t_e for the length at any point, proceeding from the nominal length…… 86

Figure 6.19 The wavelength intervals for one laser. The effective range is $\lambda/2$……..…… 87

Figure 6.20 The wavelength intervals for two lasers. The effective range is 1.67 µm……..…….89

Figure 7.1 The variation in length and flatness properties of a gauge block. The effect of variation in length is larger than the effect of flatness for central point length measurement (for small angles, $tan\ \alpha = sin\ \alpha$)……104

Figure 8.1 The comparison graph of the measurement results between UME-Köster Interferometer and NPL-TESA GBI..... 108

CHAPTER 1

INTRODUCTION

In this study an interferometer has been designed to measure the lengths of the gauge blocks. Gauge block calibration (length measurement) is important for both national metrology institutes and calibration laboratories. Besides the calibration services, such measurements give rise to research activities towards more accurate measurements [1].

1.1 Traceability Chain of Gauge Block Length Measurements

The traceability chain for length measurements is seen in figure 1.1 [2]. The definition of the meter is placed at the head of this chain. The meter is *the length of the path traveled by light in vacuum during a time interval of 1/299 792 458 of a second*. This definition of the meter allows the SI unit of length to be reproduced in any laboratory with high accuracy [3]. The meter is realized at UME (National Metrology Institute of Turkey) as a wavelength of a HeNe (Helium-Neon) laser stabilized to a saturated absorption in I_2 (iodine) molecules at 632, 991 212 6 nm. Thus, at the second row of the chain the stabilized laser is placed and it represents also the primary standard of length.

At the third row of the table, the interferometers represent high accuracy length measurements of the blocks. The subject of this thesis is exactly placed occurred at this stage. The blocks are measured in terms of the wavelength emitted by the Iodine

stabilized laser; they can then be used to calibrate the lengths of other standard through comparison, i.e. micrometer or can be used to verify the performance of length measurements (CMM-Coordinate Measuring Machine).

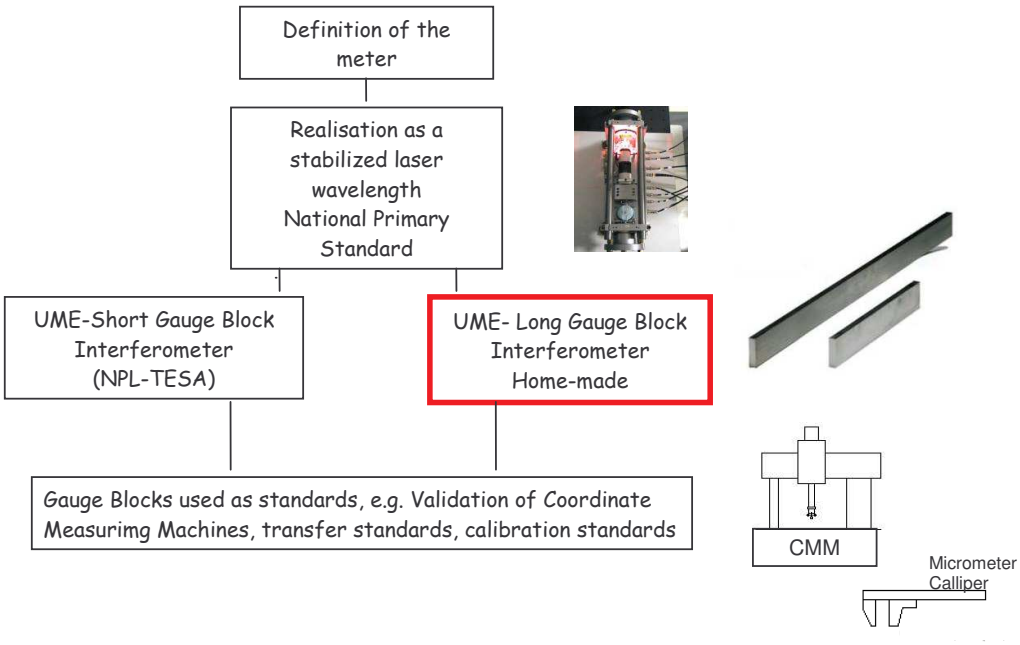

Figure 1.1 Traceability chain for length measurements

1.1.1 The Brief History of the Definition of the Meter

For the first definition of meter corresponds to a time of last decades of 19th century, two distinct major length systems were used. The metric length unit was the meter defined as 1/ 10.000.000 of the great arc from the pole to the equator, through Paris. The English system of units was based on a yard, another artifact standard.

These artifact standards were used for over 150 years. However, the length of these materials changes with time. For example, it was found that the British yard standard was slightly unstable by repeated measurements. The table 1.1 shows this instability for the British inch (1/35 yard).

Table 1.1 The instability of the British inch between the years of 1895 and 1947

1895	25.399978
1922	25.399956
1932	25.399950
1947	25.399931

In 1893 Michelson and Benoit working at the Bureau International des Podis et Mesures used an interferometer to measure the wavelength of the cadmium red line in terms of the meter. This progress allowed replacing the artifact meter at the request of the International Committee of Weights and Measures (CIPM). Because of having high coherence, this wavelength was chosen. However, the artifact standard was kept until 1960. At this year, the meter was redefined in terms of the wavelength of light, specifically the red-orange light emitted by excited krypton-86 gas.

Following the definition of the meter, for interferometric applications the newly invented helium-neon laser was beginning to be used. By the 1970's a number of wavelengths of stabilized lasers were considered much better sources of light than krypton red-orange. The candidates of CIPM decided not to use any particular wavelength, but to make a change in the measurement hierarchy. The solution was to define the speed of light in vacuum as exactly 299 792 458 m/s, and make length a

derived unit. The definition was chosen to be both intelligible enough to be understood by physics students and be precise enough to allow metrologists working at the measurement. Thus the definition was kept as simple as possible, with an additional recommendation of how to use it in practice.

" Le métre est la longeur du trajet parcouru dans le vide par la lumiére pendant une durée de 1/299 792 458 de seconde."

"la définition du métre en vigeur depuis 1960, fondée sur la transition entre les niveaux $2p_{10}$ et $5d_5$ de l'atome de krypton 86, soit abrogée."

"The meter is the length of the path traveled by light in vacuum during a time interval of 1/299 792 458 of a second"

"The definition of the meter in use since 1960, based on the transition between the two lines $2p_{10}$ and $5d_5$ of the krypton atom, is abrogated."

Given the defined speed of light, the wavelength of the light can be calculated and a meter can be generated by counting wavelengths of the light in interferometric measurements [2,4].

1.1.2 The Primary Length Standards and Their Traceability

As discussed before, the calibrations of the gauge blocks in interferometric methods are traceable to the definition of the meter through the use of stabilized laser wavelengths. Additionally, the frequencies of UME (National Metrology Institute in Turkey) He-Ne/I_2, Nd:YAG/I_2 and (External Cavity Diode Laser) ECDL/Rb wavelength standards are measured by Ti:Sa femtosecond Comb generator that is traceable to Cs atomic clocks. Additionally, the traceability of these lasers realized by international comparisons.

1.1.3 The Secondary Length Standards

The secondary length standards (line standards and end standards) are used in metrology because of everyday using of the primary length standards (stabilized lasers) is not appropriate.

The end standards are calibrated by interferometric or mechanic methods. Therefore, the length is transferred from the gauge blocks to customer blocks in industrial applications such as calibrating verniers, micrometers and verifying the performance of Co-ordinate Measuring Machines (CMMs). The gauge blocks, length bars, Hoke gauges and combination bars are the examples of the end standards [2]. The length bars have circular shape whereas the gauge blocks have rectangular shape. The dimensions of cross section are fixed, however the nominal lengths of them can be various. The dimensions of gauge blocks are 35 mm x 9 mm and the diameter of the length bar is 22 mm. The schematic diagrams can be seen in figure 1.2. We designed the interferometer to measure the gauge blocks that is rectangular shape.

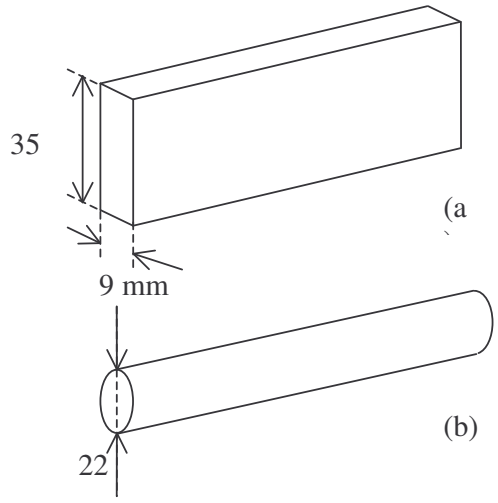

Figure 1.2 The schematic diagram of (a) gauge block and (b) length bar.

The gauge blocks are made of durable material such as steel, tungsten carbide, chrome carbide, and cervit. Despite the large thermal expansion coefficient, steel has always been the material of choice for gauge blocks. The reason for this is that most measuring and manufacturing machines are made of steel, and thermal effects tend to cancel. The gauge blocks have flat and parallel end faces. Moreover, the ends of the steel gauge blocks subjected to the hardening process during manufacturing. This hardening process is applied only the 30 to 60 mm of the block near the surfaces and affects the thermal expansion coefficient of the block [4].

The reference standard conditions for the length measurements of the gauge blocks are the temperature of 20 ^{0}C, the pressure of 101.325 Pa, the water vapour pressure of 1.333 Pa and CO_2 content of 0.03%.

In interferometric measurements a platen (parallel plate), which has reflecting surface, should be joined to the one end of the gauge block. This procedure is called 'wringing' and two faces are rotated slowly against each other. This removed the air film and allows adhesion to develop by intermolecular attraction [5].

The gauge blocks over 100 mm are called as long gauge blocks and supported horizontally at two points, 0.577L $\left(L/\sqrt{3}\right)$ apart. These points are termed the 'Airy points' of the block and their positions are engraved on the block's surface by the block's suppliers. Therefore, the sagging of the block is minimized and the ends of the block vertical and parallel with each other. The gauge blocks up to and including 100 mm are placed in the vertical position.

1.2 Definition of Metrology

Metrology is derived from the word 'meter' and means science of measurement. Metrology includes all both theoretical and practical with reference to measurements, whatever their level of accuracy, and in whatever field of science of technology they occur.

1.3 Contents of the Thesis

This thesis describes Köster interferometer instrument for long gauge block calibration and the measurement method. First in chapter 2, brief theory of interferometer systems is presented. The Michelson interferometer and Köster interferometer schematic diagrams for gauge blocks length measurements are given. Also the interferogram obtained from gauge block interferometer and its analyzing method is explained briefly.

In chapter 3, the design of the home made Köster interferometer is presented. Further the three frequency stabilized lasers used in interferometer and their stabilization systems are explained. Additionally, fibers, optical and opto-mechanical components and their installation places are presented.

The temperature stabilization and homogeneity are very important in length measurement interferometers. Chapter 4 explains the temperature controlling and temperature measurement system in detail. The construction of the interferometer to obtain accurate temperature stabilization is given in this chapter also. Additionally, the temperature measurements at different temperatures, the results of these measurements and statistical analyzing method are explained.

In chapter 5, two methods for finding refractive index of air inside the interferometer are determined. The first method that is using the Edlen formula with its modification version and the results of the refractive index calculations are discussed. The second method, the refractometer for direct refractive index measurement of air, and its construction are given in this chapter.

Chapter 6 examines the analysis of interferogram obtained in the Köster interferometer and multiple wavelength method used in gauge block length measurements. In interference analyzing, details of 5-position phase stepping

interferometry is presented firstly by using the theoretical interference fringes and then by original interference fringes. The phase unwrapping method is discussed that is necessary in the stage of producing the 3D profile of the gauge block and platen. The explanation of software for 3D profiles, flatness and variation in length of the gauge block is explained in this chapter also. Lastly, the multiple wavelength method to combine phase measurements at three wavelengths to allow accurate calculation of the length of the gauge blocks.

Chapter 7, the uncertainties in the measurement of gauge blocks by interferometry based on the ISO "Guide in the Expression of Uncertainty in Measurement" is evaluated. The influence parameters are determined and combined uncertainty calculations are realized. Thus, the uncertainty budget is formed and given in a table.

Finally, conclusion and discussion are presented in chapter 8.

CHAPTER 2

LENGTH MEASURING INTERFEROMETERS

Optical interference may be termed an interaction of two or more light waves yielding a resultant irradiance that deviates from the component irradiances [6]. In interferometers with white light, a few colored fringes can be seen. Because the coherent length of the white light is small, when the optical path difference between the interfering waves increases, the changes of color become less noticeable and finally disappear. By the invention of the laser, the limitations imposed by conventional techniques removed and many new interferometric techniques progressed [7].

Interferometric devices will be divided into two groups: wavefront splitting and amplitude splitting. The wavefront division uses apertures to isolate beams from separate portions of the primary wavefront. However, in amplitude division, two beams are derived from the same portion of the original wavefront. For such type interferometers, firstly the beam is divided into two arms, and then the two separate beams brought together again at a detector. The interference fringes are observed and examined according to the purpose of the experiment.

2.1. The Design of Michelson Interferometer

The Michelson interferometer is of amplitude division type and first introduced by Albert Michelson in 1881. The Michelson interferometer provides a substitute

standard for the meter in terms of wavelengths of light. The schematic diagram is shown in figure 2.1. The reflections at the beam splitter produces a virtual image M2' of the mirror M2. The interference pattern observed and its characteristics depend on the nature of the source and the separation of M1 and M2'. For example, with collimated light, *fringes of equal thickness* (fringes near the axis are equally spaced straight lines) are always observed. However, the separation of M1 and M2' is not important for collimated beam.

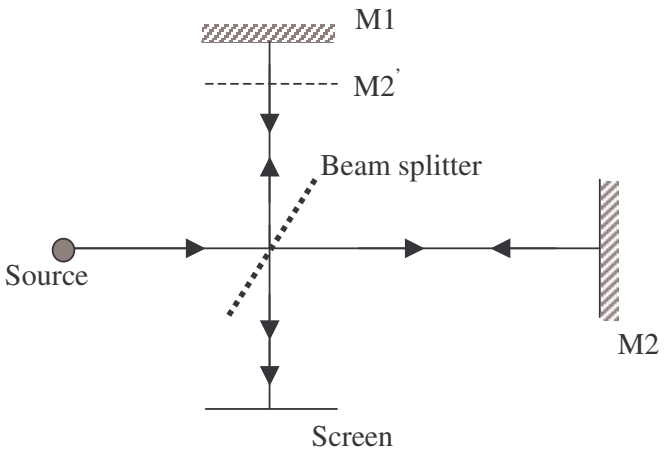

Figure 2.1 The Michelson interferometer in schematic diagram

The propagating electromagnetic waves can be represented as

$$\vec{E} = E_0 \, Cos\,(\vec{k}\,\vec{r} - \omega t + \phi_0) \tag{2.1}$$

where E is the electric field, E_0 is the electric field amplitude, $\vec{r}$ is the position vector, $\vec{k}$ is the propagating vector can be written as $k = 2\pi/\lambda$, ω is the angular frequency can be written as $\omega = 2\pi f$ and ϕ_0 is the original phase angle. Additionally,

λ is the wavelength of the light and f is its frequency [8].

In an interferometer as seen in figure 2.1, the light amplitude is divided in two parts. These two propagating electromagnetic waves can be expressed as,

$$\vec{E}_1 = E_{01}\, Cos\,(\vec{k}_1\, \vec{r}_1 - \omega t + \phi_{01}) \tag{2.2}$$

$$\vec{E}_2 = E_{02}\, Cos\,(\vec{k}_2\, \vec{r}_2 - \omega t + \phi_{02}) \tag{2.3}$$

In accordance with the principle of superposition, the electromagnetic fields are recombined in the beam splitter.

$$\vec{E} = \vec{E}_1 + \vec{E}_2 \tag{2.4}$$

Since we are interested in interference, our approach will be the irradiance.

$$I = \left\langle \vec{E} \right\rangle^2 \tag{2.5}$$

$$I = E_1^2 + E_2^2 + 2E_1E_2Cos\,(k(r_1 - r_2) - (\phi_1 - \phi_2)) \tag{2.6}$$

Total irradiance is presented as,

$$I = I_1 + I_2 + 2\sqrt{I_1 I_2}\cos\delta \tag{2.7}$$

where $\delta = k(r_1 - r_2) + (\phi_1 - \phi_2)$.

If the irradiance contributions from both arm are equal, $I_1=I_2=I_0$, the total irradiance can be presented as seen below,

$$I = 2I_0(1 + \cos\delta) = 4I_0\cos^2\frac{\delta}{2}. \tag{2.8}$$

The Michelson interferometer design with collimated beam is known as Twyman-Green interferometer as shown in figure 2.2. The gauge block whose length will be measured is attached to a platen. When the reference mirror is tilted with respect to the gauge and platen surfaces, tilt fringes (equal thickness fringes) are visible in the

image. Therefore, the beams reflected from the front-end surface of the gauge block and reference mirror realize the fringes at the middle part of the interferogram, where as the beams reflected from the platen and reference mirror produce the fringes at the both sides of the interferogram.

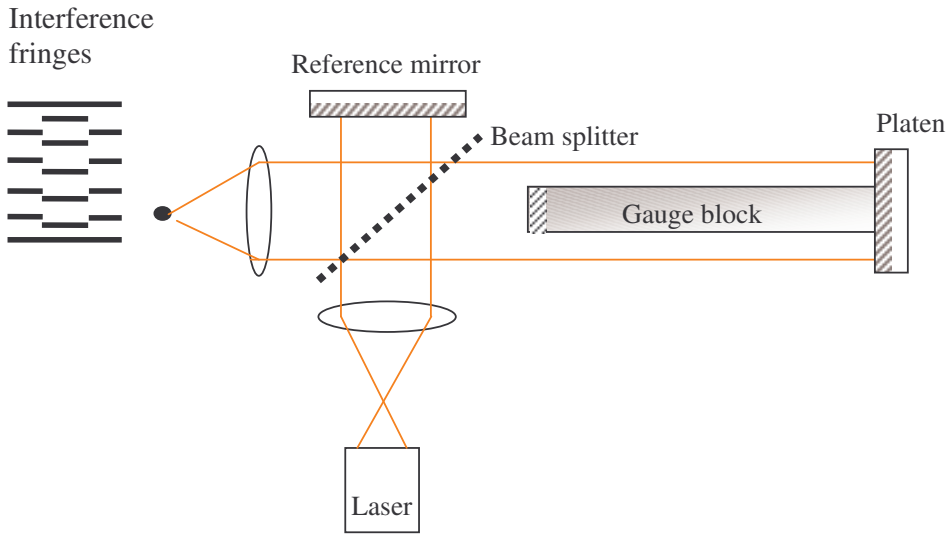

Figure 2.2 The schematic diagram of Twyman- Green interferometer for length measurement of gauge blocks

2.2 The Design of Köster Interferometer

In Köster's Interferometer as shown in figure 2.3, precision Köster's double prism is used as the beam splitter and combiner. Köster's interferometer has advantages than Michelson interferometer in being one dimension and a compensating plate is not necessary to get the same optical paths.

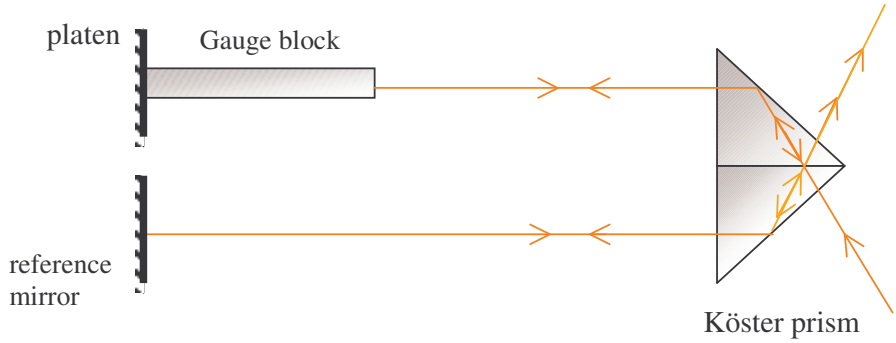

Figure 2.3 The schematic diagram of Köster's interferometer

2.3. Length Calculation of the Gauge Block

The exact definition of the length of a gauge block is "*the distance from the centre of the first face of the block to the plane of the reference flat to which the opposite face of the block is wrung*" [9]. The schematic diagram is shown in figure 2.4. The optical path difference between two beams is twice the length (L) of the block:

$$2L = N\lambda \tag{2.9}$$

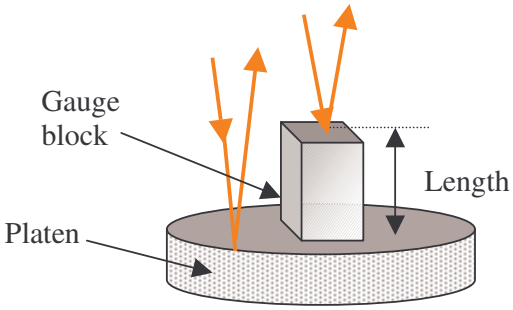

Figure 2.4 The schematic diagram of reflections from the surfaces of the platen and gauge block

Thus, light waves can be used to measure the length of a gauge block by counting how many waves N it takes to span the length of the gauge [10].

If L is an exact multiple of λ, then N is an integer. However, in general L also have the fractional part of the λ and can be expressed as shown below;

$$L = \frac{\lambda}{2} N + \Delta\ell \tag{2.10}$$

where $\Delta\ell$ corresponds to fractional part as shown in figure 2.5. L can also be written;

$$L = (N + f)\frac{\lambda}{2} \tag{2.11}$$

here f is called the *fringe fraction (0 < f <1)* and $\Delta\ell$ corresponds to ($f\frac{\lambda}{2}$).

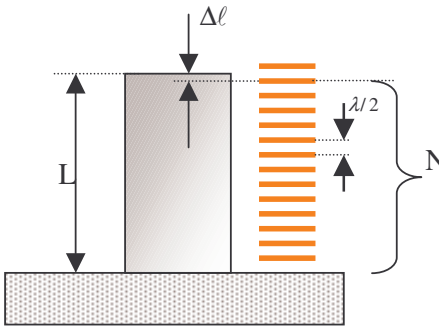

Figure 2.5 The schematic diagram of the exact and fractional multiples of *λ/2* through the length of the gauge block.

For obtaining fringe fraction, the interference fringes are examined. The fringe fraction is equal to *a/b,* where b corresponds to the distance between two consecutive

fringes whereas *a* corresponds to the distance of fractional part in the image of the interferogram as shown in figure 2.6. The fringe fractions measured at the centre of the gauge block surface for two and more wavelengths. The finding method of fringe fraction is explained in more detail in Chapter 6, Data Processing.

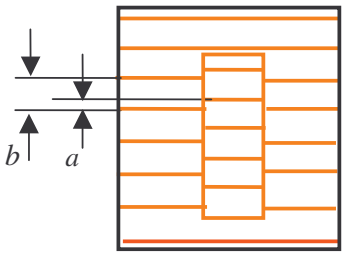

Figure 2.6 The schematic diagram of the interferogram with *a* and *b* values.

The interferogram, however, tells us noting about the exact multiple of the *λ/2* spanning *L,* gives information only the fractional part. For determining the exact multiple parts 'the *method of multiple wavelengths*' is used. The details of this method are given in Chapter 6, Data Processing.

CHAPTER 3

THE DESIGN OF THE INTERFEROMETER

The schematic diagram of the optical setup of interferometer is shown in figure 3.1.

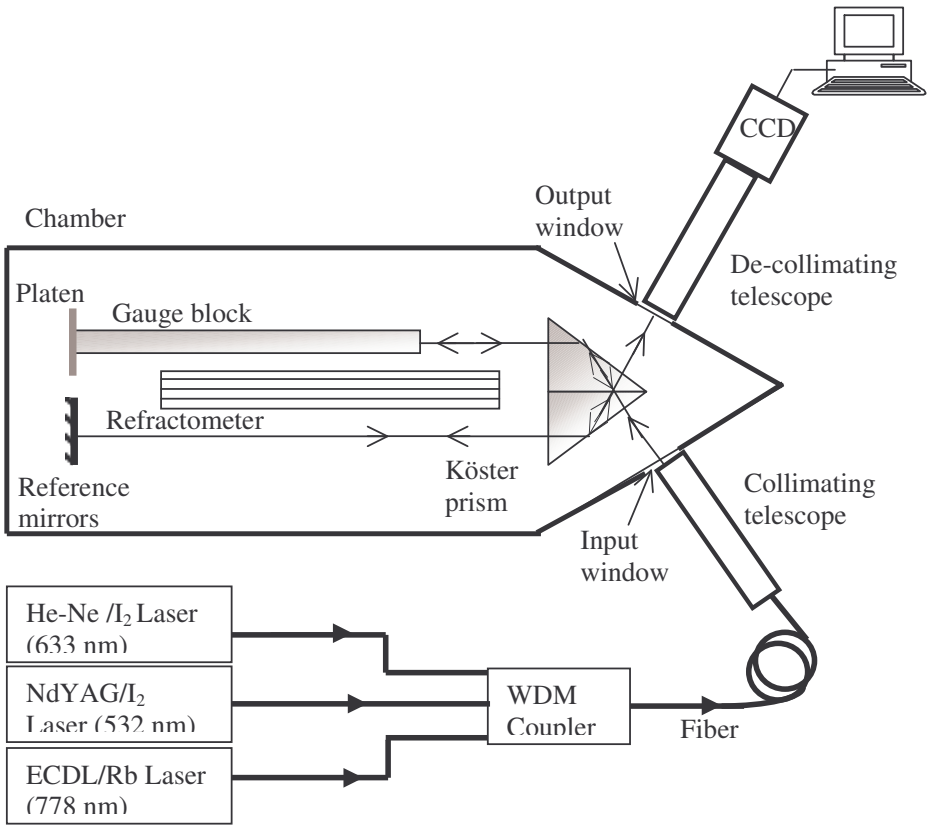

Figure 3.1 The schematic diagram of the interferometer with optical and opto-mechanical parts.

The laser beams from three different stable lasers (He-Ne/I_2 [11], Nd:YAG/ I_2 [12] and (ECDL) the external cavity diode laser stabilized on Rb atomic transition [13]) are launched to the different fiber cables, which are combined by the Wavelength Division Multiplexer (WDM) coupler. The fiber cable at the output of the WDM coupler is connected to the input of telescope. The laser beam is expanded up to 100 mm by using the collimating telescope and pointed at the inside of the chamber through the input quartz window ($\phi = 80$ mm). In the chamber, the laser beam is split into two as reference and measurement arms by using the Köster prism. The reference beam is reflected from the reference mirrors, whereas the measurement beam is reflected from the platen and the front surface of the gauge block. The reflected beams coming from the two arms are then combined by passing through the Köster prism. The fringes that form due to interference of the two laser beams are passed through the output window and then through the de-collimating telescope. Finally the interference fringes are detected using the PC-controlled charge coupled device (CCD) camera.

3.1. Lasers

In interferometer, three frequency-stabilized lasers are used. These are He-Ne/I_2, Nd:YAG/ I_2 and ECDL/Rb lasers. The description and their stabilization systems are discussed briefly below.

3.1.1 He-Ne/I_2 Laser

In the laboratory, three He-Ne/ I_2 laser setups have been built such that their frequencies are locked to the transition of I_2 molecules. The I_2 cells, which are placed in the He-Ne laser resonators, provide the interaction of He-Ne laser beam and I_2 molecules. By tuning laser frequency around energy transition of I_2 molecules absorption signals are detected. By using electronic servo system, this absorption signal of I_2 molecules are used for locking of laser frequency to the energy transition

of I_2 molecules with the stability of $1x10^{-13}$ in average time interval of 1000s.

In the laboratory three He-Ne/I_2 lasers are compared by optical-beat technique and by using this technique, the frequency stability of lasers is measured. Two different

lasers are brought on to the fast photodiode by beam-splitters and mirrors. Beat signal frequency at the output of the photodiode is equal to the difference of the two laser frequencies. The variation of the beat signal frequency with respect to the time gives us information about the stability of each of the two laser frequencies. The beat signal is observed and a computer controller counter measures the frequency of signal. The stability of beat signal and laser frequency is calculated by using Allan statistics.

The other He-Ne laser that has to be calibrated is compared with UME reference He-Ne/I_2 laser by using again the optical beat technique.

3.1.2 Nd:YAG/ I_2 Laser

3.1.2.1 Nd:YAG Laser Theory

Neodyium doped into YAG crystal (Yitrium Aluminium Garnet - $Y_3Al_5O_{12}$) is a four level system. Good quality crystals that have about 1 percent of sites occupied by Nd^{3+}. The energy level diagram for Nd^{3+} in YAG is illustrated in figure 3.2.

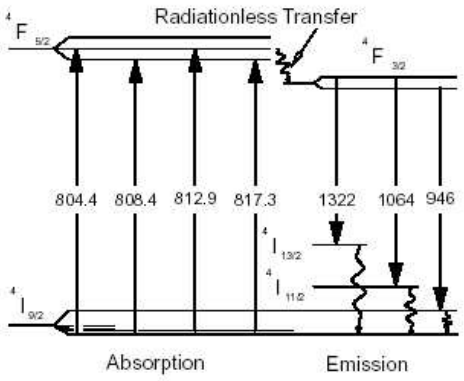

Figure 3.2. Energy levels in the Nd:YAG laser

The Nd: YAG laser is a four level laser system. The fine structure Stark splitting due to the electrostatic fields in the crystal is observed. The most intense transition between the bands $^4F_{3/2} \rightarrow {}^4I_{11/2}$ is in the wavelength region around 1.06 μm transition.

Optical pump sources for solid-state lasers include noble gas and metal vapour discharge lamps, filament lamps and lasers. At the beginning, the main pump sources have been noble gas flash lamps and filament lamps, the latter being used for CW operation only. After the developments in high-power semiconductor lasers are being used for pumping. The overall efficiency for flash lamp pumped lasers can be less than 1 percent. With diode laser pumping this efficiency can be increased to around 30 percent with the added of miniaturization and no water-cooling. Additionally extremely narrow bandwidths could be obtained. Nd:YAG laser are pumped with radiation about 809 nm from a GaAs/GaAlAs semiconductor laser.

3.1.2.2 Nd:YAG/I_2 Laser (532/ 1064 nm) Optical Frequency Standards

In our experiment [14], the Nd:YAG crystal is pumped by the diode laser beam having a wavelength of 810 nm. The Nd:YAG laser beam (1064 nm) as shown in the figure 3.3 passes through a non-linear crystal to produce frequency–doubled beam (532 nm). Therefore the input beam is in near infrared- invisible, where as the output beam from the nonlinear crystal is in visible region as green color. Both of the laser beams could be sent to the out through different apertures by using dichroic mirror.

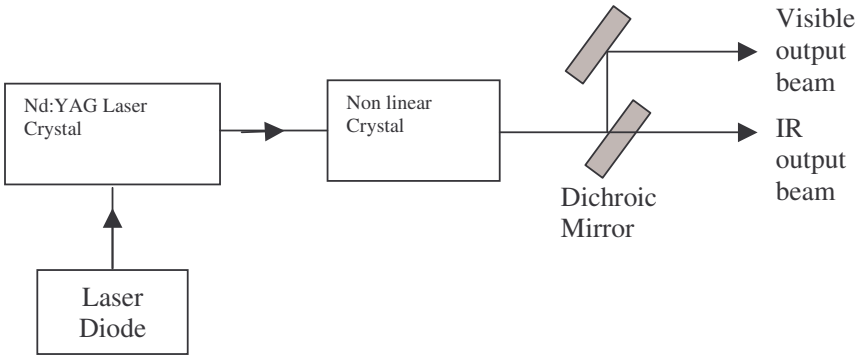

Figure 3.3 The schematic diagram of Nd:YAG laser in our experiment. The laser has two outputs as visible (532 nm) and IR (1064 nm).

The frequencies of two Nd:YAG lasers are compared by beat frequency technique (figure 3.4). In fact, the beat frequency technique is used since the photo detectors could not read the beat frequencies above 1 GHz. Therefore the frequency values of the lasers should be close to each other. Additionally the frequencies should be stable. For this reason, to stabilize the lasers, iodine cells are placed in the path of the laser beams. Thus, the absorption of the laser beam by iodine cells and fluorescence

radiation corresponds to this absorption is observed. For realizing fluorescence radiation, the temperature of the laser diode crystal and non linear crystal and also the temperature of Iodine cells should be arranged properly. At the end, the beat frequency is observed by the spectrum analyzer, which is connected to the photo detector.

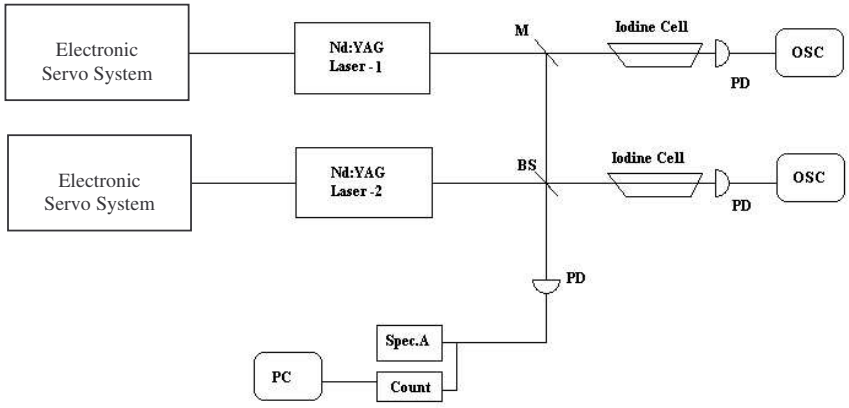

Figure 3.4 The schematic diagram of UME Nd:YAG Laser Optical Frequency Standard

3.1.3 ECDL/Rb Laser

The reason of realizing the external cavity diode laser is to be able to control of the laser diode's frequency. For such a configuration, the new cavity is placed at the path of the laser beam for optical feedback as a secondary mirror. The first mirror is the back surface of the laser diode.

Some optical components can be placed in the cavity. The important component is

the diffraction grating that is used for optical feed back. The laser beam can be tuned and the wideness of the laser bandwidth can be removed. To realize this process, the first order of the diffraction grating is sent to the diode laser as feedback. The wavelength of the back reflection depends on the angle between the coming beam and the surface of the grating, and also the constant of the diffraction grating.

$$\lambda = 2a\,Sin\theta \tag{2.1}$$

Therefore, very narrow frequency band can be feed backed to the laser diode and the modes that correspond to this frequency band are observed. Moreover, tuning of the laser wavelength is possible by using diffraction grating. The back reflected laser beams could be changeable by turning the diffraction grating.

The line width of the diode laser is reduced to a value of $(\ell / L)^2$ by using external cavity system. Here, ℓ corresponds to the length of the diode laser resonator and *L* corresponds to the length of the external resonator (the distance between the laser diode internal mirror and diffraction grating). For example, for ℓ=0.2 mm and L=200 mm, the line width is reduced to the value of 10^6. In general, the line width of the diode laser is in the range of 10-100 MHz.

The main problem in the external cavity designs is that the realizing of the mechanical and thermal stability. In UME wavelength standard laboratory [15], AlGaAs diode lasers are used having a wavelength of 852 nm. The schematic diagram of the system is shown in figure 3.5. The micro-objective is used to collimate the laser beam.

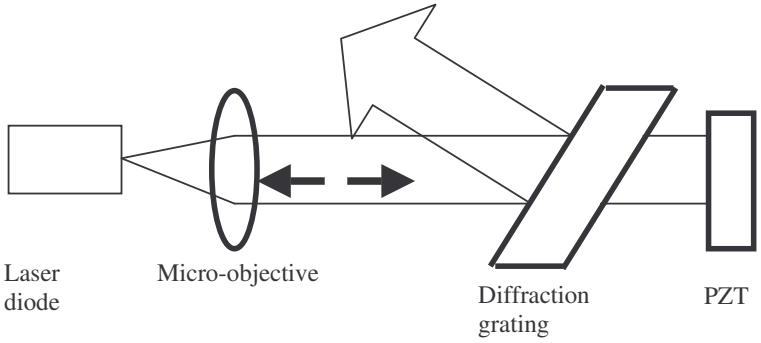

Figure 3.5 The schematic diagram of the External Cavity Diode Laser (ECDL)

The wavelength standards of 780 nm and 852 nm are realized by locking of external cavity diode lasers (ECDL) to the D_2 energy transitions of Rb atoms (780 nm) and Cs atoms (852 nm). The external cavity diode laser (ECDL) was used, which included the anti-reflection coated diode laser AC-SDL-5410 (spectra diode laser) as an active element with a nominal wavelength 850 nm. The external cavity was formed by the high reflection faces of the diode laser and diffraction grating (1200 lines/mm) mounted in the Littrow configuration on the piezo transducer PZT. The diffraction grating allowed detuning of the laser wavelength to the Cs D_2 line. By changing of diode laser's current with a rate of 1 GHz/mA, the temperature with a rate of 0.3 nm/C, the angle between diode laser and diffraction grating and also the length of external cavity (0-0.5 μm); the frequency of ECDL is adjusted to the energy transitions of Rb or Cs atoms. Fine-tuning was realized by the change of the length of the external cavity by using adjustable PZT voltage. Using of the selective external resonator helps the reduction of diode laser's spectral band (10-100 MHz) by an amount of $(\ell / L)^2$.

The ECDL laser beam passes through the glass cell in which there exists Rb or Cs gases, and then it is reflected back by using mirror and detected by photo-detector. Laser frequency is locked to the energy transition of atoms by using electronic servo system. The stability of laser frequency, when the frequency is not locked to the energy transition of atoms is changed in between $4x10^{-10}$ –$7x10^{-9}$ in the mean time interval 1-100 s.

After the locking process of the lasers to the energy transition of the atoms, it is measured that the frequency stability values are changed in the range $1x10^{-12}$-$5x10^{13}$. Additionally, laser frequency drifts during stabilization on atomic transition was measured less than ± 200 kHz.

Besides using of these lasers as length standards, they are used for realization of new Cs fountain frequency standards. In this process, the experiment that the trapping and cooling of Cs atoms by ECDL laser beam is done.

The wavelength standard of 778 nm is realized by using ECDL that is locked to S-D energy transition (778 nm) that corresponds to the two-photon resonance of Rb atoms [16]. Two photon absorption resonance used in frequency locking has much more advantage than the one photon resonance, because the bandwidth and Doppler expansion is much more less.

3.2. Fiber, Optical and Opto-Mechanical Components

3.2.1 Fiber Cables, Laser To Fiber Couplers And WDM Coupler

Because of the fact that the laser beams (532 nm, 633 nm and 778 nm) should be transmitted to the chamber of the interferometer, using of some fiber components is necessary for such systems. Details of the fiber components can be found in Appendix A.

First of all, in transmission process, three different laser beams are launched to the

three different fibers. The suitable laser to fiber couplers are placed for focusing the laser beams to the single mode fibers. Single mode fibers are used because in single mode fibers apart from the multimode fibers, large-scale speckle is not observed in the interference pattern since only one mode can propagate in the fibre [2].

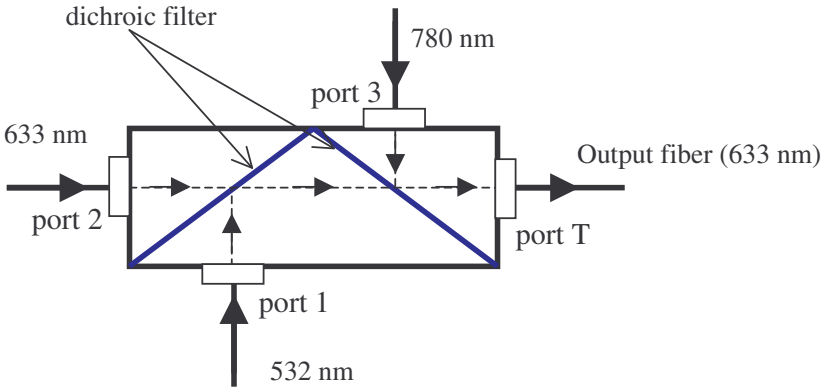

Figure 3.6 WDM coupler in schematic diagram.

Secondly, the wavelength divisions multiplexer (WDM) are used to combine light with different wavelengths into a single fiber (figure 3.6). The light from each fiber is first collimated. The collimated beams are combined using a dichroic filter, and the combined beams are focused into the output fiber. The dichroic filters are multi-layer thin film coatings that deposited on a glass substrate using thermal evaporation and high vacuum deposition technologies. Thus the filters transmit light in a certain spectral range and reflect light in another spectral range. The input and output fibers connections are chosen as pigtail style to obtain for optimum stability, minimum insertion losses and low back reflection.

Finally, an output fiber is used from the output of the WDM coupler to the input of the telescope. The end of the fiber is placed exactly at the focal point of the telescope. Therefore, the fine adjustment of the focal point of the telescope could be realized by using only one fiber end instead of the three fibers.

3.2.2 Attenuations in the Fiber Components

The large amount of powers of the laser beams would loss when the laser beam goes through the fiber components. The points where the laser powers calculated are shown in figure 3.7.

In figure 3.7 and table 3.1, the A-B path corresponds to the laser to fiber coupler, which is suitable for the laser wavelength and the beam diameter. The B-C paths correspond to the optical fibers having lengths of 25 meter. The operating wavelengths of the fibers are chosen taking care of the laser wavelengths. The D-E path corresponds to fiber cable in 25 meter length. However, the operating wavelength of this fiber is 633 nm. In fact in this fiber not only the 633 nm laser but also 532 nm and 778 nm lasers can propagate. Because of the fact that the 633 nm laser have the lowest power (100 μW) among the power of the other lasers (30 mW for 532 nm, 10 mW for 778 nm), the fiber having operating wavelength of 633 nm is used at the output of the WDM coupler. Therefore the attenuation in the fiber at the D-E path will be minimum for 633 nm laser beam.

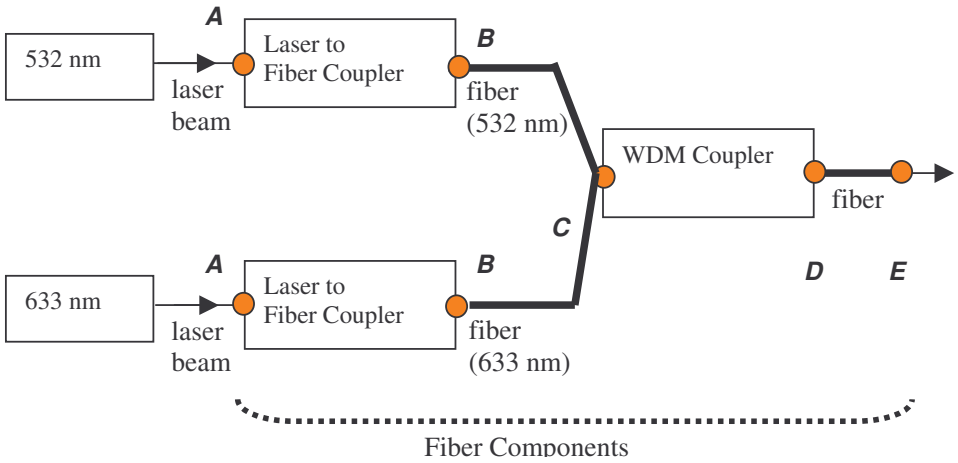

Figure 3.7 The schematic diagram of the laser beam's paths from lasers to the output of the WDM coupler's output fiber. A, B, C, D and E points corresponds to the points where the power of the laser beam calculated. (778 nm laser is not shown in the figure)

In figure 3.8 and table 3.1, the A-B path corresponds to the laser to fiber coupler, which is suitable for the laser wavelength and the beam diameter. The B-C paths correspond to the optical fibers having lengths of 25 meter. The operating wavelengths of the fibers are chosen taking care of the laser wavelengths. The D-E path corresponds to fiber cable in 25 meter length. However, the operating wavelength of this fiber is 633 nm. In fact in this fiber not only the 633 nm laser but also 532 nm and 778 nm lasers can propagate. Because of the fact that the 633 nm laser have the lowest power (100 μW) among the power of the other lasers (30 mW for 532 nm, 10 mW for 778 nm), the fiber having operating wavelength of 633 nm is used at the output of the WDM coupler. Therefore the attenuation in the fiber at the D-E path will be minimum for 633 nm laser beam.

Table 3.1(a) shows that the attenuation of the laser power suggested by the suppliers when the laser beam goes through the fiber components. The power of the lasers that are calculated theoretically at the specified points are seen in Table 3.1 (b). The power of 30 mW in the input of the fiber components is calculated 9.4 mW in the output of the fiber components. Similarly, the power of 100 μW in the input of the fiber components is calculated 39 μW in the output of the fiber components. Therefore the calculated efficiency is % 30 for 532 nm laser whereas % 40 for 633 nm laser. However, when the efficiencies are measured by a trap detector, it is observed that the measured efficiency is % 10 for 532 nm laser whereas % 30 for 633 nm laser (Table 3.1(c)). The reason of the inconsistency especially for 532 nm may be use of fiber operating in 633 nm at the output of the WDM coupler. This causes the attenuation to increase.

Table 3.1 (a) The given attenuation values, (b) theoretically calculated powers at specified points and (c) efficiencies of the fiber components.

	Suggested Attenuation			
	A-B (Coupler)	**B-C (Fiber)**	**C-D (WDM)**	**D-E (Fiber)**
532 nm	% 30	30 dB/km	2 dB	30 dB/km
633 nm	% 30	12 dB/km	2 dB	12 dB/km

(a)

	Calculated Power				
		B	**C**	**D**	**E**
532 nm	***30 mW***	21 mW	17.7 mW	11.2 mW	***9.4 mW***
633 nm	***100 μW***	70μW	66 μW	42 μW	***39 μW***

(b)

	Efficiency	
	Theoretical	**Experimental**
532 nm	% 30	% 10
633 nm	% 40	% 30

(c)

In spite of the high losses in the fiber components, the measured efficiencies are sufficient for the interferometer and imaging of the interference fringes by the CCD camera.

3.2.3 Collimating Telescope

The fiber cable at the end of the output of the WDM coupler is connected to the input of the telescope.

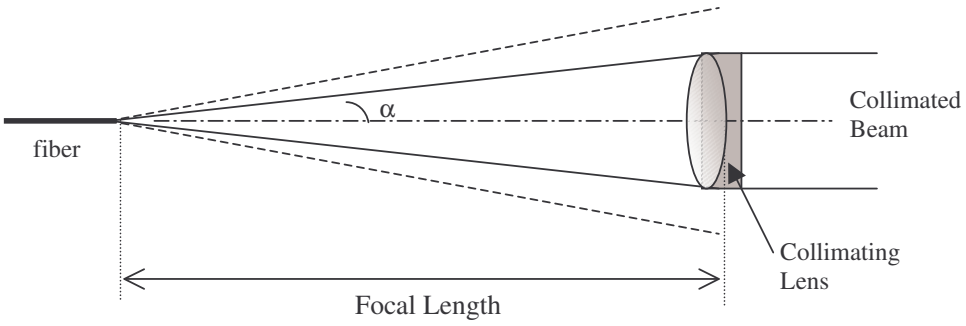

Figure 3.8 The schematic diagram of the collimating telescope

The light source is assumed as the core of the fiber, which has the diameter of 4 μm. The light beams from the fiber are spreading divergently. Therefore, the collimation system having one achromat doublet is used instead of two lenses. The end of the fiber is placed exactly at the focal point of the lens as shown in figure 3.8. Thus, the emerging beams from the collimating lens are collimated.

The numerical aperture (NA) value of the fiber is 0.11 and the emerging beam spreads with a divergence angle of α. The divergence angle (α) is found about 6.3 degree by using the below equation

$$NA = \sin \alpha \tag{3.1}$$

The diameter of the illumination at the place of the collimating lens would be bigger than the diameter of the lens. Thus the most uniform intensity as central Gaussian peak of the beam could be used by eliminating of the poor quality of the beam at the edges.

The achromatic doublet is used for the collimating lens to be able to prevent the chromatic and spherical aberration. The lens has a focal length of 1500 mm and a diameter of 100 mm. The telescope part, which is from the fiber end to the collimating lens (including lens), is covered by a cylindrical tube to prevent the air turbulence and to be able to obtain rigidity. The other technical properties could be found in Appendix A.

3.2.4 De-Collimating Telescope

The interference fringes are observed at the output of the Köster prism. The de-collimating telescope, which consists of de-collimating lens and imaging lens, are used to decrease the size of the interference fringes as parallel, and thus to be able to image at the CCD camera.

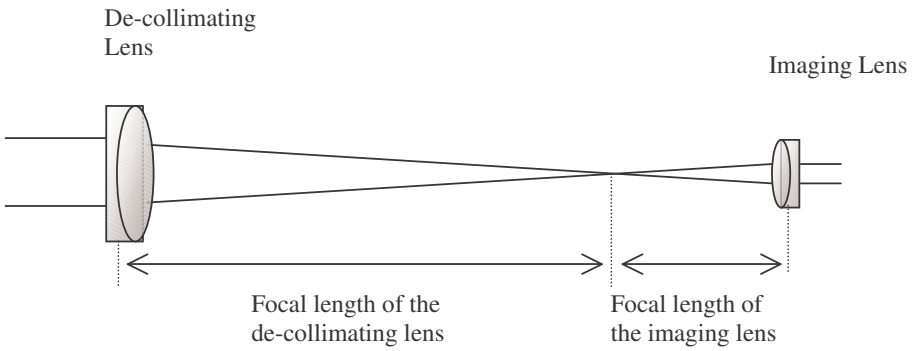

Figure 3.9 The schematic diagram of the de-collimating telescope

As seen from the figure 3.9, the image of the interference fringes coming to the de-collimating lens is focused at the focal point of the lens. Next, the image would be collimated again by using the imaging lens whose focal point is exactly placed at the focal point of the de-collimating lens. Thus the image of the interference fringes could be directed to the active area of the CCD camera. As a result, the diameter of the fringes having 50 mm in the input of the de-collimating telescope will be about 7 mm in the output of the de-collimating telescope. Because of the fact that the active area is in dimensions of 8.67 mm x 6.60 mm (2/3 inch format), CCD camera covers the image of the fringes.

The achromat doublets are used for the de-collimating lens and imaging lens. The focal length is 1000 mm for the de-collimating lens, whereas it is 140 mm for the imaging lens. The de-collimating telescope is covered by a cylindrical tube, which is including the de-collimating lens and imaging lens. The other technical properties could be found in Appendix A.

3.2.5 Köster's Interference Double Prism

The Köster's double prism consists of two identical prisms halves, which are cemented together as shown in figure 3.10. The angles of the prism halves are 30^0-60^0 – 90^0. It is used for splitting and then recombining of the laser beam.

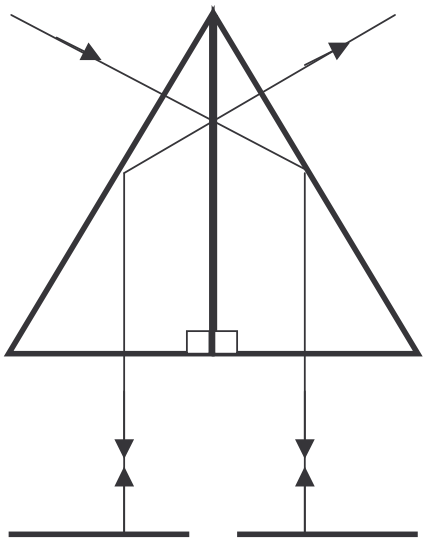

Figure 3.10 The Köster's double prism

There should be a small deviation (about 3 arc minutes) from a right angle between the output and the beam-splitting faces. This corresponds to a wedge angle for a beam-splitter plate and prevents superposition of unwanted reflections. Other technical properties can be found in Appendix A.

3.2.6 Reference Mirrors

The reference mirror is used to reflect the beams in the reference arm of the interferometer (figure 3.1). The reference mirror have capable of moving because of the application of the phase stepping method that will be discussed in the chapter of data processing. The digital piezo translator (DPT), which is mounted to the reference mirror, is used to move the mirror. However, such a horizontal movement of the mirror, which is placed vertically, could cause some tilting of the mirror in time. For preventing the tilting, the design of two mirrors is used as shown in figure 3.11 [2].

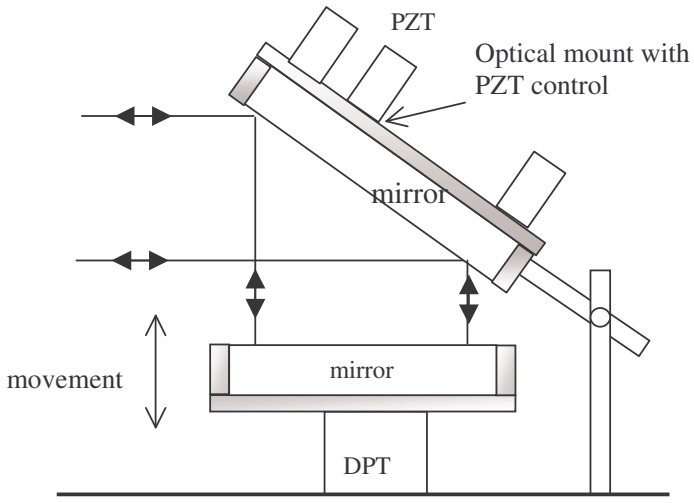

Figure 3.11 The placements of the reference mirrors at the reference arm of the interferometer

In this design, one of the mirrors is placed at 45^0 and it is hold fixed except of small alignments. The optical alignments of this mirror are realized by using the piezo electric transducer (PZT) that is mounted to the mirror. The other mirror is placed horizontally and DPT is mounted to this mirror. Thus, the necessary displacements because of the phase stepping are realized as vertically. The mirror will move totally as the half of the wavelength of the laser used for each 1-circle phase stepping application.

The mirrors are mounted to the base of the interferometer chamber by special apparatus that is manufactured by UME. The detailed technical properties can be found in Appendix A.

3.2.7 PZT and DPT Controlled Stages and Optical Mounts

Digital Piezo Translators (DPT's) are piezo electric translation devices with electronic and servo loop designs. These technologies provide positioning stages with sub-nanometer accuracy, precision and repeatability. Ordinary piezo-electric translators are non-linear and exhibit hysteresis and creep. To overcome these problems a position sensor is built in to each DPT. For moving a stage, a position command is sent to the controller by a computer. The motion is produced by a piezo actuator and monitored by this sensor. Using the feedback signal, the controller moves to the stage to minimize the difference between the sensed motion and the command [17,18]. To avoid the effects of thermal gradients, the material can be chosen with low thermal conductivity, such as Super Invar and Zerodur.

DPT is used to translate the horizontal mirror (figure 3.11) in z-direction when performing the phase stepping method. The mirror should move in steps ¼ fringe ($\lambda/8$) for five-step phase stepping method. $\lambda/8$ value corresponds to DPT step of sizes 66 nm, 79 nm and 97 nm for the 532 nm, 633 nm and 778 nm lasers, respectively.

The controller instrument of DPT is connected to PC by RS232. The DPT can be controlled by a PC after the installation of software. Therefore the actuator can be moved in definite intervals by writing the values of step sizes at the interface of the program.

The stages and holders with (piezo electric transducer) PZT control are used for the fine optical aligning and remote controlling when the cover of the interferometer chamber is closed. A motorized optical mount is placed at the reference arm for holding the 45^0 mirror as shown in figure 3.11. It has 3 motorized axes that with a resolution of 30 nm for each one. For attaching the mirror to the mounter an apparatus that is manufactured by UME is screwed to the mounter.

Two pieces of PZT controlled multi axes stages are used for holding the gauge block at airy points. Therefore, sensitive optical alignment of the gauge block can be realized with these stages.

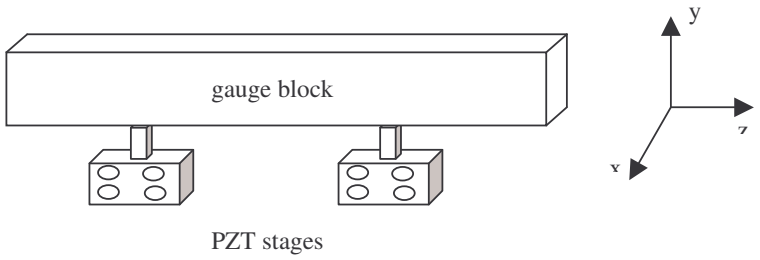

Figure 3.12 The placements of PZT stages.

The stages have four degrees of freedom such as x, y, θ_x and θ_y as shown in figure 3.12. The detailed technical properties can be found in Appendix A.

CHAPTER 4

TEMPERATURE MEASUREMENT SYSTEM OF INTERFEROMETER

4.1 The Importance of Temperature Measurement in Interferometer

In interferometric applications, especially in length measurements for metrological purpose, temperature measurement and temperature stabilization in the interferometric chamber are highly important.

The uncertainties of the temperature measurement in a length interferometer chamber depend on two main factors. The first factor is the temperature fluctuation inside the interferometer chamber, which is depend on the design of the instrument and the second factor is the uncertainty of the sensors used and their measurement methods.

The largest contributing factor to the total uncertainty of length measurements in interferometers is due to the thermal expansion of individual gauge blocks [19]. The thermal expansion uncertainty arises from two uncertainties: the uncertainty in the expansion coefficient (multiplied by the temperature deviation from the reference temperature) and the uncertainty in the temperature measurement (multiplied by the expansion coefficient). When the uncertainty of the gauge block temperature measurement is within 1 mK, then a length uncertainty of 12 nm is observed [20]. Additionally, the temperature measurement of the air contributes to the refractive index uncertainty. The laser wavelength is directly dependent on the refractive index Inside the chamber. Since this refractive index is obtained by using of the

temperature, pressure and humidity measurements of the air inside the chamber, these values should be measured very accurately. Besides, effective thermal and pressure isolation of the chamber gives rise to effective refractive index stabilization.

4.2 The Surface Temperature Measurements

The accurate surface temperature measurement of the gauge blocks is very important for two reasons: The first is the necessity of doing accurate temperature controlling in different points along the gauge block. The second is the sensitive temperature measurement of the block in different temperature points when calculating the thermal expansion coefficient.

4.2.1 The Factors Effecting Surface Temperature Measurements

Surface temperature has to be measured in an accurate manner, since the surface temperature sensor is not immersed in a solid or fluid. The external conditions affect the interaction between the sensor and surface of the material. Additionally, there may be very vital errors in the measurement results depending on the sensors used in the measurement and in the measurement techniques.

The important reason of these errors is having a high contact thermal resistance between the surface and the sensor. The contact resistance value will be decremented due to the increment in contact zone between surface and sensor and due to the increment in gas and contact pressure. Besides, if the surface is made up with rough and tough conduction materials, the contact will not be obtained perfectly and hence the contact resistance will increase. Additionally, the inner structure of the probe will affect the contact resistance directly.

Therefore, the following precautions can be taken, to decrease the errors in the surface temperature measurements; 1) The contact pressure between the surface and

sensors can be increased. 2) The area of contact surface can be increased. 3) Thermal grease can be applied between the surfaces. 4) In order to increase the contact surface, the sensors can be calibrated in the liquid [20,21].

Another important issue affecting the surface measurement results is the possibility to measure the temperature of the environment -in that the sensor is placed- together with the temperature of the surface. This possibility can be decreased by placing insulation material over the sensor [22].

4.2.2 The Main Types of the Surface Thermometers

After mentioning the errors, which is arisen from the environmental conditions faced during the measurements of the surface sensors, it is the right time to investigate three main types of surface thermometer constructions.

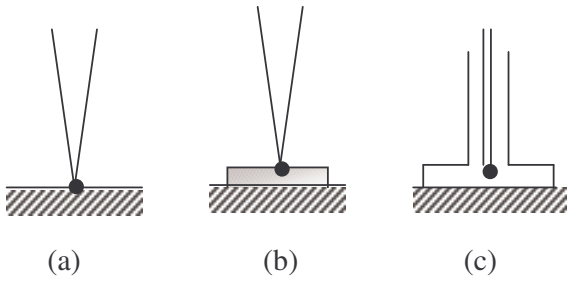

Figure 4.1 The schematic diagrams of the main types of the surface thermometers.

The thermometer in Figure 4.1(a) is a standard thermometer. Since the contact between the thermometer and the surface is minimum, the thermal contact resistance value and hence the error obtained from the measurement shall be high. The

thermometer in Figure 4.1(b) is a stamp type thermometer. The sensing element is placed inside a mid-surface. So the contact area is increased and hence contact resistance value is decreased. For the thermometer in Figure 4.1(c), the systematic error is minimized. The large contact surface reduces thermal contact resistance. Furthermore the insulation material, which is placed in the interface of contact surface with the air, prevents to measure of the environment temperature as discussed in Section 4.2.1.

4.2.3 The Surface Thermometers in Gauge Block Temperature Measurements

The surface temperature measurements could be realized by using platinum resistance thermometers (PRTs) or thermistors (thermal resistors).

The various metrology institutes are being used *platinum resistance thermometer* especially Pt100 thermometers for gauge block surface measurements. A Pt100 thermometer having a self-heating with 0.3 ^{0}C and 3 mK caused by a measuring current between 1 mA and 0.1 mA in sequence [20]. In order to prevent this, it means to reduce the self-heating, it is necessary to decrease the thermal contact resistance, as discussed before in section 4.2.1. Thus the self-heating could be minimized to few mK value and could be neglected.

After the discussion about Pt100s, we will now start to discuss about *thermistors*, which is used in this study. Thermistors are semiconducting ceramic resistors made from various metal oxides. They have one outstanding advantage over all other resistance thermometers, namely very high sensitivity. It means that thermistors exhibit large changes in resistance with a change in its body temperature. The reason of that is the exponential relation between the resistance and the temperature of the thermistors. When comparing of its sensitivity according to Pt100, sensitivity of a thermistor is about 4%K^{-1}, whereas for the Pt100 this is approximately 0.4%K^{-1} [20]. In this situation, because of the enough sensitivity, sophisticated measuring equipment is not needed for thermistors.

Besides, thermistors could be produced in small dimensions. This property enables usefulness in various temperature measurement applications for them. In addition to that its smallness give rise to the fast response time [23].

Since the thermistors have high resistive value, it could work in small currents and hence self-heating could be emitted easily. For example, self-heating of a 20 kΩ thermistors to be about 2 mK when using 10 μA measuring current [20].

Another advantage of thermistor is that it is much cheaper than Pt100.

4.3 Temperature Measurement System in UME-Köster Interferometer

4.3.1 The Construction of the Thermistors

In our experimental setup, we preferred to use the thermistor because of the mentioned advantages in Section 4.2.3. In the system, 10 pieces of thermistors are used as 4 of them as disc-type and 6 of them as bead-type. Disc thermistors are designed to measure surface temperatures whereas bead thermistors are designed for air temperature in the interferometer. The construction of them is shown in Figure 4.2.

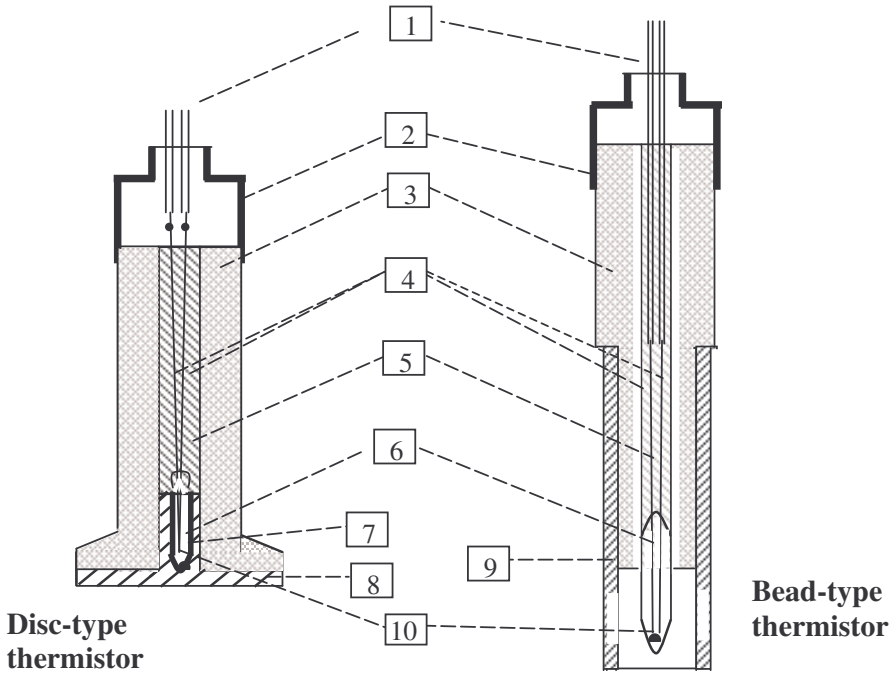

Figure 4.2. The schematic figures of air and surface thermistors. 1) 4 pieces of copper wires, 2) Al cap, 3) polyamide, 4) 2 Nickel wires with diameter of 0,2 mm, 5) epoxy glue, 6) glass sheath, 7) the layer of thermo conductive paste, 8) copper plate covered by silver, 9) stainless steel sheath, 10) thermistor sensitive element. (The diagram is not in scale)

4.3.2 The Places of the Thermistors in the Interferometer

In our system, four thermistors are used for surface temperature measurement of the gauge block and the other six are used for the air temperature measurement inside the chamber.

The gauge block is placed horizontally inside the chamber and its length is measured in that position. The block is supported at two points named the airy points as shown in figure 4.3. In the measurement of its surface temperature, the platen is not wrung to the block, so the block is supported exactly at the airy points. Support at these points minimizes sagging of the block. The distance between the airy points is calculated by dividing the length (L) of the block by $\sqrt{3}$ and it is engraved on the gauge block's surface by the block's suppliers [2]. For the temperature measurement of the gauge block, two surface thermistors are installed separately inside the two block supporters, which are placed at the airy points. One of the other two surface thermistors is placed 10 cm to the left of the first airy point and the other one is placed 10 cm to the right of the second airy point for 1 m gauge block.

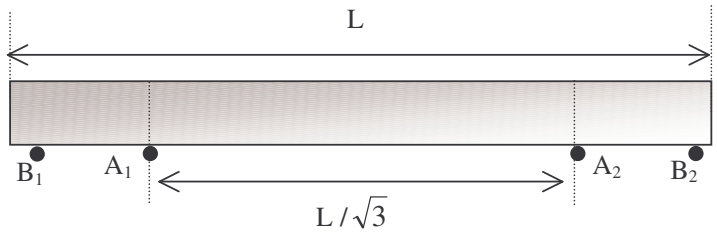

Figure 4.3 The placements of the airy points and surface temperatures of the 1-meter gauge block. L; length of the gauge block. A_1 and A_2; airy points. The two surface thermistors placed at the airy points. B_1 and B_2; placements of the other two surface thermistors at points 10 cm away from the airy points

All of the surface thermistors are attached to the gauge block at the bottom side of the block. Since the surface roughness of the thermistors reduced at the production stage and additionally thermal contact is assumed to be good enough to sense and care must be given to not damage the surface of the block, it is preferred that thermal

grease not be used between the contact surfaces during temperature measurement in this work. Additionally, the back (non-contact) sides of the surface thermistors are covered with insulation in the production stage to reduce the effects of the environment. Furthermore, a spring mechanism is placed in the thermistor holders to increase the contact pressure [20-22]. The air thermistors are placed at different points inside the chamber along the gauge block.

4.3.3. The Measurement Principle and Calibration Techniques of Thermistors

The temperature measurement system is intended for precise temperature measurements in the range of 15 ^{o}C to 25 ^{o}C with an accuracy of 0.002 ^{o}C. Nominal resistance of the thermistors at 20 ^{o}C is 12 ± 1 kΩ. The resistances of the thermistors are measured with a Wheatstone bridge. The sensitivity at 20 ^{0}C is 0.475 ± 0.025 kΩ / ^{o}C. This corresponds to a sensitivity value of 3.9 ± 0.2 %K^{-1}.

Using the measurement results of thermistor resistances, the temperature t is calculated by with formula [24]:

$$t = \frac{1}{A + B\ln R + C(\ln R)^3} - 273.15 \qquad (4.1)$$

where t is temperature in ^{o}C, R is thermistor resistance in ohms, and A, B and C are individual calibration coefficients for each thermistor.

The thermistors are calibrated by using three different fixed points as GaIn eutectic alloy at 15.646 ^{o}C, GaSn eutectic alloy at 20.482 ^{o}C and Ga at 29.765 ^{o}C. The calibration coefficients of A, B and C in equation 4.1 are calculated with these fixed points for the indicated thermistor. The most reproducible constant temperature of the eutectic alloy cells is their melting temperature and the cells enable us to have phase transitions not less than 3 hours.

The fixed points used in this work are calibrated in Temperature Laboratory of UME by Standard Platinum Resistance Thermometer (SPRT), which is traceable to ITS90 scale. Each thermistor is calibrated by using these fixed points (GaIn, GaSn and Ga). The expanded (k=2) uncertainty of each thermistor, which includes the uncertainties of fixed points, is 2 mK.

The resistance of each thermistor is measured through a PC controlled system. The measurement results are calculated by a special computer program that includes the individual calibration coefficients of thermistors. Additionally, the time dependency of the temperature for each thermistor is obtained automatically in graphical and data formats.

4.3.4 Thermostat of the Köster Interferometer

A schematic diagram of the cross-section of the UME Köster interferometric chamber (thermostat) is shown in figure 4.4 in which, the cross-sectional internal size dimensions of the chamber are 250 x 300 mm and the internal length of the chamber is 1750 mm. The similar interferometers are developed in different metrology laboratories. During the design and development of UME interferometer, it is based on the design of long gauge block interferometers of NPL [2,25] and PTB [26]. Especially, water-circulating system is based on interferometer of NPL, whereas the shape of the chamber is based on interferometer of PTB.

Our interferometric thermostat is constructed as a coaxial box which has an outer thickness of 4 mm and an inner thickness of 16 mm. Different isolation materials, roof mate and glass wool, having different thicknesses are used between the two boxes, which are separated by 70 mm. The box is made of Aluminum (AZ 7075).

Temperature stabilization is obtained by circulating the water through copper pipes that are placed side by side, over the surface of the inner box including the cover

part. One of these copper pipes brings the chilled water to the chamber whereas the other one carries the circulated water away from the chamber. For continuous water flow, a refrigerated circulator with a resolution of $0.1^{o}C$ is used. Finally, to prevent air leakage when the cover is closed, a flange channel is formed between the touching parts of the cover and the main body, and a suitable o-ring is placed in the flange channel. Additionally, the cover part can be sealed fully to the main body by its nine different points along the chamber.

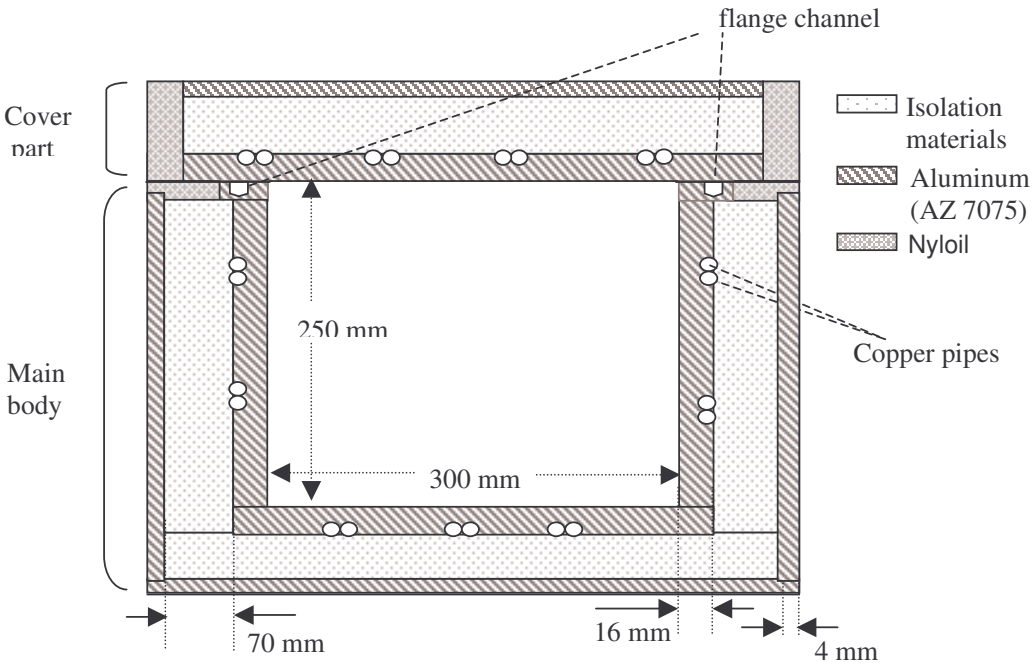

Figure 4.4. The cross section of the main body and cover part including Aluminum boxes, isolation materials, Nyloil and copper pipes (the diagram is not to scale).

Moreover, some tiny holes are drilled through one wall of the chamber to open channels for the cables and pipes. The proper flanges and o-rings are used in these

apertures to obtain temperature and pressure isolation. Each flange is utilized for the following measurements and controls; temperature, pressure, humidity, changing of internal gas, obtaining vacuum in the refractometer, control of the digital piezo translator (DPT) installed on the reference mirror, control of the piezo electric transducer (PZT) installed on the second reference mirror and control of the PZT installed on the gauge block holders. PZT and DPT are used for translating the mirrors accurately and remotely when the cover is closed.

For improving temperature control and stabilization, the lasers and the CCD camera, which can be sources of unwanted heat, are placed outside the chamber. Meanwhile the other necessary optical and opto-mechanical parts, i.e. the mirrors on the reference arm, the Köster prism, the PZT controlled mirror and gauge block holders, are placed inside the chamber.

4.4 The Results of Temperature Measurements

The results of a typical temperature measurement is shown in figure 4.5(a). During this measurement, the temperature inside the laboratory was 21.0 ± 0.5 ^{o}C. The temperature of the circulator is set to 20 ^{o}C so that the water circulates at 20 ^{o}C ± 0.1 ^{o}C along the copper pipes. The temperature measurement is realized for about 20 hours. The system reached the temperature of about 20 ^{o}C at the end of the first 4 hours and achieved stability after the first 14 hours. The first four thermistors are surface thermistors whereas the other six ones are air thermistors. As shown in figure

4.5(a), the time dependent change of the temperature value for air thermistors is faster than the value for surface thermistors. This is due to the fact that air thermistors measure the air temperature inside the interferometric chamber, whereas the surface thermistors measure the temperature of the gauge block, which is mounted on the two airy points in the interferometric chamber. This result shows that temperature of the gauge block reaches the set temperature later than the air

temperature inside the chamber due to its mass and its lower efficiency of thermal contact with the chamber wall.

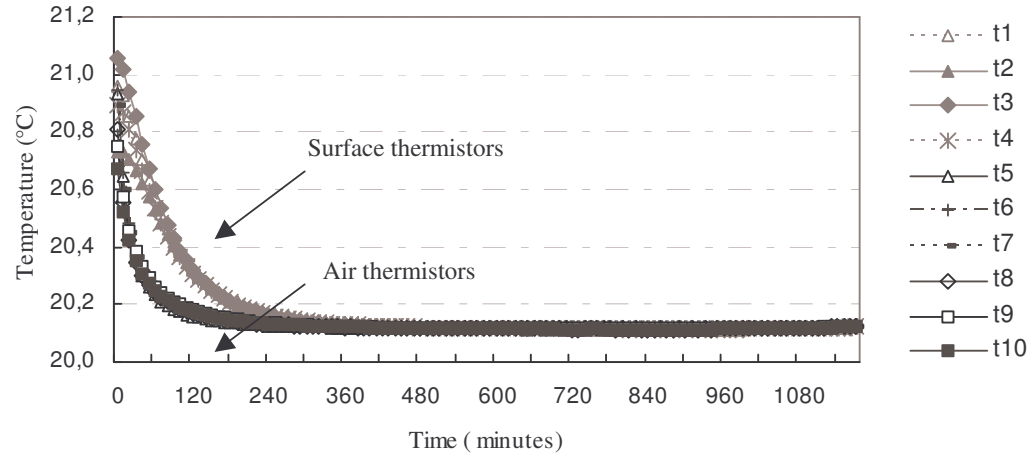

(a)

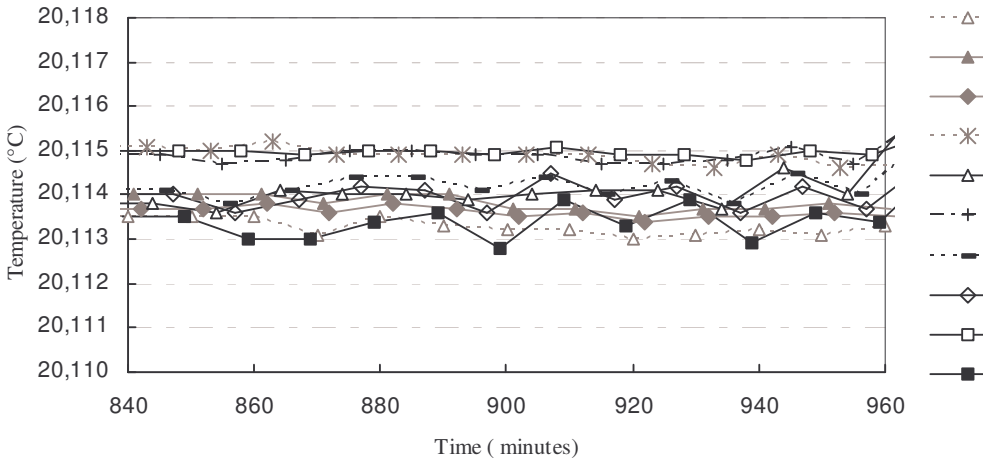

(b)

Figure 4.5. The temperature readings from all thermistors (the first four ones are surface thermistors whereas the other six ones are air thermistors) at about 20 ^{0}C for (a) about 20 hours, (b) about 2 hours. The temperature fluctuations of all thermistors remains in the range of 2 mK.

As shown in figures 4.5(a) and (b), after temperature stabilization of the chamber and gauge block (about 840 minutes), the temperature variation of all thermistors remains in the range of 2 mK for about 2 hours. In figure 4.5, the t1, t2, t3 and t4 curves correspond to the measurement results of surface temperature, whereas t5-t10 curves correspond to the measurement results of the air temperature. As it is seen in figure 4.5(b), the temperature variations of each thermistor separately are smaller than 1 mK for the same time interval.

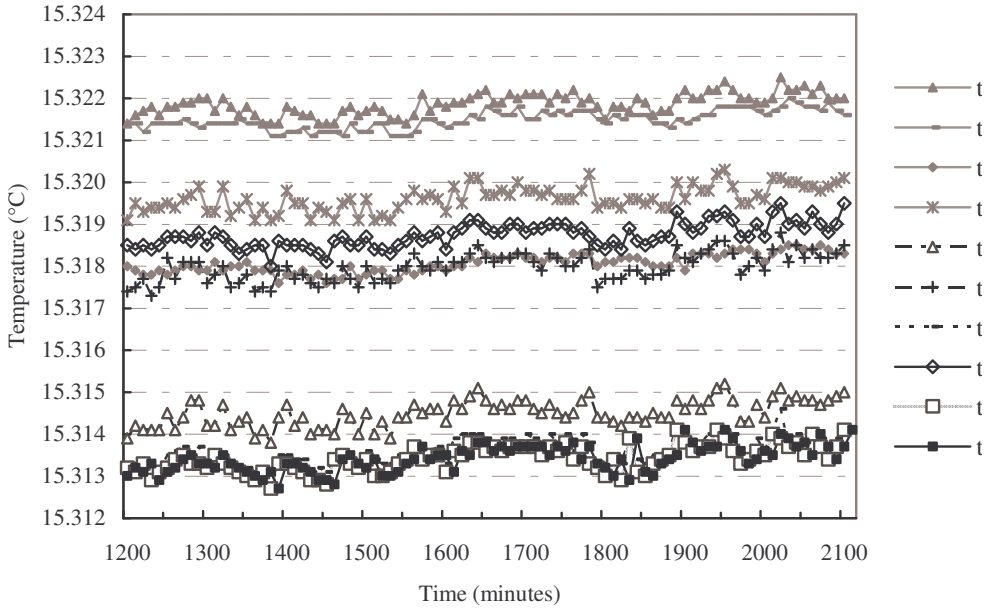

Figure 4.6. The temperature readings from all thermistors (the first four ones are surface thermistors whereas the other six ones are air thermistors) at about 15 ^{0}C for about 15 hours. The temperature fluctuations of all thermistors remains in the range of 9 mK.

A similar measurement is realized by setting the circulator's temperature to 15 ^{o}C. If we were to calculate the thermal expansion coefficient of the gauge block [2,19,25,27,28], the temperature of the chamber would be stepped along a range of 15 ^{o}C to 25 ^{o}C in definite increments. However in this study, the measurement is realized only at 15 ^{o}C, in order to test the system at a different temperature than 20 ^{o}C. The temperature measurement results at 15 ^{o}C are presented in figure 4.6. After temperature stabilization, the temperature variation of all thermistors remains within the range of 9 mK. It is observed that the temperature variation is about 4 mK for surface thermistors, whereas it is about 6 mK for air thermistors. In comparing the results in figures 4.5 and 4.6, away from the room temperature, the temperature

variation in the chamber becomes inhomogeneous due to influence of the temperature gradient of the communication cables and connectors (flange) on the chamber wall. As deducted from the graphic in figure 4.6, a small drift about 1 mK is observed within 15 hours.

For examining the temperature difference of the upper and lower parts of the gauge block, additional experiments are realized. The measurements are done at 20 ^{o}C and the results of the measurement are shown in figure 4.7. In this measurement, two surface thermistors are located under the block at the airy points whereas the other two ones are located on the top of the block at places corresponding to airy points (figure 4.7(a)). After temperature stabilization of chamber, the result of temperature measurement for two hours is shown in figure 4.7(b). The temperature values of two sensors (t1 and t3) are as close as a value of smaller than 0.5 mK. Similar result is seen for two other sensors (t2 and t4). It is deducted from the results that the gauge block is reached to the stable temperature with surrounding air of the block inside the chamber. After the system is stabilized, the temperature of the upper part of the block is quite as close as lower part of the block. Meanwhile, the temperature difference of two airy points is about 2 mK.

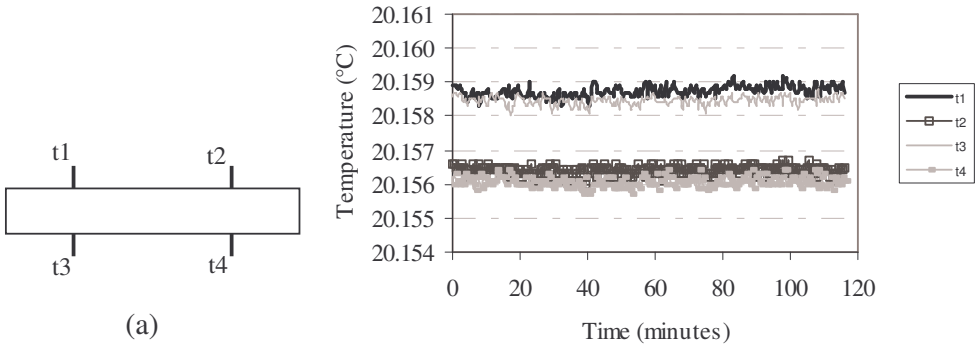

Figure 4.7 (a) The placements of the surface thermistors for examining the temperature difference of upper and lower parts of the gauge block, (b) the results of the temperature measurements. The temperature difference, which corresponds to the temperature gradient of upper and lower parts of the block, between the sensors (t1and t3, t2 and t4) is smaller than 0.5 mK.

For the influence of the platen to the temperature gradient of the gauge block, similar experiments are realized when platen is wrung to gauge block. The dimensions of the platen, which is used in this experiment, are 40 mm x 30 mm x 10mm. The measurements are done at 20 ^{o}C and 15 ^{o}C. The sensors are mounted at opposite sides at the airy points of gauge block (figure 4.8(a)). After temperature stabilization of chamber, the results of temperature measurement for two hours are shown in figure 4.8(b) and 4.8(c) for temperatures of 20 ^{o}C and 15 ^{o}C, respectively.

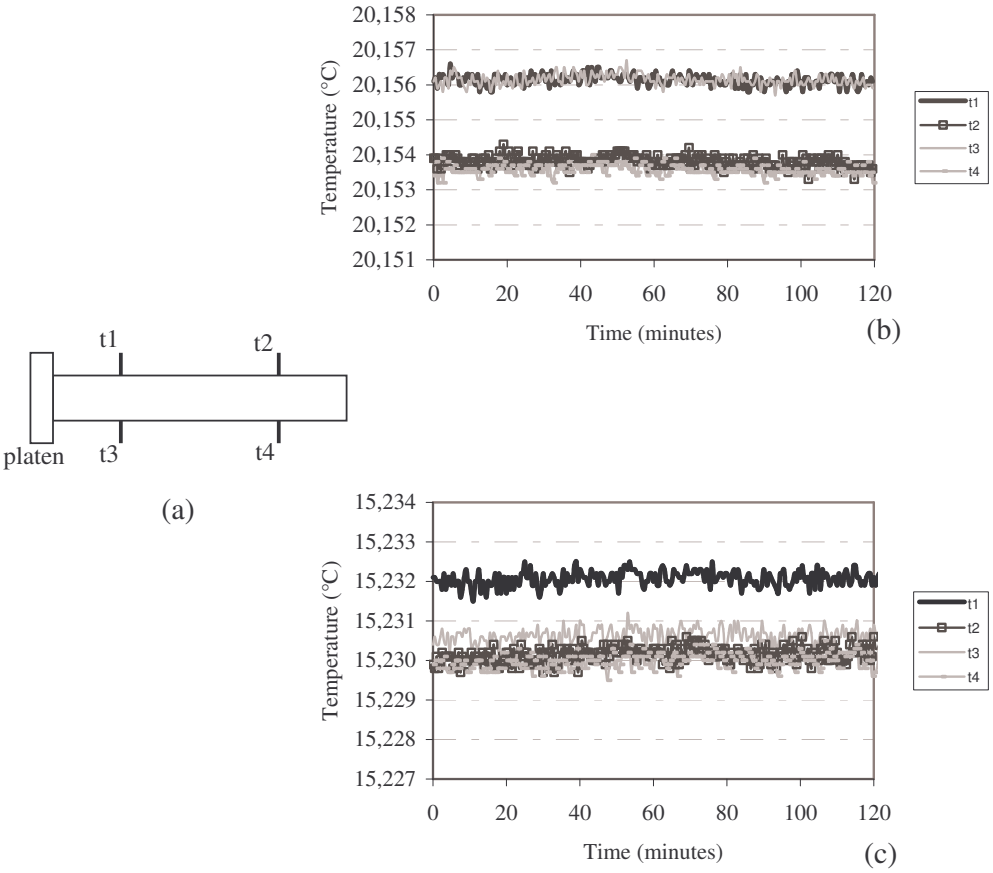

Figure 4.8. (a) The placements of the surface thermistors over the gauge block with the platen for influence of the platen to the temperature gradient of the block, (b) the temperature measurement results at 20 ^{0}C and (c) at 15 ^{0}C. The difference of the measured temperature values at airy points in the experiments at 20 ^{o}C or 15 ^{o}C with or without platen is about 2 mK.

As seen from the figure 4.8(b), the temperature difference of opposite sensors (t1-t3 or t2-t4) is about 0.5 mK whereas the temperature difference between the airy points is about 2 mK. With the experiment realized at 15 ^{o}C (figure 4.8(c)), the temperature difference of opposite sensors and the airy points is observed about 2 mK. We would

like to note that when comparing the measurement results with or without platen, an extra temperature gradient is not observed between the airy points. When the uncertainties of the sensors are taken into account, the difference of the measured temperature values at airy points in the experiments at 20 ^{o}C or 15 ^{o}C with or without platen is about 2 mK.

In this experiment, the temperature measurement for each thermistor is realized during an average time interval of one minute and thus, a single measurement data for each thermistor is taken every 10 minutes because there are 10 pieces of thermistors. In order to investigate the temperature stability in more detail, an additional measurement is realized using an air thermistor located at the center of the chamber. Within a span of 7 hours, we measure the temperature of the chamber using the thermistor in 1-second average time intervals. The graph of temperature versus time is shown in figure 4.9(a). The histogram of this measurement is shown in figure 4.9(b). This experimental result shows a symmetrical distribution of temperature fluctuation around the mean value of 20.1562 ^{o}C with a peak-to-peak temperature fluctuation of less than 30 mK and a standard deviation value of 0.4 mK.

The stability of temperature measurement results as shown in figure 4.9(c) is evaluated using Allan variance statistics [29]. Figure 4.9(c) shows the stability and the root Allan variance value as a function of the average time. When the temperature of the chamber is stabilized, the measured Allan variance of the temperature fluctuation shows a temperature stability of about 10^{-5} for average times noise from 1 second to 1000 seconds. As shown in figure 4.9(a), the white and flicker is dominated and drift is comparably small. So non-decreasing variance as a function of averaging time in figure 4.9(c) will be explained as long-term stability that is limited and determined by flicker noise and no long-term drift.

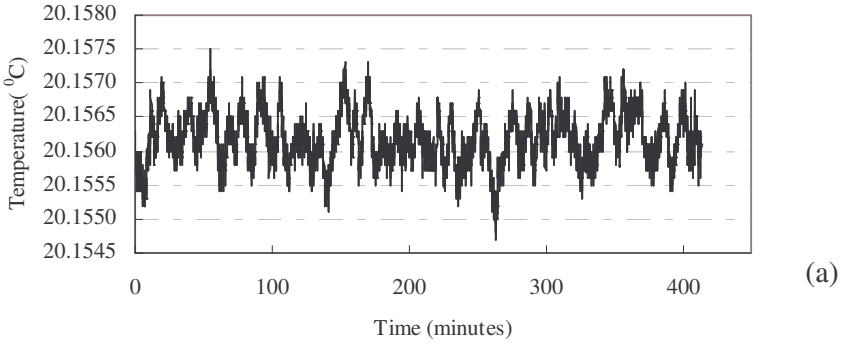

(a)

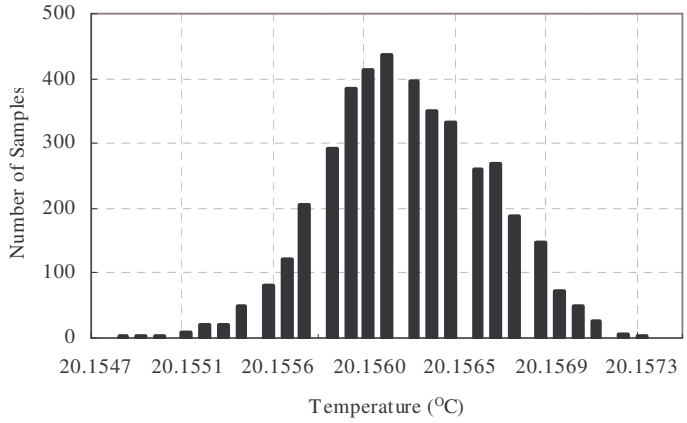

(b)

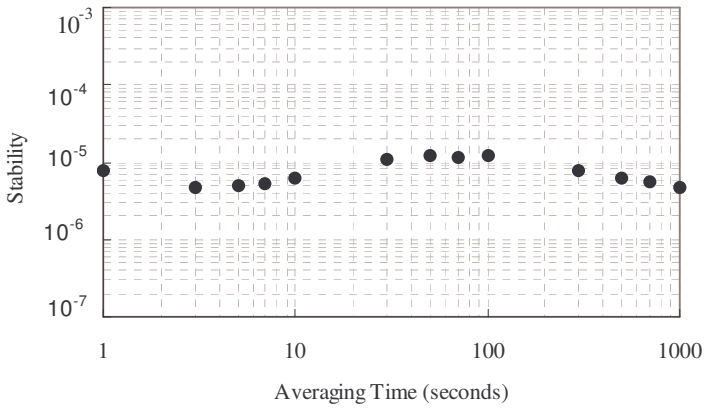

(c)

Figure 4.9 (a) The temperature data for one thermistor at 20 ^{0}C for about 7 hours (b) the histogram graph of the measurement (c) the stability graph of Allan variance analysis.

CHAPTER 5

REFRACTIVE INDEX of AIR

5.1 Introduction

In accurate interferometric measurements, it is essential to know the refractive index of ambient air with a reasonable accuracy. The refractive index of the medium affects the wavelength of the light and a correction is realized for the laser wavelength.

$$\lambda = \lambda_v / n \tag{5.1}$$

where λ is the wavelength in the air, λ_v is the wavelength in vacuum and n is the refractive index of the air.

The refractivity of a gas (n-1), can be expressed as

$$(n-1)_{T,P} = K_\lambda D_{T,P} \tag{5.2}$$

where K_λ is the dispersion factor and $D_{T,p}$ is the density factor.

The dispersion factor, K_λ is independent of the temperature and pressure variences and based on measurements of the dispersion of air. The density factor $D_{T,p}$ is based on the Lorentz-Lorentz equation and the gaseous equation of state. Further corrections were presented for humidity and Carbon dioxide content [2].

For refractive index measurements of air, two main methods are generally used. The first one is Edlèn's formula based on the measured air parameters simultaneously such as temperature, pressure and humidity. The second method is the use of refractometers with vacuum cell. In this method, the refractive index is measured by using the passed interference fringes when filling or evacuation of the vacuum cell.

5.2 The Calculation of Refractive Index of Air by Using Edlén Equation

5.2.1 The Original and Modified Edlèn Equations

5.2.1.1 The Original Edlèn Equations

The Edlèn equation (1966) is used with the highest accuracy for calculation of refractive index. The Edlèn's equation [30] for the density factor is,

$$(n-1)_{tp} = \frac{p(n-1)_s}{720.775} \times \frac{1 + p(0.817 - 0.0133t) \times 10^{-6}}{(1 + 0.0036610t)} \tag{5.3}$$

where $(n-1)_{tp}$ is refractivity of standard air, t is temperature in degrees Celsius, p is pressure in torr, $(n-1)_s$ refractivity of standard air at 1 atmosphere and 15 ^{0}C. $(n-1)_s$ is calculated from the dispersion formula [31] which was given as

$$(n-1)_s \times 10^8 = 8342.13 + 2406030(130 - \sigma^2)^{-1} + 15997(38.9 - \sigma^2)^{-1} \tag{5.4}$$

where σ is the vacuum wave number in μm^{-1}. Equations 5.2 and 5.3 are valid for standard dry air defined as 78.09% nitrogen, 20.95% oxygen, 0.93% argon and 0.03% carbon dioxide.

5.2.1.2 Modification for Water Vapour and Conversion to the SI System

For most air, the water vapour (humidity) should be taken into account and, therefore Edlèn added the following formula:

$$n_{tpf} - n_{tp} = -f(5.7224 - 0.0457\sigma^2).10^{-8} \tag{5.5}$$

where f is the partial pressure of the water vapour in torr.

Brich and Down (1988) realized some comparisons between the calculated and measured values of refractive index for dry and moist air [32,33]. They used Edlèn's equations (5.2, 5.3 and 5.4) and NPL refractometer to determine the calculated and measured refractive indexes. The experiment results showed that the differences between two methods were within the ±3 x 10^{-8} for dry air.

However, in the experiments for the moist air, this difference was found to be 13 x 10^{-8}. Brich and Down (1993) suggested an modification for the moist air part of the formula [34],

$$n_{tpf} - n_{tp} = -f(3.7209 - 0.0343\sigma^2)\times 10^{-8} \tag{5.6}$$

where *f* is Pa. The unit of the partial pressure of water vapour is converted from torr to Pa, after acceptance of the SI system. Similarly the unit of the density of air may be changed as follows,

$$(n-1)_{tp} = \frac{p(n-1)_s}{96095.43}\times\frac{1+p(0.613-0.00998t)10^{-8}}{1+0.0036610t} \tag{5.7}$$

5.2.1.3 Modification for CO_2 and Application of ITS-90 Temperature Scale

The original Edlèn equation assumes that dry air has a constant CO_2 composition of 300 ppm. Edlèn suggested a correction expression for excess levels of CO_2 as follows [30,35]:

$$(n-1)_x = [1 + 0.540(x - 0.0003)](n-1)_s \quad (5.8)$$

where x is the CO_2 concentration by volume and $(n\text{-}1)_s$ is obtained from the Edlèn dispersion equation.

However, Birch and Down applied a correction to Edlèn's equation (5.3) a correction for increased CO_2 level and accepted ITS-90 temperature scale [34]. The expression

$$(n-1)_s \times 10^8 = 8343.05 + 2406294(130 - \sigma^2)^{-1} + 15999(38.9 - \sigma^2)^{-1} \quad (5.9)$$

The recent experiments were realized between the measured values and calculated by the expressions as i) the Edlèn equation (5.2, 5.3 and 5.4), ii) the Edlèn equation after correction for excess CO_2 levels (5.7), iii) the modified Edlèn equation (5.5 and 5.6), iv) the modified Edlèn equation after correction for excess CO_2 levels (5.8) [37].

The differences were decreased for Edlèn equation after correction excess CO_2 levels. Moreover, more improvement was found for the modified Edlèn equation and particularly for modified Edlèn equation after correction for excess CO_2 levels.

5.2.1.4 Modification for Wavelengths over Visible Range

In addition to these improvements Erickson derived constants for over visible range of wavelengths from 350 nm to 650 nm [37]. The revised expression is given as:

$$n_{tpf} - n_{tp} = -f \times (3.7345 - 0.0401\sigma^2)\, x10^{-10} \tag{5.10}$$

5.2.1.5 Modification for Compressibility

Further improvements applied to equation 5.6, since the expression for the compressibility factor is revised [34]. Therefore, $(n\text{-}1)_{tp}$ is given as following:

$$(n-1)_{tp} = \frac{p\,(n-1)_s}{96095.43} \times \frac{1+10^{-8}\,(0.601-0.00972t)\,p}{1+0.0036610t} \tag{5.11}$$

5.2.1.6 The *Result* Modified Edlèn's Equations

$$(n-1)_{tp} = \frac{p\,(n-1)_s}{96095.43} \times \frac{1+10^{-8}\,(0.601-0.00972t)\,p}{1+0.0036610t} \tag{5.12}$$

$$(n-1)_s \times 10^8 = 8343.05 + \frac{2406294}{130-\sigma^{-2}} + \frac{15999}{38.9-\sigma^{-2}} \tag{5.13}$$

$$n_{tpf} - n_{tp} = -f \times (3.7345 - 0.0401\sigma^2)\, x10^{-10} \tag{5.14}$$

For converting the dewpoint temperature, T_{dp}, into the partial pressure of water vapour, f, in mbar, the below equation is used [2].

$$f = \log^{-1}\left(\frac{7.5xT_{dp}}{237.3+T_{dp}} + 0.78571\right) \tag{5.15}$$

5.2.2 The Experiment Results for Edlèn's Equations

The recorded values of refractive index of air by modified Edlèn's equation (equations 5.11-5.13) over a period of 120 minutes are shown in figure 5.1(a). The results of pressure, humidity and temperature values were taken simultaneously are seen in figure 5.1(b, c and d).

When comparing the graphics of the refractive index and pressure, very similar variation can be observed. The reason of that is the air pressure and temperature has the largest effect on the refractive index. The effects of the air temperature, pressure, humidity and CO_2 on the refractive index can be seen in Table 5.1 [2]. In our measurement, since the temperature stabilization inside of the chamber is obtained very accurately (section 4.4 and figure 5.1(c)), the results of the refractive index measurements by Edlèn's equation is mainly depending on the pressure variation.

Table 5.1 The dependence of temperature, pressure, humidity and CO_2 level on the refractive index of air.

Parameter	**Increment**	**Effect on refractive index**
temperature	1 ^{o}C	-9.26×10^{-7}
pressure	1 mbar	2.68×10^{-7}
humidity	1 mbar	-2.73×10^{-8}
CO_2 content	100 ppm	1.47×10^{-8}

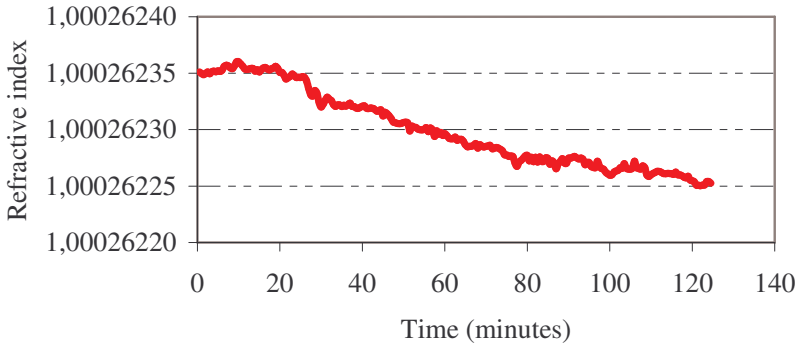
Refractive index
1,00026240
1,00026235
1,00026230
1,00026225
1,00026220
0
20
40
60
80
100
120
140
Time (minutes)

(a)

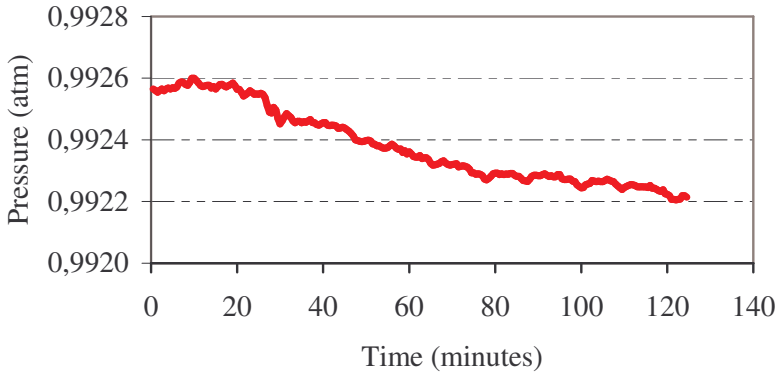
Pressure (atm)
0,9928
0,9926
0,9924
0,9922
0,9920
0
20
40
60
80
100
120
140
Time (minutes)

(b)

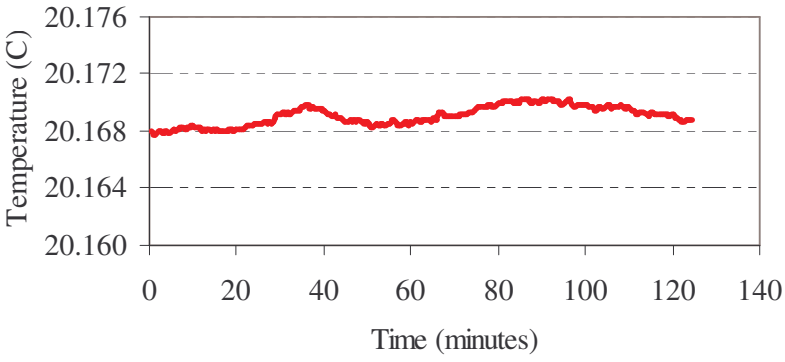
Temperature (C)
20.176
20.172
20.168
20.164
20.160
0
20
40
60
80
100
120
140
Time (minutes)

(c)

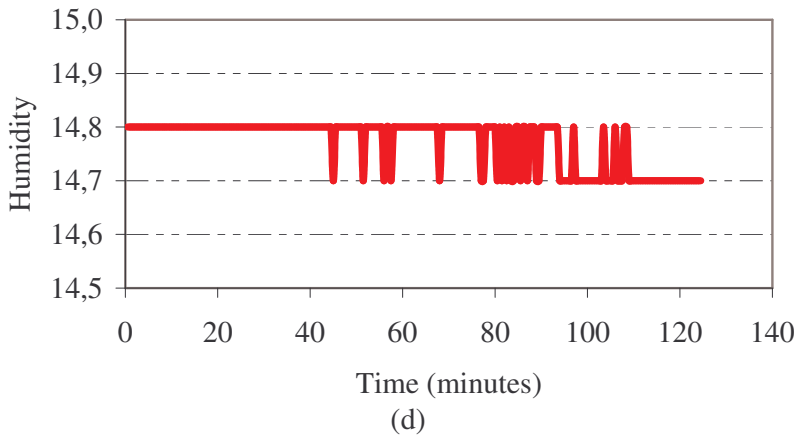

(d)

Figure 5.1 (a) The refractive index, (b) the pressure, (c) the temperature and (d) the humidity of the air inside of the chamber for about 2 hours.

5.3 The Measurement of Refractive Index of Air by Using Refractometer

5.3.1 The Design of the Refractometer

The refractometer used in this thesis is based on PTB refractometer design [26]. The refractometer consists of four channels (cells) and the ends of the refractometer are closed by special windows (Figures 5.2 and 5.3). These windows are anti reflection coated and are attached to the ends of the refractometer by using a vacuum adhesive. The two cells of the refractometer are connected to each other and to vacuum pump as shown in figure 5.2. These two cells are used as *vacuum cells*. For the other two cells, some holes are opened in the upper and lower parts to obtain the air leakage through the holes. Therefore, these two cells are used as *open cells*.

5.3.2 The Measurement Method

The refractometer is placed in the interferometer as shown in figure 5.2. Initially, the sealed cells are evacuated to vacuum and then filled with the air to be measured. During the filling of the air, the passing of interference fringes are observed, since the change in refractive index causes a change in optical path length of the sealed cell. The refractive index of the air inside interferometer is calculated by counting the passing fringes.

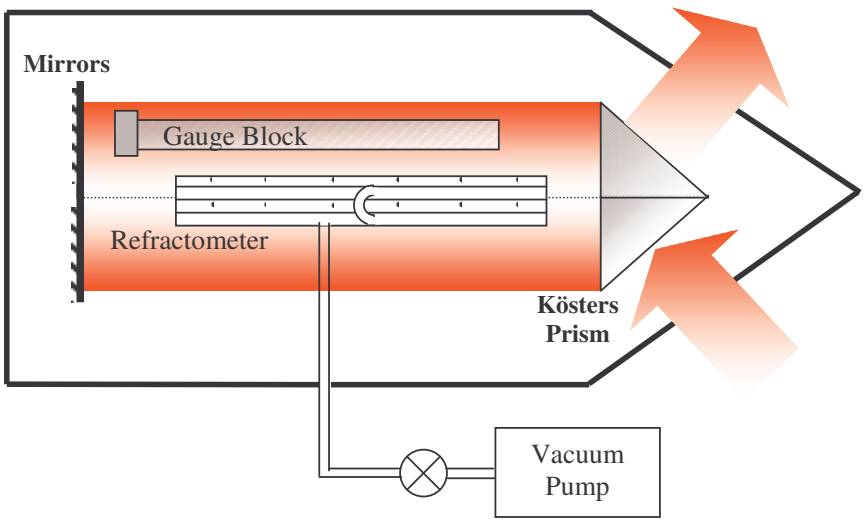

Figure 5.2 The placement of refractometer inside of the interferometer

The optical path length depends on the mechanical path length and the refractive index of the medium that is measured. This relation can be expressed as seen,

$$L_{optical} = n\,L_{mechanical} \tag{5.16}$$

A change in the refractive index or a change in the mechanical path length cause to a change in the optical path length. Hence,

$$\Delta L_{optical} = n\Delta L_{mechanical} + L_{mechanical}\Delta n \tag{5.17}$$

where $\Delta L_{optical}$ represents the change in optical path length, $\Delta L_{mechanical}$ represents the change in mechanical path length, n is the refractive index and Δn represents the change in refractive index.

Since $L_{mechanical}$ is not changed during the application, $\Delta L_{mechanical}$ will be zero, thus the first term will be zero also.

$$\Delta L_{optical} = L_{mechanical}\,\Delta n \tag{5.18}$$

As a result, the refractive index can be calculated by forming the vacuum condition as a reference (n_{vacuum}=1),

$$\Delta L_{optical} = L_{mechanical}\,(n-1) \tag{5.19}$$

Since the optical path difference is equal to $N\lambda/2$, the equation 5.19 can be used as follows,

$$n-1 = \frac{N\lambda}{2L_{mechanical}} \tag{5.20}$$

where N is the number of fringes passed, λ is the wavelength of the laser used and n is the refractive index of the air [8].

The refractometer and Köster's prism can be seen in figure 5.3. Sealed and open parts is drawn in more detail

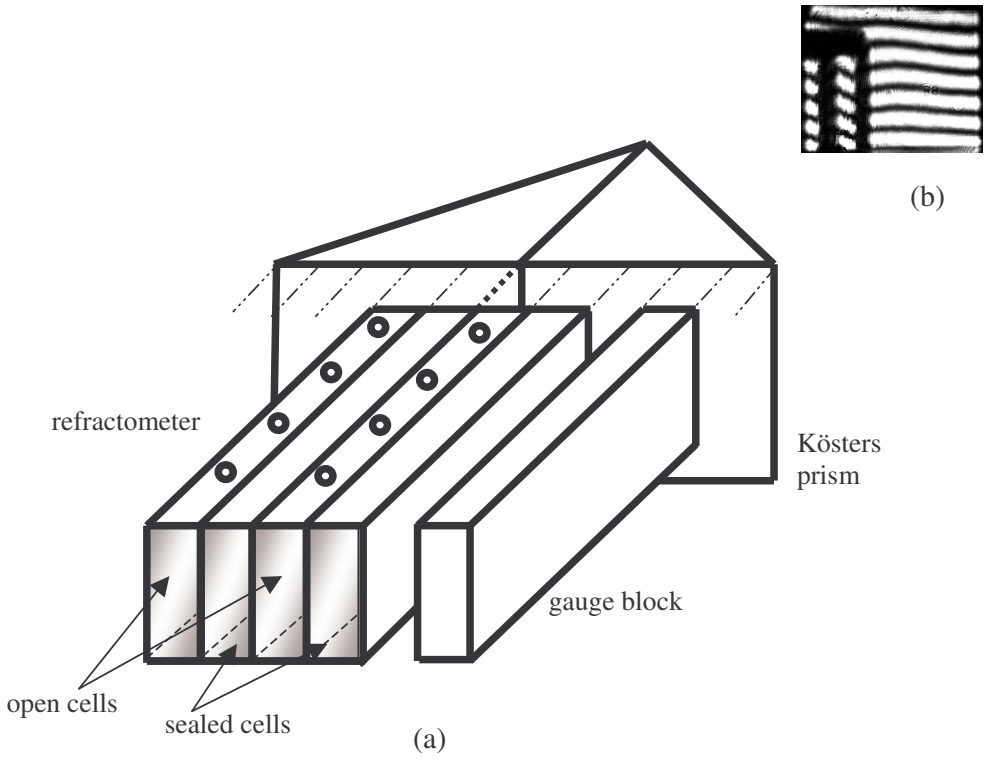

Figure 5.3 (a) The schematic diagram of the refractometer in more detail (attached windows are not shown here) and (b) the interference fringes due to the refractometer (the fringes due to the gauge block is not shown here)

In this system, a photo detector, which is connected to a voltmeter, perceives the passing fringes. The output signals of the voltmeter are recorded by a PC. The results of the signals taken for one measurement can be seen in figure 5.4. Here, each peak corresponds to one passing fringe.

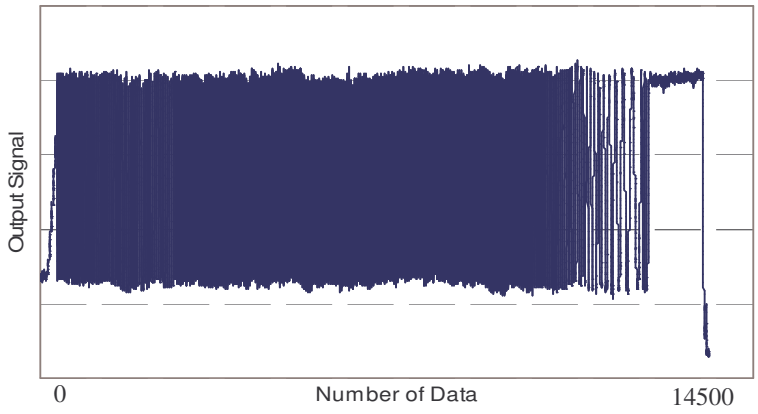

Figure 5.4 The output signals detected by a voltmeter when the fringes were passing.

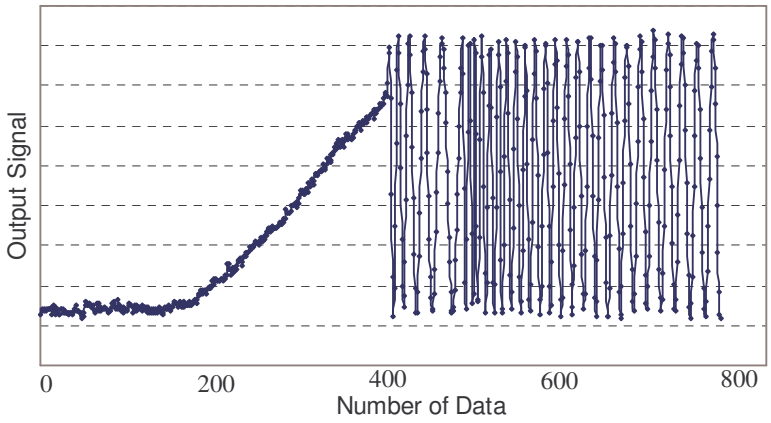

Figure 5.5 The output signals detected by voltmeter for the first 750 data. The data points in the graphs correspond to the voltmeter readings. Each peak corresponds to one passing fringes.

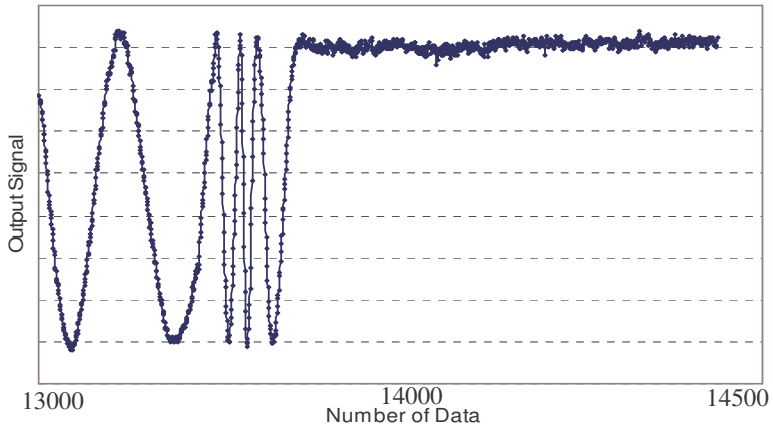

Figure 5.6 The output signals detected by voltmeter for the last about 1500 data. The data points in the graphs correspond to the voltmeter readings. Each peak corresponds to one passing fringes.

For this measurement, the number of the peaks in the graphs is counted as N=1003.5 during the filling of the air in the sealed cells. The length of the refractometer is measured as 998.8 mm using CMM and the wavelength of the laser is taken as 532.249972 nm. The refractive index is calculated as 1.000267 when these values are placed in equation 5.20.

CHAPTER 6

DATA PROCESSING

6.1 Interferogram Analysis

6.1.1 Interference Fringes and Phase Calculation

An interferogram has a periodic shape forming of destructive and constructive fringes repetition. The distance between the two constructive or destructive fringes is λ/2 (for double path interferometers). Here, λ is the wavelength of the light source. Since these interference fringes give the height information of the test object, the analysis of the fringe patterns on the basis of *their intensity* should be realized very accurately. One method is making observation by naked eye, which could detect the fringes having a resolution of λ/5 or λ/10. Another method is determining the fringe positions in more detail by digitizing interferograms, and recording in a PC. Furthermore, more accurate method, *which is* having a resolution ten to a hundred times, greater than digitizing of fringe, is phase calculation of each point in the image of interference fringes [38]. Here, the phase corresponds to the relative phase difference between the test and reference optical paths and it is ϕ(x,y) in equation 1. This phase have the height information of the test surface.

$$I(x,y,t) = a(x,y) + b(x,y)\cos\left[\phi_R(x,y,t) + \phi(x,y)\right] \tag{6.1}$$

where a(x,y) is the variation of background intensity, b(x,y) is the noise and contrast variations, ϕ(x,y) is the phase related to the surface to be measured (wavefront phase) and ϕ_R(x,y,t) is the reference phase [2].

The phase measurement over the recording interferogram supplies height information of the test surface or optical component. The fringe analysis and phase calculation are performed accurately by using computer.

6.1.2 Phase Measurement Methods

In phase measurement interferometry, first a known phase change is induced between the object and reference beams, then the interferogram is recorded and finally, wavefront phase is calculated from changes in the recorded intensity data.

The phase change means the phase modulation. The phase is shifted by a mirror, tilting a glass plate, moving a grating, rotating a half-wave-plate or analyzer, using an acousto-optic or electro-optic modulator. In these methods, the phase shifter (mirror, glass plate, grating etc) is positioned in one arm of the interferometer and interferogram is recorded [38]. The phase of one beam in the interferometer is shifted with respect to the other beam. Therefore the phase is modulated because of the phase difference between the beams.

6.2 Phase Stepping Interferometry (PSI)

In PSI techniques, the phase in the interferometer is shifted in a known amount. Since equation 6.1 includes three unknown (a, b, and ϕ), minimum three measurements (steps) are required to reconstruct the wavefront. The value of each step can be any value between 0 and π degrees.

6.2.1 Five-Frame Technique

The wavefront phase is calculated from a phase shift of $\pi/2$ (90^o) per step with

$$\phi_R = 0,\ \pi/2,\ \pi,\ 3\pi/2, \text{ and } 2\pi. \qquad (6.2)$$

The five intensity measurements at a single point in the interferograms may be expressed as

$$\begin{aligned} I_1 &= A + B + 2\sqrt{AB}\cos(\phi + 0) \\ I_2 &= A + B + 2\sqrt{AB}\cos(\phi + \pi/2) \\ I_3 &= A + B + 2\sqrt{AB}\cos(\phi + \pi) \\ I_4 &= A + B + 2\sqrt{AB}\cos(\phi + 3\pi/2) \\ I_5 &= A + B + 2\sqrt{AB}\cos(\phi + 2\pi) \end{aligned} \tag{6.3}$$

where ϕ_R may be taken as values of -2α, $-\alpha$, 0, α, 2α for R= 1 to 5 respectively. The phase at each point is calculated by using [2]

$$\phi = \arctan\left[\frac{2(I_2 - I_4)}{2I_3 - I_5 - I_1}\right]. \tag{6.4}$$

6.2.2 Removal of Phase Ambiguities

Since ϕ is calculated *by using* arctangent function, and arctangent functions give the results between the values of $-\pi/2$ and $\pi/2$, the results should adjust between the values of 0 and 2π (or $-\pi$ and π). For this reason, after the phase is calculated, the signs (+ or -) of numerator ($\sin\phi$) and denominator ($\cos\phi$) must be examined. The equation 6.4 is written simply

$$\phi = \arctan\left(\frac{a}{b}\right) \tag{6.5}$$

The phase at each point is determined by using table 1 (modula 2π).

Table 6.1. The conversion table for the phase values to be placed in unit circle [38].

a	*b*	ϕ	*In unit circle*
+	+	ϕ	1.region
+	-	$\pi-\phi$	2. region
-	+	$2\pi-\phi$	4. region
-	-	$\pi+\phi$	3. region
+	0	$\pi/2$	$\pi/2$
0	-	π	π
-	0	$3\pi/2$	$3\pi/2$
0	+ or 0	0	0

6.2.3 Phase Unwrapping Method

Since the phase calculation by computer gives values ranging from $-\pi$ to π, the phase distribution is wrapped into this range and consequently has discontinuities with 2π-phase jumps for variations more than 2π. The sawtooth function of phase angle ϕ is shown in figure [6.1(a)]. For continuing the necessary procedures of data processing, this phase jumping should be removed. This process is called 'phase unwrapping'.

For detecting the phase jumping, the phase gradient is calculated at each pixel;

$$\Delta\phi = \phi_n - \phi_{n-1} \tag{6.6}$$

where n is the pixel number. If $|\Delta\phi|$ is greater than a certain threshold such as π, then a phase jump (2π discontinuity) is detected. When the sign of $|\Delta\phi|$ is negative (the phase is increasing), 2π is added, whereas the sign of $|\Delta\phi|$ is positive (the phase is decreasing), 2π is subtracted. Therefore, the offset phase distribution that should be added or subtracted from the wrapped phase distribution is seen in figure [6.1 (b)].

As a result of phase unwrapping process, the continuous phase distribution is shown in figure [6.1(c)] [39].

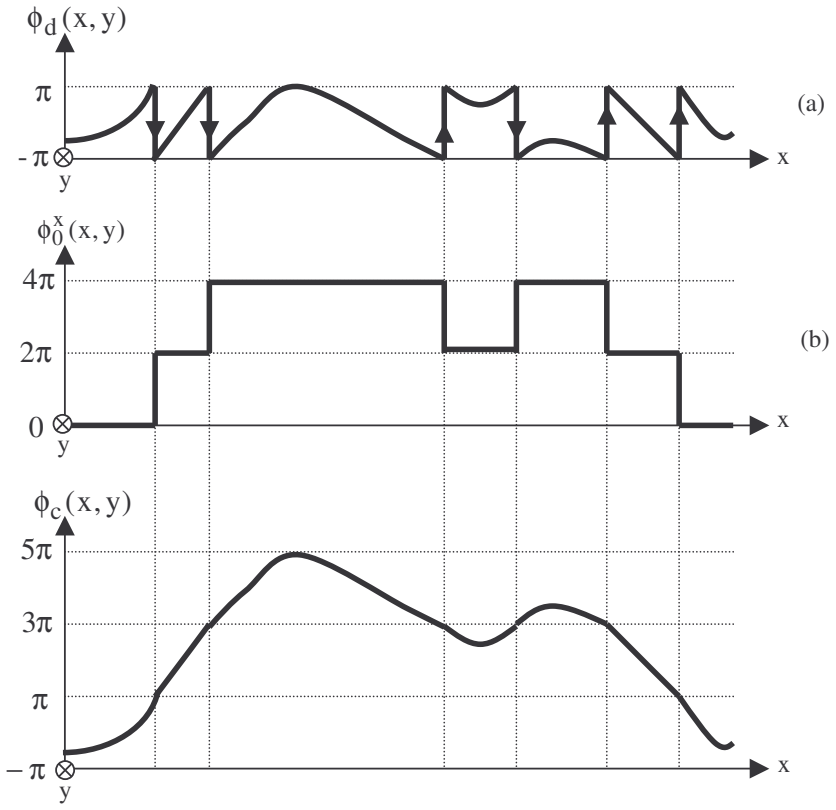

Figure 6.1 (a) Example of a phase distribution having discontinuities that are due to the principal-value calculation; (b) offset phase distribution for correcting the discontinuities in (a); (c) continued profile of the phase distribution. The y axis is normal to the figure.

6.3 Experiment

6.3.1 Theoretical Interference Fringes

The interference fringes are obtained theoretically in PC medium (by a software). Therefore the images of the interferograms without noise could be realized. Each interference fringes in Figure 6.2 correspond to different surface shapes over a reference surface. For example, Figure 6.2 (a) represents flat surface, it may be the surface of a gauge block, Figure 6.2 (b) represents a convex surface,

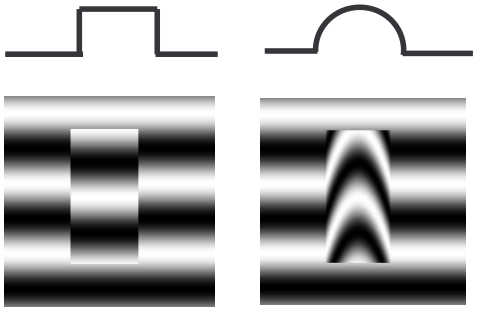

(a) (b)

Figure 6.2. The examples of theoretic interferograms correspond to different surface shapes. The upper parts represents 2D cross-sections of the surfaces, the lower parts represents the possible interference fringes correspond to these cross sections. (a) Flat surface (i.e. gauge block), (b) convex surface

The number of the fringes in one image could be changed by using the same software as shown in figure (6.3). The changeability of the fringe number is only realized for the flat surface interferogram.

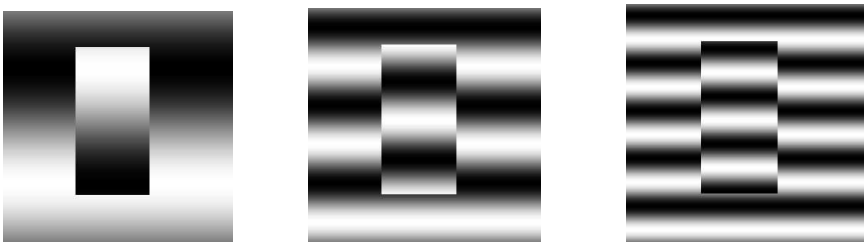

(a) (b) (c)

Figure 6.3. The examples of theoretic interferograms corresponds to different number of the fringes in one image. (a) Two fringes (b) Six fringes (c) Ten fringes.

As an example for five frame phase stepping, the theoretical interferograms and *corresponding* 3D intensity profiles are shown in Figure 6.4. The 3D intensity profiles are obtained by using Matlab program. The relative phase difference between the interferograms is $\pi/2$ (90^0). When looking at the first and last frames, their appearances are the same because of the phase shift having 2π (360^0) between them.

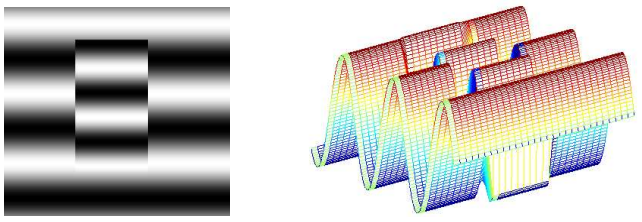

(a) $\phi_R=0$ (0^0)

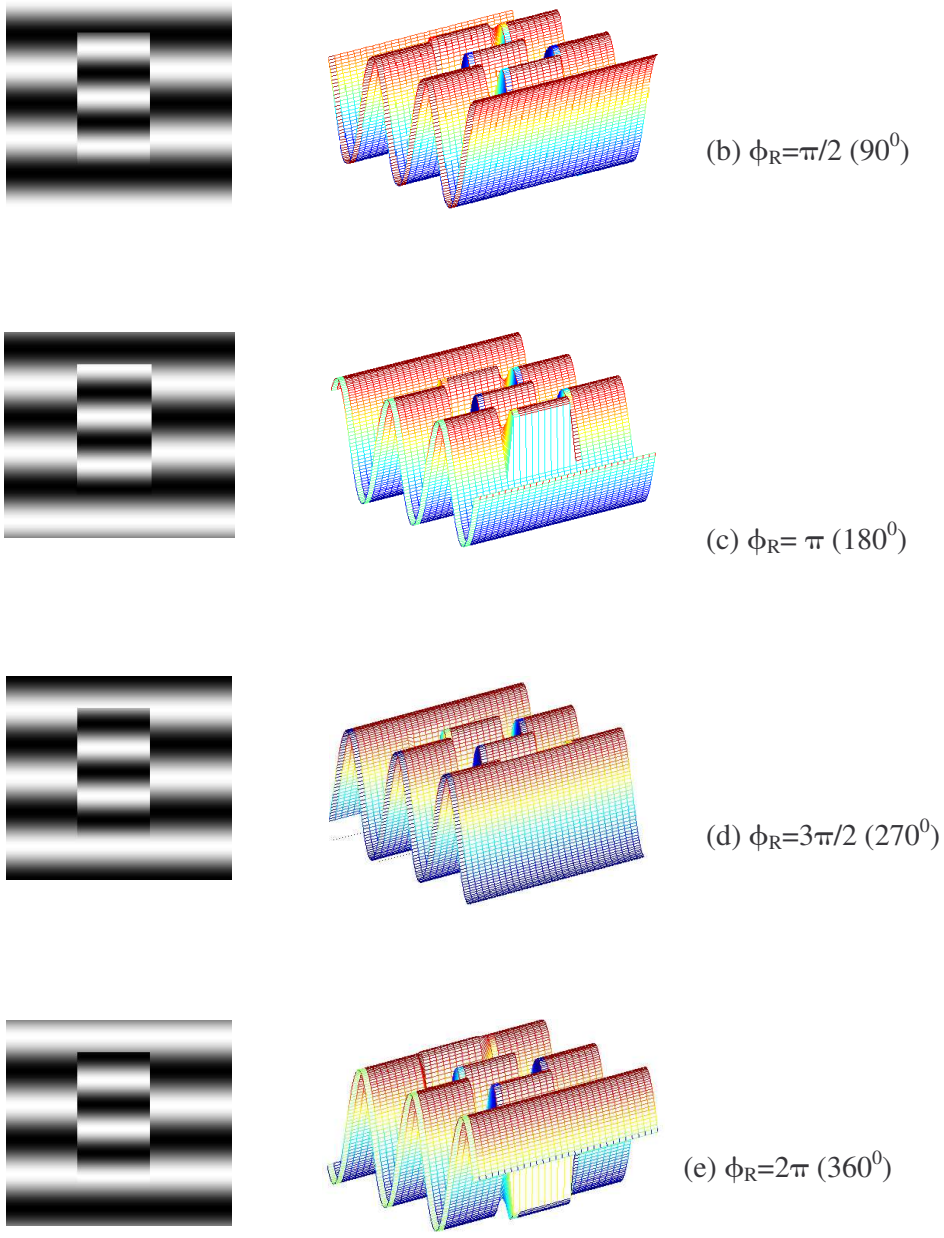

Figure 6.4. The examples of five frames for five step phase stepping method. (a) $\phi_R=0$ (0^0), (b) $\pi/2$ (90^0), (c) π (180^0), (d) $3\pi/2$ (270^0), and (e) 2π (360^0). The images in first column represent interferograms obtained by theoretically; the figures in second column represents the 3D intensity profiles respectively.

The phase ϕ is calculated by substituting of five frames intensity values in Equation 6.4. This process is realized for each point in the interferograms automatically. The calculated phase (ϕ) can be plotted versus x-y coordinates as shown in Figure 6.5. Figure 6.5(a) gives the results of arctangent function between the values of $-\pi/2$ (-90^0) and $\pi/2$ (90^0). Figure 6.5(b) represents also the arctangent function between the values 0 and 2π (360^0) by applying Table 6.1.

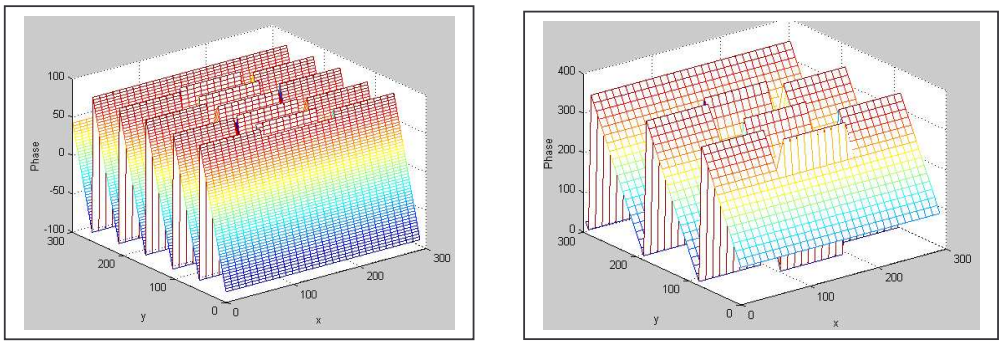

(a) (b)

Figure 6.5. The calculated phase (ϕ), (a) for between -90^0 and 90^0 (b) for between 0^0 and 360^0.

2π discontinuities are removed by using phase unwrapping algorithm as discussed in chapter 6.2.3. The phase map containing tilt is shown in Figure 6.6. The image of the wrapped phase is unwrapped by passing through y direction. After the discontinuities and their signs are detected, 2π values are added (or subtracted).

The phase map is very smooth and the height above the surface corresponds to the gauge block where as the reference surface corresponds to the platen.

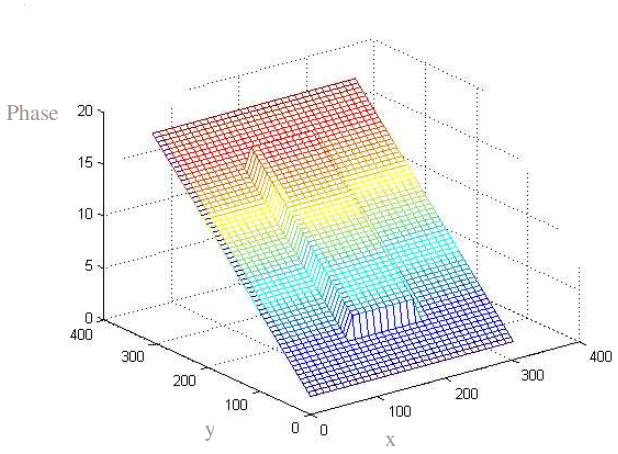

Figure 6.6 The phase map corresponds to gauge block and platen surface.

The values in the phase maps are converted to fringe fractions (as discussed in chapter 2) dividing by 2π . The fringe fractions of 20x20 pixels at the centre of the block are averaged. The same process is realized for each of the three wavelengths. These three fractions, f_1, f_2, and f_3 correspond to the 532 nm, 633 nm and 778 nm wavelengths respectively. The length of the gauge block is calculated by using the method of multiple wavelength interferometry, which combines these three fringe fractions.

6.3.2 Experimental Interference Fringes

6.3.2.1 13 mm Gauge Block

In the Figure 6.7, the interference fringes are seen for three different laser beams as ECDL/Rb (780 nm), He-Ne/I_2 Laser (633 nm) and Nd:YAG/I_2 Laser (532 nm).

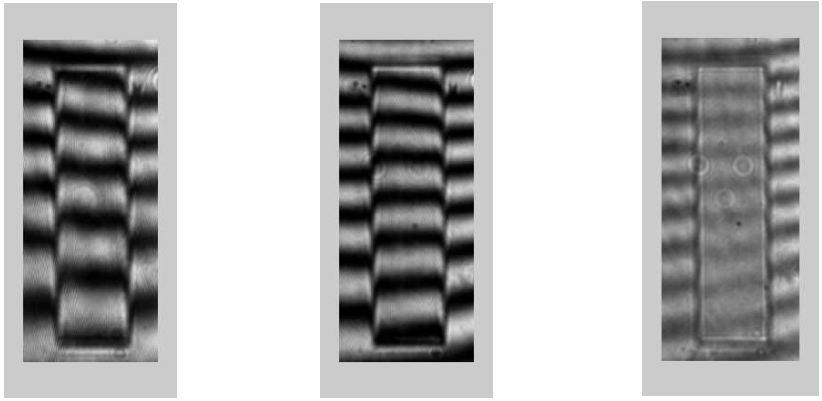

Figure 6.7. The images of interference fringes (a) ECDL/Rb (780 nm), (b) He-Ne/I_2 Laser (633 nm) (c) Nd:YAG/I_2 Laser (532 nm)

After the temperature stabilization of the system, the interference fringes are captured individually for each of the laser wavelength. The purpose is to calculate the phase of each pixel in the image of the interference fringes and then to transfer to the spatial coordinates. For this reason, the "phase stepping method (5-step)" is used that is one of the methods for calculating of the phase. In this method, the reference mirror is moved for five times between two destructive or constructive interference fringes, and the image of the fringes are captured by CCD camera at each of the step. Each step corresponds to 90^0 ($\pi/2$) that is one quarter of the distance between two destructive or constructive fringes. The images for HeNe/I_2 laser are seen in figure 6.8. As a result, totally 15 images are obtained for three different laser wavelength.

The interference fringes at each step can be seen for He-Ne/I_2 laser. The first and last frames look the same because there is a 360^0 (2π) phase shift between them.

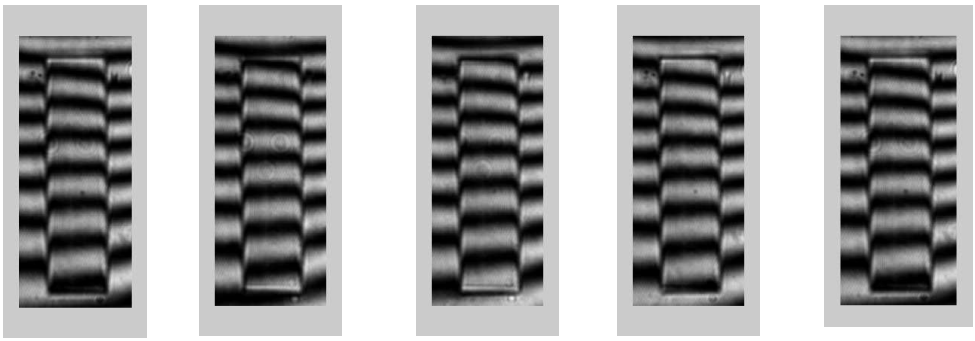

(a) (b) (c) (d) (e)

Figure 6.8 The interference fringes for five steps by using He-Ne/I_2 laser and by applying "Phase Stepping Method". (a) 0^0 (0), (b) 90^o ($\pi/2$), (c) 80^0 (π), (d) 270^0 ($3\pi/2$) and (e) 360^0 (2π)

6.3.2.2 3D Profile for Central Part of the 13 mm Gauge Block

At the stage of image analysis, initially the intensity values of five frames are obtained for each pixel over the images. After that, the phase at each point (pixel) is calculated by substituting these intensity values in a trigonometric expression (arctangent). This process is realized for frames of each of the three different lasers. In figure 6.9, the examples of 3D phase graphics that is obtained from this image analysis for He-Ne/I_2 laser can be seen. These plots are obtained only for central parts of the fringes for this measurement and consist of the gauge block and platen. This process is convenient, since at international standards, the length of the gauge block is defined as the distance between the platen and the central part of the gauge block. Meanwhile, the shifting because of the gauge block can be seen apparently.

In figure 6.9(a), it is seen that the phases are between the values of -π/2 and π/2. This is the inherent result of the arctangent calculation. Transporting of these values to the unit circle, the figure 6.9(b) is obtained. The figure 6.9(c) corresponds to the same plot in scales of degrees. At all of the figures, the shifted phase values because of the gauge block can be seen. Besides that, the figures 6.9, 6.10 and 6.11 do not correspond to the whole surface of the block and platen. These are just for about one fringe, which include the central point of the gauge block.

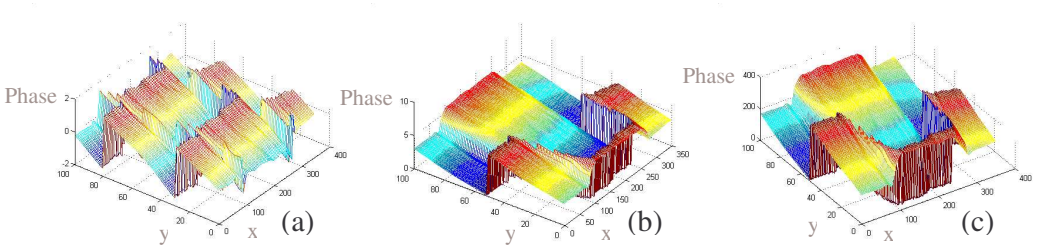

Figure 6.9 3D phase graphics obtained from the frames by using He-Ne/I_2 lasers. They cover the platen and the gauge block. (a) between -π/2 and π/2, (b) 0 and 2π, (c) 0^o and 360^o

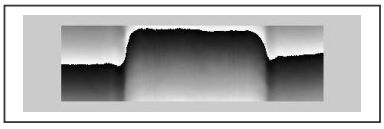

Figure 6.10 2D picture of 3D phase values after changing to intensity values.

Additionally, the "saw-tooth" wrapped phase can be seen, in Figure 6.9. This situation is inherent result of phase varying between 0 and 2π. At this stage, the

solution to this problem is to detect and then to remove the phase jumps. This process is called “phase unwrapping”. 3D phase mapping of platen and gauge block that the phase jumping is reconstructed can be seen in figure 6.10. When assuming the platen as a reference surface, the height above the surface carries information of fractional part *(f)* along the gauge block.

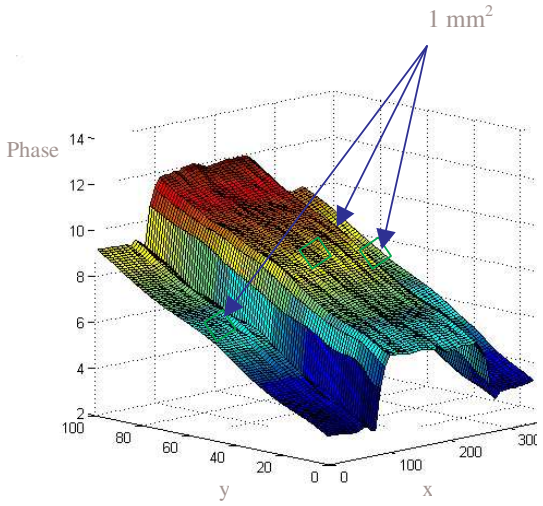

Figure 6.11 3D profile of gauge block and platen after phase unwrapping

After obtaining unwrapped phase data, small regions are chosen at the center of the gauge block and two regions symmetrically are located on the right and left platen faces as shown in figure 6.11. These regions correspond to about an area of 1 mm^2. The phase values of several pixels in each of these chosen regions are averaged. After that, firstly the phases of two regions of platens are averaged again and then subtracted from the average phase value of gauge block. The fringe fraction (*f*) is obtained by dividing of this phase value by 2π. The same process is realized for each of the three wavelengths. Finally, the three different phase values were obtained.

The exact parts (*N*) of the gauge block is calculated by using "exact fraction method". In this method three fringe fraction values that is calculated before, three different wavelengths that is used in the measurements and the nominal gauge block length that is given before are used in developed software at the same time. After some calculations, the exact parts and consequently the length of the gauge block is obtained.

6.3.2.3 3D Profile for Whole Surface of the 13 mm Gauge Block

In section 6.3.2.1 the profile is calculated for just small part of the surface as seen figure 6.11. 3D profile can also be obtained for whole surface of the gauge block.

In figure 6.12, intensity images can be seen. The first image is the intensity of the interferogram and corresponds to one step in phase stepping method. The second image is obtained after phase stepping method and the phase values converted to their intensity values. Both of them are formed for 633 nm laser.

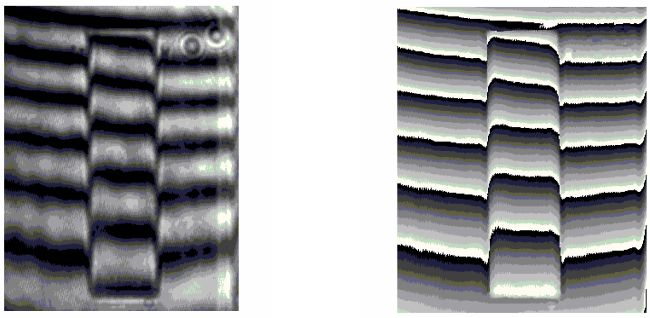

(a) (b)

Figure 6.12 (a) The image of intensity values corresponds to one step for 633 nm (b) The phase values of the fringes as intensity image for 633 nm wavelength after phase stepping method

In figure 6.13, the 3D profile of the block and platen can be seen by applying phase unwrapping method for whole surface. Because of the tilt of fringes in the original images, the tilt of the unwrapped phase map is seen. Meanwhile a small concaveness is seen in the image.

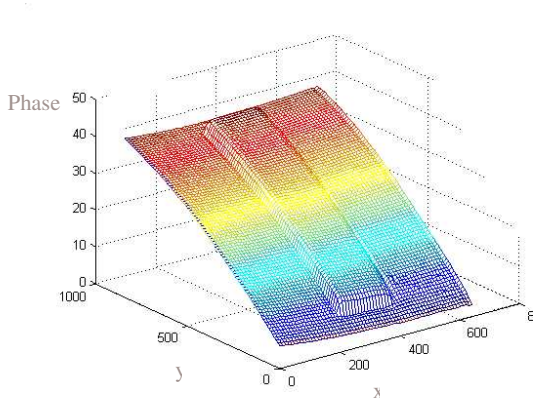

Figure 6.13 3D profile of block and platen. Concaveness is seen.

The tilt in phase map is removed by applying a surface fitting process to the platen surface and then subtracting fitted surface from the original phase map. In figure 6.14 the fitted surface to the left part of the platen is seen. The fitting process is enlarged for whole surface of the platen.

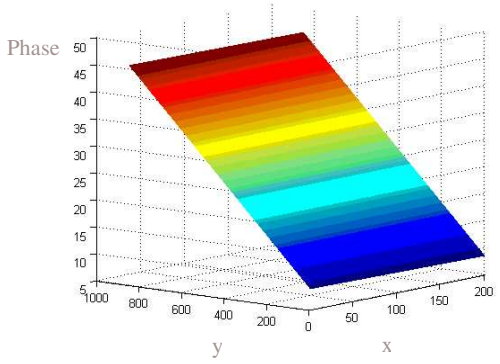

Figure 6.14 Fitted surface to the left part of the platen

In figure 6.15, the result phase map is seen by subtracting fitted surface from the original phase map. The tilt in the phase map is removed. Nevertheless the concaveness is observed in the image. The reason of this concaveness may originate from the non-equalness of the fringe spacing.

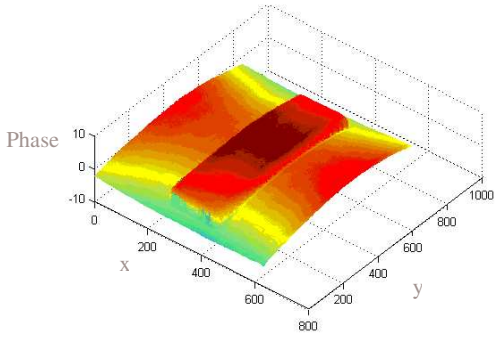

Figure 6.15 Subtracting (Figure 6.13) form (Figure 6.14). Tilt removed. However concaveness is observed.

In order to calculate the variation in length and flatness for the gauge block, this concaveness should be removed from the phase map. For this purpose, some revisions are realized in the software. (The phase values of the gauge block are subtracted from the phase values of the platen through a line.) The resulting map can be seen in figure 6.16. 3D plot corresponds to only gauge block surface for the time. The y axis corresponds to the length dimension as nanometer.

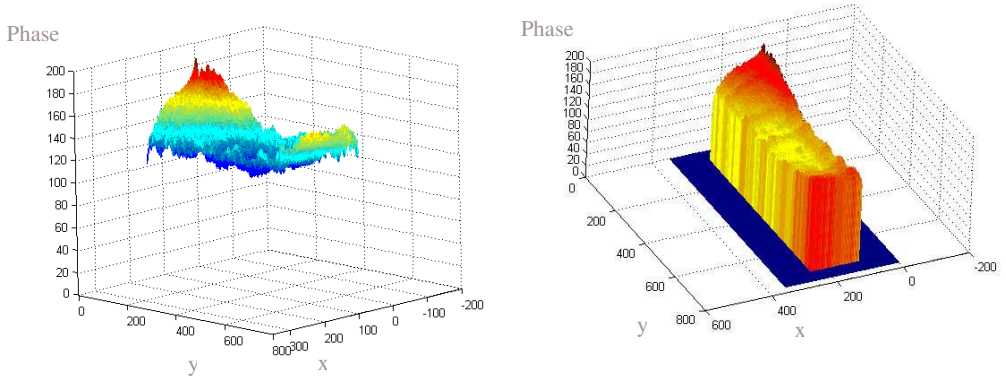

Figure 6.16 3D profile of the gauge block measurement surface.

6.3.2.4 Flatness and Variation in Length Measurements

The measurements of flatness and variation in length give rise to the information of the surface of the block and platen. The blocks are categorized by taking care of these values. Additionally, the uncertainty values of these terms are calculated for central point length measurement and added to the uncertainty budget. The basics of the "flatness" and "variation in length" are defined in the ISO 3650 standard.

Flatness (deviation from flatness) is defined as "f_d minimum distance between two

parallel planes between which all points of the measuring face lie" as shown in Figure 6.17. In general, the flatness can be calculated by taking all the fringe fractions on the surface, and fit minimum and maximum planes to them. Then the minimum distance will give the flatness value. Besides that, the easer way is to perform a least squares plane fit to the surface data, and take the maximum and minimum departure from this plane.

The calculation result of flatness for 13 mm gauge block is found as 91 nm. In our system, the flatness is calculated by taking the maximum and minimum departures from fitted plane surface

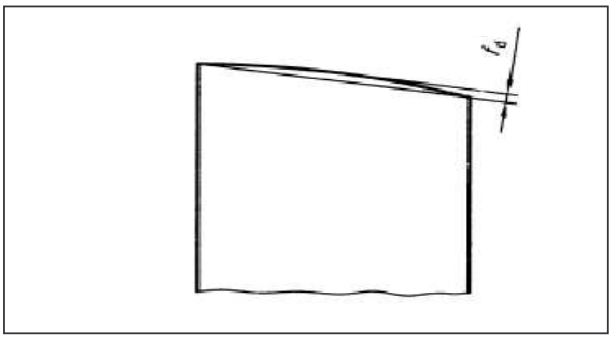

Figure 6.17 Deviation f_d from flatness

Variation in length (deviation from variation) is defined as the difference between the maximum length l_{max} and the minimum length l_{min} as shown in figure 6.18 [2]. The variation in length is calculated by taking the difference between the highest and lowest fringe fraction results on the surface. The calculation result of variation in length for 13 mm gauge block is found as 103 nm.

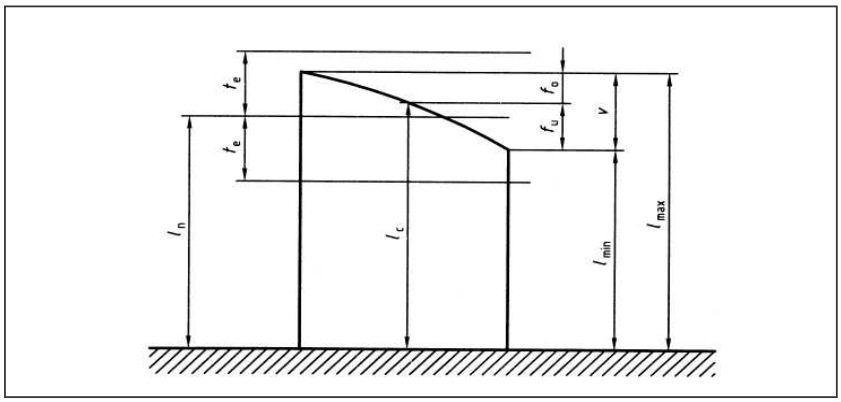

Figure 6.18 Variation in Length. Nominal length l_n; central length l_c; variation v with f_o and f_u; limit deviations t_e for the length at any point, proceeding from the nominal length.

6.3.3 Multiple Wavelength Calculation

The length of the gauge block is determined by program written in computer. This program calculates the possible solutions around the nominal length of the gauge block [40].

As discussed in previous section, the fringe fraction values (f_1, f_2, f_3) are perfectly measured for each of three wavelengths ($\lambda_1, \lambda_2, \lambda_3$). Thus, the length of the block could be determined by solving the homogeneous equation that is given below;

$$L = (N_1 + f_1)\frac{\lambda_1}{2} = (N_2 + f_2)\frac{\lambda_2}{2} = \ldots\ldots\ldots\ldots = (N_i + f_i)\frac{\lambda_i}{2} \qquad (6.7)$$

But solving this equation gives in numerous solutions. Additionally, sets of these solutions repeat at regular length interval (or the synthetic wavelength or the effective range (*ER*)) [41,42]. This effective range is determined by the laser

wavelengths that are used in interferometric measurements. However there are many possible solutions about the nominal length, there is only one correct solution that it has the best fit when considering the fraction values.

Consider that L is initially known as L_0 in an uncertainty, δL. The correct value of L could have any value from $L_0 - \delta L$ to $L_0 + \delta L$. Thus, from equation $2L = (N + f)\lambda$,

$$4\,\delta L = \Delta N\,\lambda \tag{6.8}$$

can be written. For finding of the N uniquely, $\Delta N < 1$ must be satisfied. Then equation 6.8 can be written as [43]

$$\delta L < \lambda/4 \tag{6.9}$$

The nominal length of the gauge block is given by the block supplier with calibration certificate. For instance, the uncertainty (δL) is given as ±1.5 μm by CMM measurements of 1-meter gauge blocks [2]. In this situation, the equation $N = L_0/(\lambda/2)$ would give many probable solutions in the range of the given uncertainty. Because the condition in equation 6.9 is not satisfied for uncertainty value given above with one wavelength. Using of different wavelengths could decrease the number of the solutions.

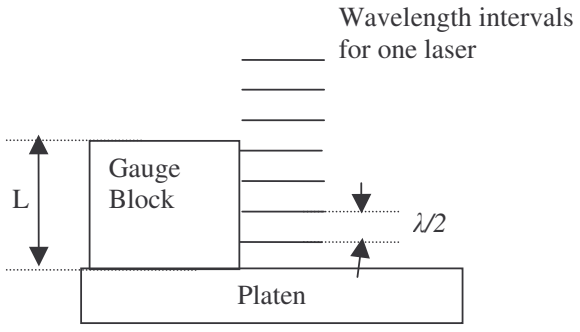

Figure 6.19 The wavelength intervals for one laser. The effective range is λ/2.

For example, if the system has only one wavelength, the effective range will be $\lambda/2$ (figure 6.19). However there may be a probable solution at each effective range, only one of them corresponds to correct solution and we should find this correct one. At this stage, it is necessary to know nominal length of the block to within half of the effective range (equation 6.9), which is approximately 150 nm. When considering δL value as ±1.5 μm, one wavelength is not sufficient to reach a correct solution.

When using two wavelengths, the effective range (*ER*) is calculated for 532 nm and 633 nm as shown below;

$$Effective \quad Range = \frac{\lambda_1 \lambda_2}{2(\lambda_1 - \lambda_2)} \tag{6.10}$$

$$= \frac{532x633}{2x(633-532)} = 1.67\mu m$$

In the meantime, an alternative method for finding the effective range is seen in table 6.2. This is prepared in MS Excel program. The red painted regions correspond to the effective range points, for the wavelengths of 532 nm and 633 nm. The effective range value is periodic through the length of the block at the points as (N1=6, N2=5), (N1=13, N2=11) and (N1=19, N2=16). Additionally, the effective range value (1.67 μm) obtained from the table is the same with the value obtained from the equation 6.10.

For these wavelengths, according to equation 6.9, ER=1.67 μm gives an estimate of the length of the block within ± 0.84 μm, which will allow unambiguous calculation of the accurate length of the block. However, when taking care of the long gauge blocks with an uncertainty of ±1.5 μm, this accuracy is difficult to achieve with these two wavelengths too.

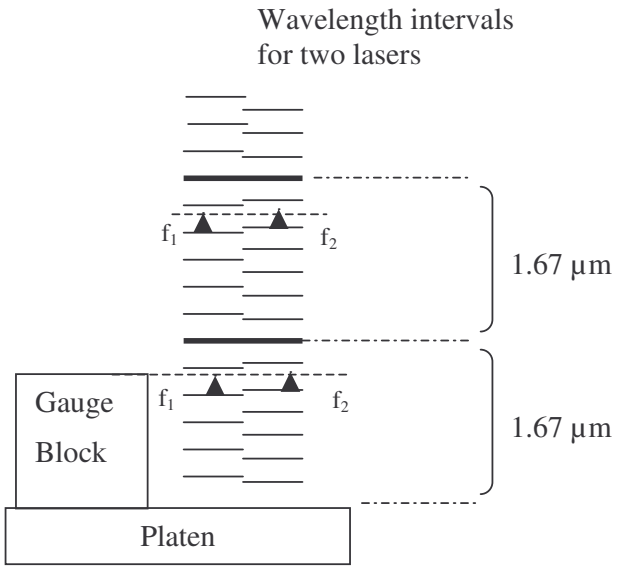

Figure 6.20 The wavelength intervals for two lasers. The effective range is 1.67 μm.

Table 6.2 The finding method of effective range for two wavelengths as 532 nm and 633 nm

λ1/2 (532/2)	N1	N1*(λ1/2)	λ2/2 (633/2)	N2	N2*(λ2/2)
266	1	266	316,5	1	316,5
266	2	532	316,5	2	633,0
266	3	798	316,5	3	949,5
266	4	1064	316,5	4	1266,0
266	5	1330	316,5	5	1582,5
266	6	1596	316,5	6	1899,0
266	7	1862	316,5	7	2215,5
266	8	2128	316,5	8	2532,0
266	9	2394	316,5	9	2848,5
266	10	2660	316,5	10	3165,0
266	11	2926	316,5	11	3481,5
266	12	3192	316,5	12	3798,0
266	13	3458	316,5	13	4114,5
266	14	3724	316,5	14	4431,0
266	15	3990	316,5	15	4747,5
266	16	4256	316,5	16	5064,0
266	17	4522	316,5	17	5380,5
266	18	4788	316,5	18	5697,0
266	19	5054	316,5	19	6013,5
266	20	5320	316,5	20	6330,0

When the third wavelength is used, this effective range will increase. As a matter of that, there exists no formula for finding effective range value for three wavelengths as equation 6.10. But similar basic calculations in MS Excel could give the effective range.

The effective range is found about 5.1 μm for three wavelengths of 532 nm, 633 nm and 780 nm. The correct solution is identified by close matches at all three wavelengths with the coincidence at N1=19, N2=16 and N3=13. In this situation, it is relatively easy to measure the length of a gauge block to within a tolerance of ± 2,5 μm (5.1μm / 2). Hence, the equation 6.9 is satisfied.

In the stage of finding the length of the block, specific software is written. In this software, taking care of the measured fringe fraction values for three wavelengths, the closest match is examined in the range of ± 9 orders of the 532 nm wavelength. The nominal length of the block gives information about which effective range will be analyzed (by dividing the nominal length by λ/2). Thus, the program gives one solution which corresponds to the length of the block.

At these tables, the given values of wavelengths are rounded values, not exact values. However, when the same calculations are realized for the exact values, it is seen that the orders are the same. So, the exact values are not given in these tables.

The laser exact values of the wavelengths used in the Köster Interferometer located in UME are as below;
ECDL/Rb Laser Wavelength: $780.2460209 \pm 0.101534 \times 10^{-6}$ nm
He-Ne/I_2 Laser Wavelength: $632.9912126 \pm 0.006683 \times 10^{-6}$ nm
Nd:YAG/I_2 Laser Wavelength: $532.2499720 \pm 0.009450 \times 10^{-6}$ nm

The measurement result for 13 mm gauge block using UME home made Köster Interferometer that is placed in UME-Wavelength Standards Laboratory is given as,
The measurement result for length of the block:

$$12\ 999\ 900 \pm Q\ (33;\ 0.8L)\ \text{nm};\ L/\text{mm}$$
$$12\ 999\ 900 \pm 43\ \text{nm}$$

where Q (33; 0.8L)=33+(0.8xL)=43 nm. The measurement result and uncertainty calculation is discussed in more detail in chapter 7 and chapter 8.

6.3.4 The Flow Diagram of Data Processing

The flow diagram of data processing corresponds to interferogram analysis and multiple wavelength analysis are seen in table 6.3.

Table 6.3 Flow diagram of data processing

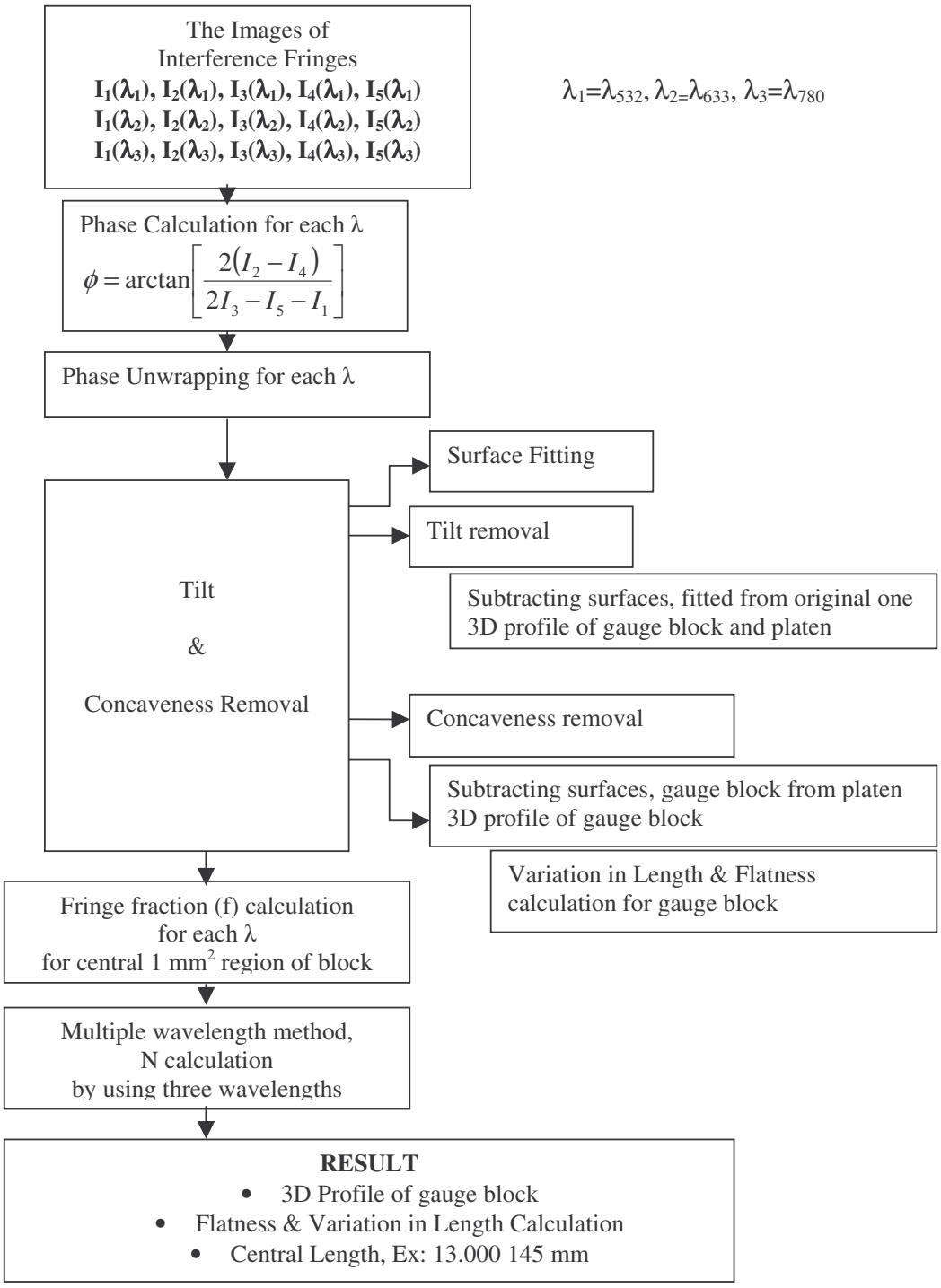

CHAPTER 7

UNCERTAINTY OF MEASUREMENTS

7.1 The Uncertainty Calculations

The uncertainty evaluation for the measurement of a gauge block by optical interferometry is given in this chapter. The uncertainties attributed to the design and operation of the instrument is considered and the total uncertainty will be the sum of many contributing uncertainties.

7.1.1 The Combined Uncertainty

The combined standard uncertainty calculation is realized with guidelines of the *ISO Guide to the Expression of Uncertainty in Measurement* (GUM 1993, revised and reprinted 1995).

The combined standard uncertainty $u_c(X)$ *is* a sum of the uncertainties $u(x_i)$ of all of the influence factors x_i, each weighted by a sensitivity coefficient c_i:

$$u_c^2(X) = \sum_{i=1}^{N} c_i^2\, u^2(x_i) + \sum_{i=1}^{N}\sum_{j=1}^{N} \left[\frac{1}{2} c_{ij}^2 + c_i\, c_{ijj} \right] u^2(x_i)\, u^2(x_j) \qquad (7.1)$$

where $u(x_i)$are the standard uncertainties attributed to the influence quantities x_i and c_i, c_{ij} and c_{ijj} are sensitivity coefficients [43-45].

$$c_i = \frac{\partial X}{\partial x_i}, \quad c_{ij} = \frac{\partial^2 X}{\partial x_i \partial x_j}, \quad c_{ijj} = \frac{\partial^3 X}{\partial x_i \partial x_j^2} \tag{7.2}$$

7.1.2 The Expanded Uncertainty

The expanded uncertainty $U=ku_c(X)$ is defined as the combined standard uncertainty multiplied by a coverage factor k. The main principle is to choose of the approximate level of confidence that is relevant to the uncertainties. In generally, measurements are expressed with a value of k between 2 and 3 [44]. UME has chosen the coverage factor as k=2, corresponding to confidence level not less than 95%.

7.1.3 The Uncertainties Due to Length Dependence and End Effects

Gauge block uncertainties can be grouped into those due to length dependent effects and those due to end effects. End effects are those arising from the quality of optical surfaces of the gauge block and their interaction with the measurement system. They are also independent of the length of the gauge block. An example for end effect uncertainties is given as wringing. Length dependent effects arise from the bulk properties of the gauge block and the surrounding medium and are independent of the end effects. For end dependent effects, the thermal expansion can be given. The uncertainty table (table 7.4) that is seen at the end of this chapter is occurred taking care of these two groups of uncertainties.

For the short gauge blocks (up to 30 mm), the main contributions in the uncertainty budget are due to the length independents factors. Besides that, for the long gauge blocks, length dependent uncertainties are more important than end dependent ones.

7.1.4 The Model Equation

A model equation is formed considering the influence parameters for measurements such as interferometry of a gauge block. The measured deviation from nominal length of the gauge block is

$$d = \ell - L \tag{7.3}$$

where L is the nominal length of the gauge block, ℓ is the measured length of the gauge block. The following model equation is convenient for presenting the uncertainty evaluation.

$$d = l_{fit} + l_t + l_n + l_\Omega + l_\phi + l_v + l_\omega \tag{7.4}$$

The best fit solution, ℓ_{fit} for gauge block length for j wavelengths of light is expressed as

$$\ell_{fit} = \frac{1}{j}\sum_{i=1}^{j}(N_i + f_i)\frac{\lambda_i}{2n} \tag{7.5}$$

where f_i is measured interference fringe fraction, N_i represents an integral count of interference orders for the gauge length and n represents the refractive index of the air.

The gauge block temperature correction, ℓ_t is determined as seen,

$$\ell_t = \alpha L \Delta t \tag{7.6}$$

where α is the thermal expansion coefficient, $\Delta t = 20 - t$, t is the gauge block temperature in degrees Celsius and $20\ ^oC$ is the ISO standard reference temperature for length measurements.

The correction for refractive index, ℓ_n is expressed as seen,

$$\ell_n = (n-1)L \tag{7.7}$$

where n is the refractive index of air that is calculated using modified version of the Edlen equation.

The correction of obliquity effect (ℓ_Ω) due to the size of light source is expressed,

$$\ell_\Omega = \Omega L$$

$$\ell_\Omega = \left(\frac{a^2}{16 f^2}\right) L \tag{7.8}$$

where a is the aperture diameter and f is the focal length of the collimating lens.

The correction of gauge block geometry (ℓ_v) accounts for non-flatness and variation in length of the gauge block. The correction (ℓ_ϕ) is phase correction and represents both the surface roughness and the phase change on reflection. The correction (ℓ_w) corresponds to the thickness of the wringing film.

7.2 Uncertainty Evaluations

7.2.1 Uncertainty Evaluation of ℓ_{fit}

The following expression can be written by applying the equation 7.1 to equation 7.5,

$$u_c^2(l_{fit}) = c_N^2 u^2(N) + c_f^2 u^2(f) + c_\lambda^2 u^2(\lambda)$$

$$u_c^2(l_{fit}) = \left(\frac{\partial l_{fit}}{\partial N}\right)^2 u^2(N) + \left(\frac{\partial l_{fit}}{\partial f}\right)^2 u^2(f) + \left(\frac{\partial l_{fit}}{\partial \lambda}\right)^2 u^2(\lambda) \tag{7.9}$$

where N is exact multiple part of the wavelength for the gauge block as discussed before and if N is found as incorrectly, this situation is taken as not an uncertainty it will be considered as a blunder by *ISO Guide to the Expression of Uncertainty in Measurement*. Thus u(N)is taken as zero.

Thus, the equation (7.9) can be written as shown below,

$$u_c^2(l_{fit}) = \left(\frac{\partial l_{fit}}{\partial f}\right)^2 u^2(f) + \left(\frac{\partial l_{fit}}{\partial \lambda}\right)^2 u^2(\lambda) \tag{7.10}$$

The combined standard uncertainty is evaluated by taking the partial derivatives of the equation 7.5.

$$u_c^2(l_{fit}) = \sum_{i=1}^{j}\left(\frac{\lambda_i}{2j}\right)^2 u^2(f_i) + \sum_{i=1}^{j}\left(\frac{N_i + f_i}{2j}\right)^2 u^2(\lambda_i) \tag{7.11}$$

By using the relation of $(N_i / f_i)/2j = L/(j\lambda_i)$, the second term of equation (7.11) can be rewritten as seen below,

$$u_c^2(l_{fit}) = \sum_{i=1}^{j}\left(\frac{\lambda_i}{2j}\right)^2 u^2(f_i) + \sum_{i=1}^{j}\left(\frac{L}{j\lambda_i}\right)^2 u^2(\lambda_i) \tag{7.12}$$

where u(f) is the standard uncertainty in reading a fringe fraction that is determined experimentally and taken as 0.01. Additionally, i is equal to 3, since three wavelengths are used and their exact values and standard uncertainties are given table 7.1.

Table 7.1 The laser wavelengths and their standard uncertainties.

Lasers	Wavelengths (nm)	Standard Uncertainties (nm)
NdYAG Laser	532. 249 972 0	0.00945×10^{-6}
HeNe Laser	632. 991 212 6	0.00668×10^{-6}
ECDL Laser	780. 246 020 9	0.10153×10^{-6}

By substituting these values in equation (7.12),

$$u_c^2(l_{fit}) = \sum_{i=1}^{3}\left(\frac{\lambda_i}{2.3}\right)^2 u^2(f_i) + \sum_{i=1}^{3}\left(\frac{L}{3.\lambda_i}\right)^2 u^2(\lambda_i) \qquad (7.13)$$

$$= [3.\ 59 + (0.19\text{x}10^{-20}\ L^2)]\ nm^2$$

7.2.2 Uncertainty Evaluation of ℓ_t

The combined uncertainty due to the temperature effects can examine in two parts. One of them corresponds to gauge block temperature measurements, the other one corresponds to thermal expansion coefficients. These two components can be seen below by taking the partial derivatives of ℓ_t,

$$u_c^2(\ell_t) = u^2(\alpha)L^2(\Delta t)^2 + \alpha^2 L^2 u^2(\Delta t) \qquad (7.14)$$

where $u(\alpha)$ is the uncertainty of thermal expansion coefficient for the gauge material. This value and also thermal expansion coefficient (α) value are provided and given with the calibration certificate by the gauge manufacturer.

7.2.2.1 Uncertainty in the Thermal Expansion Coefficient

The first component in equation (7.14) corresponds to uncertainty in thermal expansion coefficient.

$$u^2(\alpha)L^2(\Delta t)^2 \qquad (7.15)$$

The uncertainty of thermal expansion coefficient for steel gauge block is taken as $u(\alpha) = 1x10^{-6}(1/K)$. The temperature difference from 20 ^{o}C is Δt =0.3796 ^{o}C for current experiment. Substituting these values in equation (7.15), the contribution of the variance terms to the combined standard uncertainty in lengths is

$$u^2(\alpha)L^2(\Delta t)^2 = [1.44\text{x}10^{-13}\ \text{L}^2]\ \text{nm}^2 \qquad (7.16)$$

7.2.2.2 Uncertainty in the Gauge Block Temperature Measurement

The second component in equation (7.14) corresponds to uncertainty in gauge block temperature measurement.

$$\alpha^2 L^2 u^2(\Delta t) \tag{7.17}$$

The thermal expansion coefficient for steel gauge block is $11.5\text{x}10^{-6}$ (1/K). The combined standard uncertainty of temperature measurement based on thermistor calibration and performance is given as 2 mK. The thermistors are calibrated in the Temperature Laboratory at UME with standard platinum resistance thermometer that is traceable to ITS90 scale.

$$\alpha^2 L^2 u^2(\Delta t) = [5.29\text{x}10^{-16}\ \text{L}^2]\ \text{nm}^2 \tag{7.18}$$

7.2.3 Uncertainty Evaluation of ℓ_n

The refractive index (n_{tpf}) of the air is calculated by using Edlèn's equations (5.12, 5.13 and 5.14). n_{tpf} can be written by combining these three equations:

$$\begin{aligned}(n-1)\times 10^8 = &\left(\frac{p}{96095.43}\right)\times\left(8343.05+\frac{2406294}{130-\sigma^2}+\frac{15999}{38.9-\sigma^2}\right)\\ &\times\left[\frac{1+10^{-8}(0.601-0.00972t)\,p}{1+0.0036610t}\right]-f\left(0.037345-0.000401\sigma^{-2}\right)\end{aligned} \tag{7.19}$$

The combined standard uncertainty $u_c(\ell_n)$ in the length correction $\ell_n = (n-1)L$ is determined by applying equation 7.1 to ℓ_n. The **term** of (n-1) can be expressed as in equation 7.3.

$$u_c^2(\ell_n) = c_p^2 u^2(p) + c_t^2 u^2(t) + c_f^2 u^2(f) + c_\lambda^2 u^2(\lambda) \tag{7.20}$$

The sensitivity coefficients are calculated by partial derivatives of the n_{tpf}:

$$c_p = \frac{\partial \ell_n}{\partial p},\ c_t = \frac{\partial \ell_n}{\partial t},\ c_f = \frac{\partial \ell_n}{\partial f},\ c_\lambda = \frac{\partial \ell_n}{\partial \lambda} \tag{7.21}$$

The partial derivatives can be written as following:

$$\frac{\partial \ell_n}{\partial p} = \left(8343.05 + \frac{2406294}{130 - \sigma^{-2}} + \frac{15999}{38.9 - \sigma^{-2}}\right) \times \left(\frac{10^{-8}}{96095.43}\right) \times \left[\frac{1 + 2 \times 10^{-8}(0.601 - 0.00972t)\,p}{1 + 0.0036610t}\right] xL \tag{7.22}$$

$$\frac{\partial \ell_n}{\partial t} = \left(8343.05 + \frac{2406294}{130 - \sigma^{-2}} + \frac{15999}{38.9 - \sigma^{-2}}\right) \times \left(\frac{10^{-8}}{96095.43}\right) \times L \left[\frac{10^{-8} \times (-0.00972)(1 + 0.0036610t)p^2 - 0.003661\left(p + 10^{-8} \times (0.601 - 0.00972t)p^2\right)}{(1 + 0.00366610t)^2}\right] \tag{7.23}$$

$$\frac{\partial \ell_n}{\partial f} = \left(-3.7345 + 0.0401\sigma^{-2}\right) \times Lx10^{-10} \tag{7.24}$$

$$\frac{\partial \ell_n}{\partial \lambda} = \left(\frac{p + 10^{-8} \times (0.601 - 0.00972t)p^2}{1 + 0.0036610t}\right) \times \left(\frac{10^{-8}}{96095.43}\right) xL \times \left[\frac{2 \times 2406294\lambda}{\left(130 - \lambda^2\right)^2} + \frac{2 \times 15999\lambda}{\left(38.9 - \lambda^2\right)^2} + \left(0.0401 \times 2 \times 10^{-10} f\,\lambda\right)\right] \tag{7.25}$$

where λ is equal to $1/\sigma$.

By substituting the mean values of the temperature, pressure and humidity values taken during the experiment (5.2.2): t = 20.168 °C, p = 99 257 Pa, f = 1 136 Pa and λ=0.532 μm.

Sensitivity coefficients of refractive index of air depending on certain parameters are

calculated using the equations 7.22, 7.23, 7.24 and 7.25 and given in table 7.2. The mean values of the temperature, pressure and humidity values taken during the experiment are substituted in these equations (5.12, 5.13 and 5.14): t = 20.168 ^{o}C, p=99 257 Pa, f = 1 136 Pa and λ=0.532 μm.

Table 7.2 Sensitivity coefficients of refractive index of air depending on certain parameter.

	Verified Edlen Equation	unit
$\partial \ell_n / \partial p$	2.7 x 10^{-9} L	Pa^{-1}
$\partial \ell_n / \partial t$	-8.9 x 10^{-7} L	K^{-1}
$\partial \ell_n / \partial f$	-3.7 x 10^{-10} L	Pa^{-1}
$\partial \ell_n / \partial \lambda$	1.6 x 10^{-6} L	μm^{-1}

The measurement instruments were calibrated at UME – Pressure, Temperature and Humidity Laboratories. The given standard uncertainties for the instruments of temperature, pressure, humidity and wavelength as given in table 7.3. Meanwhile, in the last row in table, the term of “equation” represents the uncertainty of the revised equation stated by the authors.

Table 7.3 The standard uncertainties of the parameters affect the air refractive index.

	value	Unit
u(p)	4	Pa
u(t)	2	K
u(f)	24	Pa
$u(\lambda)$	$9.45\text{x}10^{-12}$	μm
Equation	$3\text{x}10^{-8}$	

The combined standard uncertainty attributed to the refractive index calculation are evaluated by using equation 7.20 and making substitutions of the values given in table 7.2 and 7.3.

$$u_c^2(\ell_n) = (1.095\text{x}10^{-15}\,\text{L}^2)\ \text{nm}^2 \tag{7.26}$$

7.2.3.1 The Experiment Results for Edlen and Refractometer

The refractive index value is calculated as $1.00026234 \pm 3.3\text{x}10^{-8}$ through the Edlen formula and measured as $1.000267 \pm 6\text{x}10^{-6}$ by the refractometer. The results indicate a difference of $5\text{x}10^{-6}$. Approximately fifteen refractive indices were measured and calculated, and all the differences obtained are in the range of 10^{-6}. We would like to note that a difference in the range of 10^{-7} is observed in the results of other metrology laboratories. This difference of $5\text{x}10^{-6}$ in our refractive index measurement is probably caused by the refractometer, especially from counting of the fringe numbers.

7.2.4 Uncertainty Evaluation of ℓ_v

In our system, the flatness is calculated by taking the maximum and minimum departures from fitted plane surface as explained in chapter 6.3.2.4. The calculation result of flatness for 13 mm gauge block is found as 91 nm. The variation in length is calculated by taking the difference between the highest and lowest fringe fraction results on the surface. The calculation result of variation in length for 13 mm gauge block is found as 103 nm.

The uncertainty calculation from deviations in gauge block geometry by non flatness and parallelism are realized by considering the largest variation in central length. As shown in figure 7.1, non- parallelism (variation in length) has a larger effect for the central length measurement than a deviation from flatness. Additionally, non-parallelism will be more effective in the crosswise direction than in the lengthwise direction. For this reason the crosswise direction (9 mm) is taken as shown in figure 7.1 [40].

When calculating the uncertainty term of variation in length and flatness values, the central region of the gauge block surface should be considered. Because the length of the block is measured by taking care of the central region of the gauge block.

The size of the central region is a compromise between a large enough area to reduce noise, and a small enough area so that variations in surface topography do not contribute to the average phase. For this reason, 1mm x 1 mm square area is chosen for central region in length measurement of gauge block.

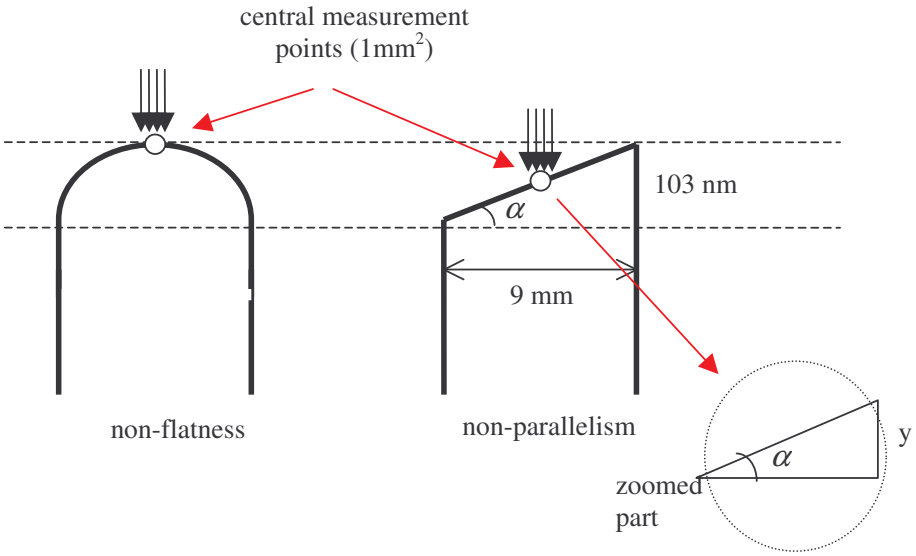

Figure 7.1. The variation in length and flatness properties of a gauge block. The effect of variation in length is larger than the effect of flatness for central point length measurement (for small angles, *tan α =sin α*).

The uncertainty in pointing to the centre of the gauging surface is 0.5 mm. Using similar triangles, the central length difference for a 103 nm deviation in variation in length along the crosswise direction of the gauge is

$$\tan\alpha = \frac{103\,nm}{9\,mm} = \frac{y}{0.5\,mm} \tag{7.27}$$

and the *y* is equal to 5.7 nm which is uncertainty term for variation in length (for small angles, *tan α =sin α*). Sensitivity coefficient for this term is 1.

$$u(\ell_y) = 5.7\,nm$$

7.2.5 Uncertainty Evaluation of ℓ_Ω

The end of the fiber is exactly placed at the focal point of the collimator. Thus, the fiber end is considered as the light source of the interferometer. The source diameter can be taken as 5 μm that is the diameter of the fiber. There is an obliquity effect due to the finite size of the source.

The combined standard uncertainty is evaluated by partial derivative of equation H. The partial derivative due to the f is negligible.

$$u_c^2(\ell_\Omega) = \left(\frac{aL}{8f^2}\right) u^2(a) \tag{7.28}$$

where a is the source diameter and equal to 5 μm, f is the focal length of the collimator and equal to 1500 mm, *u(a)* is the uncertainty of the fiber diameter and taken as 0.05 μm that corresponds to 1% of the fiber diameter. When substituting these values in the equation I,

$$u_c^2(\ell_\Omega) = (1.\ 93\text{x}10^{-28}\,\text{L}^2)\ \text{nm}^2 \tag{7.29}$$

7.2.6 Uncertainty Evaluation of ℓ_ϕ

Since the measurement of surface roughness is not realized in UME Köster interferometer, the theoretical value is used for this correction [2].

Table 7.4 Uncertainty Table

Uncertainty Sources			Partial Uncertainties				Sensitivity Coefficients					Partial Variances			
Definition	Symbol	Estimated Value c	Unit	Symbol	Value	Unit	Deviation Function	Coeff	Symbol	Value		Unit	Value		Unit
Fringe Fraction															
Fraction (λgreen)	Fg	0.1080	fringe	Ufg	0.01	fringe	N., k=1	1	C_{F_g}	88.68	-	nm	7.86E-01		nm^2
Fraction (λred)	Fr	0.3787	fringe	Ufr	0.01	fringe	N., k=1	1	C_{F_r}	105.47	-	nm	1.11E+00		nm^2
Fraction (λdiode)	Fd	0.3670	fringe	UFd	0.01	fringe	N., k=1	1	C_{F_d}	130.01	-	nm	1.69E+00		nm^2
Fraction (total)													**3.59E+00**		**nm^2**
Wavelength															
λgreen	λg	532.108059066	nm	$U_{\lambda g}$	9.45E-09	nm	N., k=1	1	$c_{\lambda g}$	6.26E-04	L	nm	3.50E-23	L^2	nm^2
λred	λr	632.822439195	nm	$U_{\lambda r}$	6.68E-09	nm	N., k=1	1	$c_{\lambda g}$	5.27E-04	L	nm	1.24E-23	L^2	nm^2
λdiode	λd	780.037985187	nm	$U_{\lambda d}$	1.02E-07	nm	N., k=1	1	$c_{\lambda d}$	4.27E-04	L	nm	1.88E-21	L^2	nm^2
λ (total)													**1.92E-21**	**L^2**	**nm^2**
Integer Value															
Integer Value (λgreen)	Ng	48862	nm	U_{Ng}	0	nm			C_{Ng}	-			-		
Integer Value (λred)	Nr	33331	nm	U_{Nr}	0	nm			C_{Nr}	-			-		
Integer Value (λdiode)	Nd	41085	nm	U_{Nd}	0	nm			C_{Nd}	-			-		
Temperature Effects															
Block Temperature (difference from 20	Δt	19.6204	°C	$U_{\Delta t}$	2.00E-03	°C	N., k=1	1	$C_{\Delta t}$	1.15E-05	L	nm	**5.29E-16**	**L^2**	**nm^2**
Expansion Coefficient	α	0.0000115	1/°C	U_{α}	1.00E-06	1/°C	N., k=1	1.00	C_{α}	0.3796	L	nm	**1.44E-13**	**L^2**	**nm^2**
Refractive Index	δln	1.000266699	-	Ul_n	3.3E-08	-	N., k=1	1	Cl_n	1	L	nm	**1.09E-15**	**L^2**	**nm^2**
Source Diameter	δlΩ	0	nm	$U_{B\Omega}$	5.00E-05	nm	N., k=1	1	$C_{B\Omega}$	2.78E-10	L	nm	**1.93E-28**	**L^2**	**nm^2**
Phase Correction															
Phase Change	δlpc	0	nm	U_{Bpc}	4.40E+00	nm	N., k=1	1	C_{Bpc}	1		nm	**1.94E+01**		**nm^2**
Roughness Correction	δlr	0	nm	U_{Br}	-1.40E+01	nm	N., k=1	1	C_{Br}	1		nm	**1.96E+02**		**nm^2**
Variation in length	δlv	0	nm	U_{Bp}	5.70E+00	nm	N., k=1	1.00	C_{Bp}	1		nm	**3.25E+01**		**nm^2**
Wringing	δlw	0	nm	U_{Bw}	5.30E+00	nm	N., k=1	1	C_{Bw}	1		nm	**2.81E+01**		**nm^2**
									TOTAL VARIATION			u_l^2 =	2.80E+02	+ 1.46E-13	**L^2** **nm^2**
Measured Value	L	12999900	nm						Standard Uncertainty			u_l =	1.67E+01	+ 3.82E-07	L **nm**
									Expanded Uncertainty			u_l =	3.34E+01	+ 7.63E-07	L **nm**
									(k=2,%95)					0.76	
Certificated Value	L=	12999900	±	Q(33;0,8L)		nm	k=2		Declarated Value			u_l =	Q(33;0,8L)	nm Lmm	

CHAPTER 8

CONCLUSION and DISCUSSION

In this work, a new interferometer system that measures the lengths of the gauge blocks has been proposed. The values of flatness, variation in length and also 3D surface profile of the blocks can be given as a result of this study. For the time being, the length of 13 mm gauge block is measured in the system and the results are presented. Additionally, the experimental result is compared by using the short gauge block interferometer that is purchased from NPL (National Physics Laboratory of England)-TESA. The results have shown that very close values are obtained at this comparison and the lengths of the long gauge blocks such as 1000 mm could be measured by using this instrument.

The measurement result for 13 mm gauge block using UME home made Köster Interferometer that is placed in UME-Wavelength Standards Laboratory is given as,

The measurement result for length of the block:

$$12\ 999\ 900 \pm Q\ (33;\ 0.8L)\ \text{nm};\ L/\text{mm}$$

$$12\ 999\ 900 \pm 43\ \text{nm}$$

Besides that, as mentioned before**,** the length of the block is measured using NPL-TESA GBI (Gauge Block Interferometer). This interferometer is placed in another laboratory that is UME-Dimensional Laboratory and the measurement result for the same block is given as

12 999 890 ± Q (25; 0.4L) nm; L/mm

12 999 890 ± 30 nm

As seen from the results and figure 8.1, very close values of the length of the block are obtained. Similarly, the difference between the uncertainty values is also very close. The small difference in uncertainty value corresponds to dissimilarities of the interferometer systems.

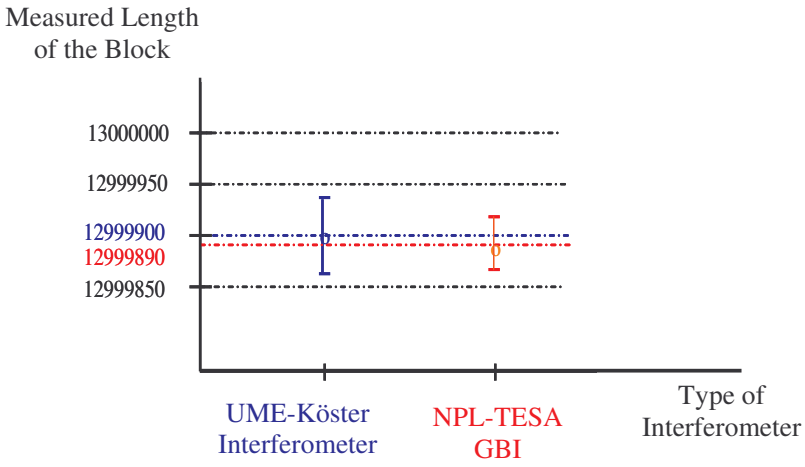

Figure 8.1 The comparison graph of the measurement results between UME-Köster Interferometer and NPL-TESA GBI.

For UME Köster interferometer, specific software is developed. This software includes of data processing of digitized images with the techniques for phase wrapping removal and surface fitting. Thus, the fractions which are needed to obtain the length of the block are obtained by image processing techniques. Additionally,

the software for multiple wavelength method in order to combine three wavelengths allows accurate calculation of the length of the blocks. In this specific software, the flatness and variation in length is calculated and the 3D surface profile of the end surface of the blocks is extracted. Further, the software and interconnections to the computer used for the refractive index calculation are prepared during this thesis study. Although the whole software works correctly, it needs some improvements for providing visual format to the user. This revision of software would decrease the data processing time and also be very user-friendly.

It is very important to have temperature stabilization of the chamber in gauge block length measurements. Reaching to the temperature stabilization of the huge interferometric systems is a time consuming process. In our case, UME Köster interferometer system reaches to that condition at most in 15 hours. There occurs no drift in the temperature for 2 hours after the system reaches to stabilization. This result shows that the isolation of the interferometer chamber is perfect in the sense of keeping the stabilization for long time durations. Considering the time needed for taking the image of the fringes for 3 wavelengths is about 5 minutes for one gauge block measurement, this long time duration of 2 hours having no temperature drift is quite sufficient.

According to international standards, the interferometer would measure the length of blocks at a temperature close to 20 ^{o}C and correct the length to 20 ^{o}C using calculated value of the thermal expansion coefficients (α). In this thesis, the nominal value of α is used but α of different blocks could be different according to lengths because of hardening process. It will be useful to measure the value of α of the blocks, thus an accurate value of it which could be used to accurately correct measured lengths. Further, the measurement of its uncertainty component *($u(\alpha)$)* yields the reduction of uncertainty value of thermal expansion coefficient term as given in chapter 7.2.2.1. Thus, one of the objectives for UME Köster Interferometer is to measure the thermal expansion coefficient (α) and its uncertainty component

u(α). The same interferometer system would measure the lengths of the blocks at different temperatures over the range from 20 ^{o}C to 30 ^{o}C and thus derive an accurate value of α and also *u(α)*.

The refractive index of air is measured inside of the interferometer, and the wavelengths corrections are applied when performing the data processing. In this work, Edlen formula is used by measuring temperature, pressure and humidity values simultaneously. Additionally, a home made refractometer is used for measuring the refractive index also. The result obtained from the Edlen formula is compatible with the result obtained in international measurements. Besides that, the measurement method especially fringe counting system with refractometer could be improved.

We are interested in the double-ended interferometer that does not require wringing process. Thus, some errors coming from wringing can be removed. Firstly, the uncertainty due to wringing is not considered. Consequently a reduction in the total uncertainty is expected. Secondly, when wringing process is realized, according to the definition of International standard 3650, the platen must be made of the same material and surface finish. This is a difficult situation and hence the phase correction should be calculated between platen and block surface. Hence in double-ended interferometre, this phase calculation will not be needed [47]. Additionally, the lengths and the thermal expansion coefficients of different blocks made of different materials (ceramics, tungsten/chrome carbide, cervit etc.) having low thermal expansion coefficient could be measured in this system with no need of wringing.

REFERENCES

[1] Decker J. E., Schödel R. and Bönsch G., 2003, Next-Generation Kösters Interferometer, Proceedings of SPIE, 5190, 14-23

[2] Lewis A. J., 1993, Absolute length measurement using multiple-wavelength phase stepping interferometry, PhD Thesis, University of London

[3] Decker J. E., Miles J. R., Madej A. A., Siemsen R. F., Siemsen K. J., Bonth S., Bustraan K., Temple S. and Pekelsky J. R., 2003, Increasing the range of unambiguity in step-height measurement with multiple-wavelength interferometry-application to absolute long gauge block measurement, Applied Optics, 42, 5670-5678

[4] Doiron T. and Beers S. J., 1995, The Gauge Block Handbook National Institute of standards and Technology (NIST), Monograph 180

[5] Morris A. S., The Principles of Measurement and Instrumentation

[6] Hecht E., 1990, Optics, Addision-Wesley Publishing Company

[7] Hariharan P., 1991, Basics of Interferometry, Academic Press

[8] Cosijns S. J. A. G., Displacement Laser Interferometry with Sub-Nanometer Uncertainty, 2004, PhD thesis, Technische Universiteit Eindhoven

[9] ISO 3650-1978 (E), 1998, ISO Standards Handbook 33: Applied Metrology-Limits, fits and surface properties, 1st Edition

[10] Decker J. E. and Pekelsky J. R., 1997 Gauge Block Calibration by Optical Interferometry at the National Research Council of Canada Measurement Science Conference Pasadena NRC, International Report No. 40002

[11] Hamid R., Sahin E., Celik M., Zucco M., Robertsson L. and Ma L. S., 2004, Absolute frequency measurement and comparison of the UME and the BIPM He-Ne/I2 lasers, Conference digest of Conference on Precision Electromagnetic Measurements (CPEM), UK, 261-262

[12] Ma L. S., Robertsson L., Picard S., Chartier J. M., Karlsson H., Prieto E. and Windeler R. S., 2003, The BIPM Laser Standards at 633 nm and 532 nm simultaneously linked to the SI second using a femtosecond laser in an optical clock configuration, IEEE Transactions on Instrumentation and Measurement, 52, 232-235

[13] Hamid R., Cetintas M. and Celik M., 2004, Observation of Faraday resonances on the S-D two-photon transition of Rb atoms, Physical Review A, 70, 025805/1

[14] Erdoğan C., 2004, 532 ve 1064 nm Dalga Boylarında Optik Frekans Standardının Oluşturulması ve Endüstriyel Uygulamaları, MSc. Thesis, Gebze Yüksek Teknoloji Enstitüsü

[15] Çelik M., 2000, Cooling of Cs Atoms by ECDL (External Cavity Diode Lasers) MSc. Thesis, Gebze Yüksek Teknoloji Enstitüsü

[16]Çetintaş M., 2003, Rubidyum Atomlarında Doğrusal Olmayan Lazer Spektroskopisi ve Metrolojik Uygulamaları, PhD. Thesis, Gebze Yüksek Teknoloji Enstitüsü

[17] Xu Y., Atherton P. D., Hicks T. R., McConnell M. and Rhead P., Quensgate Instruments Ltd, Bracknell, England

[18] Catalog of The Digital Piezo Translator, Queensgate Instruments

[19] Hughes E. B., 1993, Measurement of the linear thermal expansion coefficient of gauge blocks by interferometry, Proc. SPIE, 2088, 179-189

[20] Groot M., 1996, Surface temperature measurement with contact thermometers, High Temperatures-High Pressures, 29, 591-602

[21] Morice R., Andras E., Devin E. and Kovacs T., 2001, Contribution to the calibration and the use of surface temperature sensors, TEMPMEKO, 1111-1136

[22] Pook, J., 1988, Control and Instrumentation, Choosing surface temperature sensors, 20, 75

[23] Quinn T. J., 1990, Temperature Academic Press Inc., San Diego, CA 92101

[24] Mangum B. W., 1983, Triple Point of Succinonitrile and its use in the calibration of thermistor thermometers, Review of Scientific Instruments, 54, 1687-1692

[25] Lewis A. J., 1994, Measurement of length, surface from thermal expansion coefficient of length bars up to 1.5 m using multiple-wavelength phase-stepping interferometry, Measurement Science and Technology, 5, 694-703

[26] Darnedde H., 1992, High precision calibration of long gauge blocks using the vacuum wavelength comparator, Metrologia, 29, 349-359

[27] Thalmann R. 1995, Intercomparison of Thermal Expansion Measurements, EUROMET Project 275

[28] Okaji M., Yamada N. and Moriyama H., 2000, Ultra-precise thermal expansion measurements of ceramic and steel gauge blocks with an interferometric dilatometer, Metrologia, 37, 165-171

[29] Demtröder W., 1996, Laser Spectroscopy 2nd edn (New York: Springer)

[30] Edlèn B., 1966, The Refractivity of Air, Metrologia, 2, 71-80

[31] Edlèn B., 1953, The Dispersion of Standard Air, J. Opt. Soc. Am., 43, 339-344

[32] Birch K. P. and Downs M. J., 1988, The Results of a Comparison Between Calculated and Measured Values of the Refractive Index of Air, J. Phys. E: Sci. Instrum., 21, 694-695

[33] Birch K. P. and Downs M. J., 1989, Error Sources in the Determination of the Refractive Index of Air, Applied Optics, 28(5), 825-826

[34] Birch K. P. and Downs M. J., 1993, An Updated Edlèn Equation for the Refractive Index of Air, Metrologia, 30, 155-162

[35] Bönsch G. and Potulski E., 1998, Fit of Edlèn's Formulae to Measured Values of the Refractive Index of Air, SPIE Vol. 3477, 62-67

[36] Birch K. P., Reinboth F., Ward R. E. and Wilkening G., 1993, The effect of Variations in the Refractive Index of Industrial Air upon the Uncertainty of Precision Length Measurement, Metrologia, 30, 7-14

[37] Erickson K. E., 1962, J. Opt. Soc. Am., 52, 777-780

[38] Robinson D. W., Reid G. T., 1993, Interferogram Analysis, Institute of Physics Publishing

[39] Takeda M., Ina H. and Kobayashi S., Opt. Soc. Am., 72, 156.

[40] Decker J. E., Miles J. R., Madej A. A., Siemsen R. F., Siemsen K. J., Bonth S., Bustraan K., Temple S. and Pekelsky J. R., 2003, Increasing the range of unambiguity in step-height measurement with multiple-wavelength interferometry-application to absolute long gauge block measurement, Applied Optics, 42, 5670-5678

[41] Decker J. E. and Pekelsky J. R., 1997, Gauge Block Calibration by Optical Interferometry at the National Research Council of Canada, California, NRC International Report No. 40002

[42] Siemsen K. J., Siemsen R. F., Decker J. E., Marmet L. and Pekelsky J. R., 1996, A multiple frequency heterodyne technique for the measurement of long gauges, Metrologia, 33, 555-563

[43] Zhao Y., Zhou T. and Li D., 1999, Heterodyne Absolute Distance Interferometer with a Dual-Mode HeNe Laser, Opt. Eng., 38(2), 246-249

[44] Decker J. E. and Pekelsky J. R., 1997, Uncertainty Evaluation for the Measurement of Gauge Blocks by Optical Interferometry, Metrologia, 34, 479-493

[45] Decker J. E., Ulrich A. and Pekelsky J. R., 1998, Uncertainty of Gauge Block Calibration by Mechanical Comparison: A worked Example for Gauge Blocks of Dissimilar Materials", SPIE, San Diego, California, 3477, 225-246

[46] Downs M. J. and Birch K. P., 1983, Bi-directional fringe counting interference refractometer, Precision Engineering Seminar, 5, 105-110

[47] Ishii Y. and Seino S., 1998, New Method for Interferometric Measurement of Gauge Blocks without wringing onto a Platen, Metrologia, 35, 67-73

APPENDIX A

DETAILED TECHNICAL PROPERTIES OF THE INSTRUMENT USED IN INTERFEROMETER

Fibers
Supplier: OzOptics
Specifications:
NA:0.11, Core: 3.5 μm, Cladding: 125 μm, length :25 m for 532 nm laser
NA:0.11, Core: 4 μm, Cladding: 125 μm, length :25 m for 633 nm laser
NA:0.11, Core: 5 μm, Cladding: 125 μm, length :25 m for 778 nm laser

Laser to Fiber Coupler
Supplier: OzOptics
Part No: HPUC-23-532-S-3.9AS-11 for 532 nm laser
HPUC-23-633-S-6.2AS-11 for 633 nm laser
HPUC-23-780-S-6.2AS-11 for 778 nm laser

WDM (Wavelength Division Multiplexer)
Supplier: OzOptics
Part No: WDM-13P-1111-532/633/780-3.5/125,4/125,5/125,4/125-SSSS-40-3S3S3S3S-3-25-SP

Collimating Lens
Supplier: Schott Lithotec AG
Specifications:
Achromat Doublet for 532 nm, 633 nm and 778 nm
Difference of focal length for different wavelengths < 0.6 mm
Focal Length: 1500 mm
Diameter: 100 mm, Thickness: 13 mm
Glass type: BALF5
Coating: CaF_2

De-Collimating Lens
Supplier: Schott Lithotec AG
Specifications:

Achromat Doublet for 532 nm, 633 nm and 778 nm
Difference of focal length for different wavelengths < 0.6 mm
Focal Length: 1000 mm
Diameter: 100 mm, Thickness: 13 mm
Glass type: BALF5
Coating: CaF_2

Imaging Lens
Supplier: Schott Lithotec AG
Specifications:

Achromat Doublet for 532 nm, 633 nm and 778 nm
Difference of focal length for different wavelengths < 0.6 mm
Focal Length: 140 mm
Diameter: 33 mm, Thickness: 7 mm
Glass type: BAF5
Coating: CaF_2

Kösters Interference Double Prisms
Supplier: B.Halle Nachfl.GmbH
Specifications:

The flatness of the effective surfaces is λ/10
The angles of the prism halves: 30^0, 60^0 and 90^0
Dimension tolerance: ± 0.15 mm
Angular accuracy: ± 1'
Angular equality: ± 5'' (25 μrad)
Material: Fused Silica
Based dimensions: 70mmx70 mm
Coatings: AR<1% for 532 nm, 633 m and 778 nm for the entrance and exit faces
R=T=45% for 532 nm, 633 m and 778 nm, semi-transparent coated for one long cathetus side
Surface Quality: 40-20 scratch and dig

Reference Mirrors
Supplier: Melles Griot
Specifications:

Material: Fused Silica
Dimensions: 60 x 60 mm for horizontal mirror
80 x 80 mm for 45^0 mirror
Thickness: 9 mm
Flatness: λ/20
Surface Quality: 40-20 S-D
Coating: Side 1: R < 95 % @500-800 nm/ 45^0 and 90^0
Side 2: AR<1 % @500-800 nm/ 45^0 and 90^0

DPT (Digital Piezo Translator) Controlled Stages

Supplier: Sifam Instruments Limited

Part No: NPS-Z-15A (Actuator)

NPS3220 (Controller)

Specifications:

Active axis: one dimensional as vertical
Travel Range: 5-15 μm (total)
Repeatability: better than 1 nm
Resolution (Position Noise): 0.1 nm or better
Length: 40-55 mm
Diameter: 30-40 mm
Max Load: 0.5 kg
Non-Linearity: 0.01% or better
Rotational Error: 0.15 arcsec / 1 μm or better
Controller: position servo control, RS 232 computer control

PZT (Piezo Electric Transducer) Controlled Optical Mounts and Stages

Supplier: New Focus

Part No: 8809 (Optical mounter)

8071 (Stages)

8732 (Multi-Axis Driver)

8620 (Control hand pad)

Specifications:

Optical Mounter:

Motorized Axis: 3
Angular Resolution: 0.7 μrad

Stages:

Degrees of Freedom: x, y, θ_x and θ_y
Angular Resolution: 0.7 μrad
Linear Resolution: 30 nm
Angular Travel Range: 8^{0}
Linear Travel Range: 3 mm

Controller: RS-232, GPIB, Control Pad

APPENDIX B

SOME PICTURES OF UME (National Metrology Institute)
HOME MADE KOSTER INTERFEROMETER

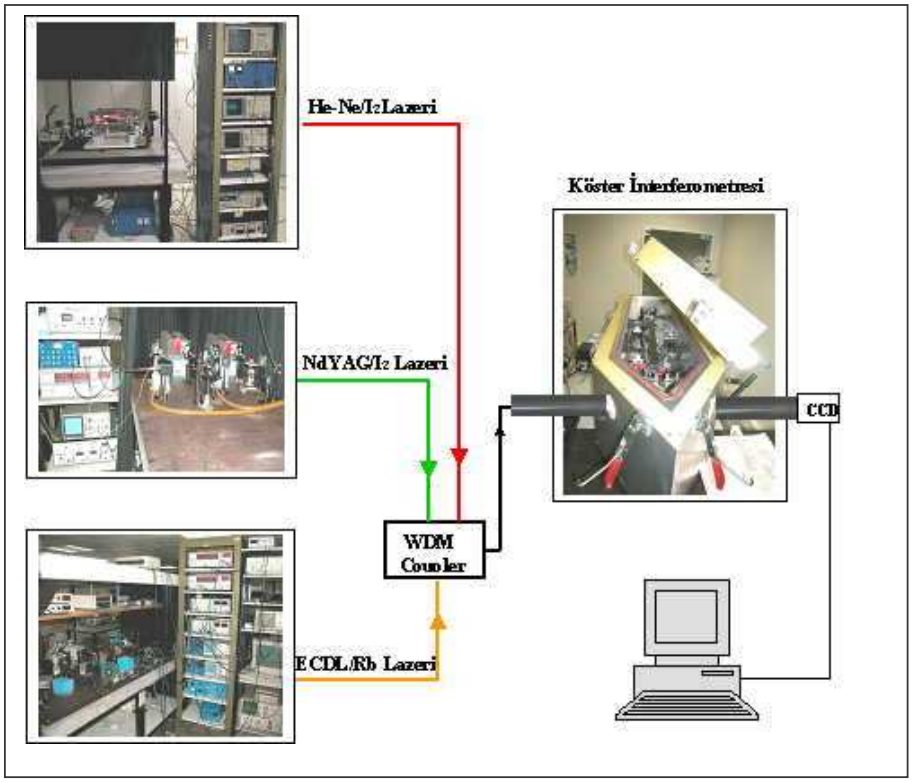

Figure 1. The Köster Interferometer and Stable Laser Systems

Figure 2. The mechanical design and cross-section of Köster Interferometer

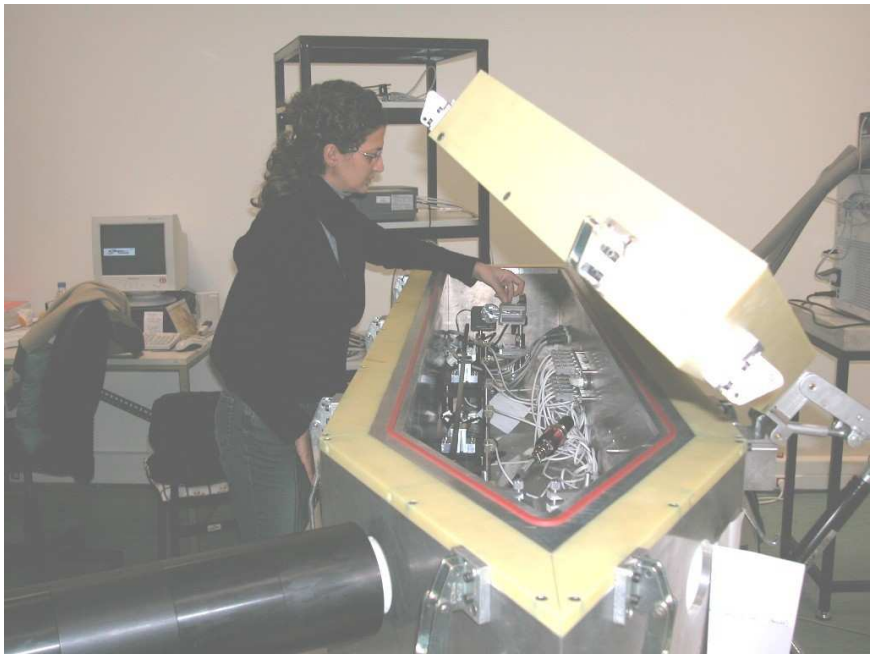

Figure 3. Inside of the Koster interferometer

APPENDIX C

PUBLICATIONS

This appendix contains copy of the paper published by the author, relevant to the thesis. The temperature stabilization results and construction of the interferometer is given in paper as

1. The temperature stabilization and temperature measurement of a Kösters interferometer, Hamid R., Sendogdu D. and Erdogan C., Meas. Sci. Technol., 16, pp. 2201-2207, 2005

The other national and international proceedings relevant to this thesis are as follows,

2. Köster İnterferometresi'nde Havanın Kırılma İndeksinin Edlen Formülü İle Hesaplanması ve Refraktometre İle Ölçülmesi, Hamid R., Şendogdu D., Erdogan C., 6. Ulusal Optik, Elektro-optik ve Fotonik Çalışma Toplantısı, Aralık 2004
3. Yapılandırılmış Işığın 3-Boyutlu Metroloji Uygulamaları, Birlikseven C., Celik M., Sendogdu D., Sahin E., Hamid R., 6. Ulusal Eskişehir Ölçüm Bilim Kongresi, Eskişehir, 17-18 Kasım 2005
4. The Kösters interferometer for long gauge block length measurements, Hamid R., Sendogdu D. and Erdogan C., in conference digest *of Conference on Precision Electromagnetic Measurements (CPEM*), Italy, 2006
5. Köster İnterferometresi'nde Mastar Blok Uzunluk Ölçümleri ve Kullanılan Veri İşleme Yöntemleri, Şendogdu D., Hamid R., Erdogan C., Birlikseven C., 8. Ulusal Fotonik Çalıştayı, Koç Üniversitesi, İstanbul, Eylül 2006

INSTITUTE OF PHYSICS PUBLISHING MEASUREMENT SCIENCE AND TECHNOLOGY
Meas. Sci. Technol. 16 (2005) 2201–2207 doi:10.1088/0957-0233/16/11/010

The temperature stabilization and temperature measurement of a Kösters interferometer

R Hamid, D Sendogdu and C Erdogan

National Metrology Institute (UME), Scientific and Technical Research Council of Turkey (TÜBİTAK), PO Box 54, 41470 Gebze-Kocaeli, Turkey

E-mail: ramiz.hamid@ume.tubitak.gov.tr

Received 21 April 2005, in final form 28 June 2005
Published 28 September 2005
Online at stacks.iop.org/MST/16/2201

Abstract
In this work, the mechanical design, optical setup and temperature measurement system of a Kösters interferometer are described for the length measurements of long gauge blocks. The temperature variation of 9 mK at 15 °C and 2 mK at 20 °C was measured inside the interferometric chamber using the six air and four surface thermistors. The temperature stability is analysed by using standard deviation and Allan variance statistics.

Keywords: Köster interferometer, gauge block, temperature measurement, thermistor

1. Introduction

In interferometric applications, especially in length measurements for metrological purpose, the temperature measurement and temperature stabilization in the interferometric chamber are highly important. In metrology laboratories, various interferometers have been designed for different purposes, which are still in use [1–5]. For example, in the Length Bar Interferometry at the National Physical Laboratory (NPL) in England, the temperature of the chamber is stabilized to 20.00 °C with an uncertainty of ±0.03 °C [1, 2]. Similarly in a Euromet project [3], the Swiss Federal Office of Metrology (OFMET) achieved a temperature variation of less than 0.01 °C within a temperature range of 10–30 °C with a vacuum interference dilatometer.

The result of temperature measurement in a length interferometer chamber and its uncertainty depend on two main factors. The first factor is the temperature fluctuation inside the interferometer chamber, which is dependent on the design of the instrument, and the second factor is the uncertainty of the sensors used and their measurement methods.

The largest contributing factor to the total uncertainty of length measurements in interferometers is due to the thermal expansion of individual gauge blocks [6]. The thermal expansion uncertainty arises from two uncertainties: the uncertainty in the expansion coefficient (multiplied by the temperature deviation from the reference temperature) and the uncertainty in the temperature measurement (multiplied by the expansion coefficient). When the uncertainty of the gauge block temperature measurement is within 1 mK, then a length uncertainty of 12 nm is observed [7]. Additionally, the measurement of air temperature contributes to the refractive index uncertainty. The laser wavelength is directly dependent on the refractive index inside the chamber. Since this refractive index is obtained by using the temperature, pressure and humidity measurements of the air inside the chamber, these values should be measured very accurately. Besides, the effective thermal and pressure isolation of the chamber gives rise to effective refractive index stabilization.

In this paper, firstly the mechanical design of the interferometric chamber realized at the National Metrology Institute of Turkey (UME) and its opto-mechanical parts are described. Then the temperature measurement system using air and surface thermistors is given. After that, the temperature measurement results and a temperature variation of 2 mK at 20 °C are demonstrated. Finally, a statistical analysis of the temperature measurement results is presented.

2. UME Kösters interferometer

2.1. Thermostat of the Kösters interferometer

A schematic diagram of the cross section of the UME Kösters interferometric chamber (thermostat) is shown in figure 1, in

0957-0233/05/112201+07$30.00 © 2005 IOP Publishing Ltd Printed in the UK

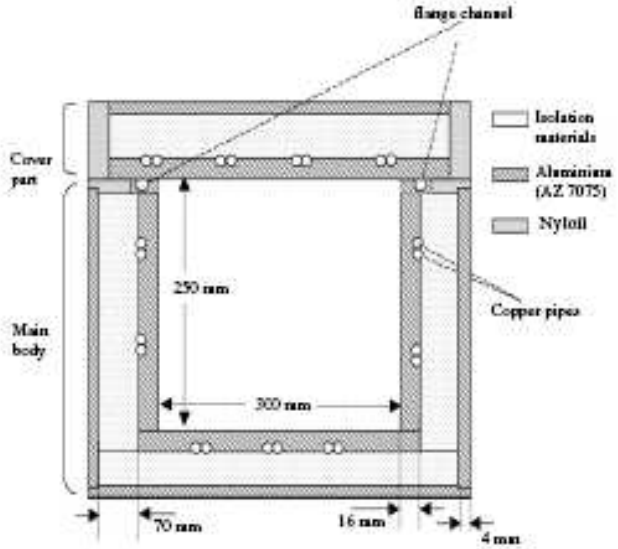

Figure 1. The cross section of the main body (chamber) and cover including aluminium boxes, isolation materials, Nylon and copper pipes (the diagram is not to scale).

which the cross-sectional internal dimensions of the chamber are 250 mm × 300 mm and the internal length of the chamber is 1750 mm. Similar interferometers have been developed in different metrology laboratories. The design and development of the UME interferometer is based on the design of long gauge block interferometers at NPL [1, 2] and PTB [4]. In particular, the water-circulating system is based on the interferometer at NPL, and the shape of the chamber is based on the interferometer at PTB.

Our interferometric thermostat is constructed as a coaxial box which has an outer thickness of 4 mm and an inner thickness of 16 mm. Different isolation materials, roof mate and glass wool, having different thicknesses, are used between the two boxes, which are separated by 70 mm. The box is made of aluminium (AZ 7075). Temperature stabilization is obtained by circulating water through copper pipes that are placed side by side, over the surface of the inner box including the cover. One of these copper pipes brings the chilled water to the chamber, whereas the other one carries the circulated water away from the chamber. For continuous water flow, a refrigerated circulator with a resolution of 0.1 °C is used. Finally, to prevent air leakage when the cover is closed, a flange channel is formed between the touching parts of the cover and the main body, and a suitable o-ring is placed in the flange channel. Additionally, the cover part can be sealed fully to the main body by its nine different points along the chamber.

Additionally, some tiny holes are drilled through one wall of the chamber to open channels for the cables and pipes. The proper flanges and o-rings are used in these apertures to obtain temperature and pressure isolation. Each flange is utilized for the following measurements and controls: temperature, pressure, humidity, changing of internal gas, obtaining vacuum in the refractometer, control of the digital piezo translator (DPT) installed on the reference mirror, control of the piezo electric transducer (PZT) installed on the second reference mirror and control of the PZT installed on the gauge block holders. PZT and DPT are used for controlling the movement of the mirrors and gauge block accurately and remotely when the cover is closed.

2.2. Optical setup of the Kösters interferometer

The schematic diagram of the optical setup of the interferometer is shown in figure 2. To improve the temperature control and stabilization, the lasers and the charge coupled device (CCD) camera, which can be sources of unwanted heat, are placed outside the chamber. Meanwhile the other necessary optical and opto-mechanical parts, i.e. the mirrors on the reference arm, the Kösters prism, the PZT controlled mirror and gauge block holders, are placed inside the chamber.

The laser beams from three different stable lasers (He–Ne/I_2 [8], Nd:YAG/I_2 [9] and the external cavity diode laser (ECDL) stabilized on Rb atomic transition [10]) are launched into different fibre cables, which are combined by the wavelength division multiplexer (WDM) coupler. The fibre cable at the output of the WDM coupler is connected to the input of the telescope. The laser beam is expanded up to 100 mm by using the collimating telescope and pointed at the inside of the chamber through the input quartz window (80 mm). In the chamber, the laser beam is split into two as reference and measurement arms by using the Kösters prism. The reference beam is reflected from the reference mirrors, whereas the measurement beam is reflected from the platen and the front surface of the gauge block. The reflected beams coming from the two arms are then combined by passing through the Kösters prism. The fringes that form

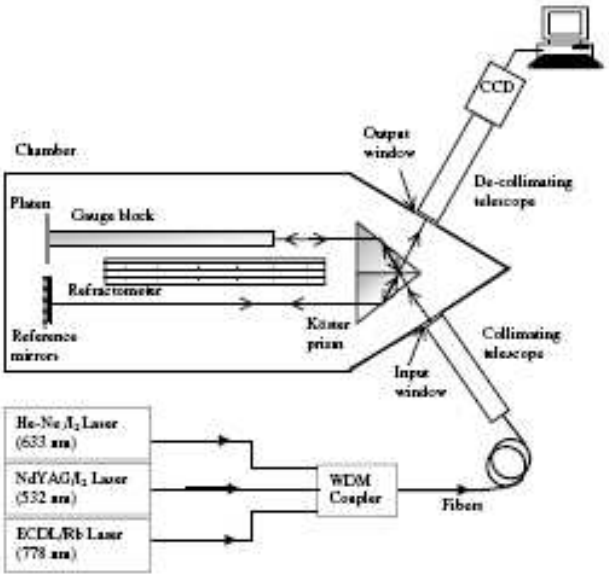

Figure 2. The schematic diagram of the interferometer with optical and opto-mechanical parts.

due to the interference of the two laser beams pass through the output window and then through the de-collimating telescope. Finally, the interference fringes are detected using the PC-controlled CCD camera.

The refractometer seen in figure 2 is used to optically measure the refractive index of the air inside the chamber. Another method for obtaining the refractive index is to use the Edlen formula, which calculates a value based on measurement results using air thermistors, as well as values from the measurements of pressure and humidity inside the chamber [11–13]. The refractive index value is calculated as $1.000\,2623 \pm 3.6 \times 10^{-7}$ through the Edlen formula and measured as $1.000\,267 \pm 6 \times 10^{-6}$ by the refractometer. The results indicate a difference of 5×10^{-6}. Approximately, 15 refractive indices were measured and calculated, and all the differences obtained are in the range of 10^{-6}. We would like to note that a difference in the range of 10^{-7} is observed in the results of other metrology laboratories [11, 13]. This difference of 5×10^{-6} in our refractive index measurement is probably caused by the refractometer, especially from counting of the fringe numbers. However, as the refractive index measurement is not the main subject of this paper, the initial results are presented. Moreover, the development of the refractive index measurement system and efforts to minimize the difference in the results are still in progress. Thus, for each of the methods, achieving accurate temperature stability and uniformity, and preventing turbulence of the air inside the chamber are important.

3. Temperature measurement system

For accurate temperature control and measurement of both the air inside the chamber and the surface of the gauge block,

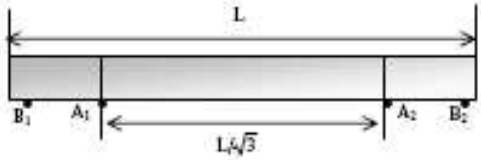

Figure 3. The placements of the Airy points and surface temperatures of the 1 m gauge block. L is the length of the gauge block. A_1 and A_2 are the Airy points. Two surface thermistors are placed at the Airy points. B_1 and B_2 are the placements of the other two surface thermistors at points 10 cm away from the Airy points.

thermistors are used because of their higher sensitivities. When comparing their sensitivity with respect to a platinum resistance thermometer (Pt100), the sensitivity of a thermistor is about 4% K^{-1}, whereas that of the Pt100 is approximately 0.4% K^{-1} [7]. In our system, a total of ten thermistors is used. Four of them are used for the surface temperature measurement of the gauge block and the other six are used for the air temperature measurement inside the chamber.

The gauge block is placed horizontally inside the chamber and its length is measured in that position. The block is supported at two points named the Airy points as shown in figure 3. In the measurement of its surface temperature, the platen is not wrung to the block, so the block is supported exactly at the Airy points. Support at these points minimizes sagging of the block. The distance between the Airy points is calculated by dividing the length (L) of the block by $\sqrt{3}$ and it is engraved on the gauge block's surface by the block's suppliers [1]. For the temperature measurement of the gauge block, two surface thermistors are installed separately inside the two block supporters, which are placed at the Airy points.

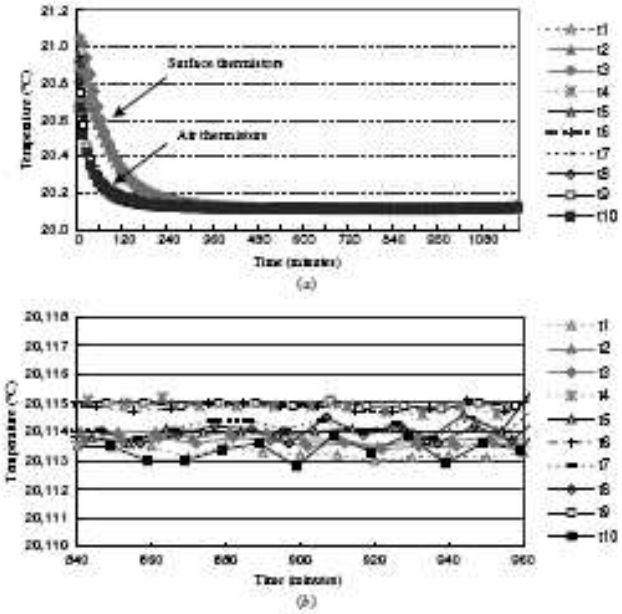

Figure 4. The temperature readings from all thermistors (the first four are surface thermistors whereas the other six are air thermistors) at about 20 °C for (*a*) about 20 h, (*b*) about 2 h. The temperature fluctuations of all thermistors remain in the range of 2 mK.

One of the other two surface thermistors is placed 10 cm to the left of the first Airy point and the other one is placed 10 cm to the right of the second Airy point. All of the surface thermistors are attached to the gauge block at the bottom side of the block. Since the surface roughness of the thermistors reduced at the production stage and additionally thermal contact is assumed to be good enough to sense and care must be given not to damage the surface of the block, it is preferred that thermal grease not be used between the contact surfaces during the temperature measurement in this work. Additionally, the back (non-contact) sides of the surface thermistors are covered with insulation in the production stage to reduce the effects of the environment. Furthermore, a spring mechanism is placed in the thermistor holders to increase the contact pressure [7, 14, 15]. The air thermistors are placed at different points inside the chamber along the gauge block.

The temperature measurement system is intended for precise temperature measurements in the range of 15–25 °C with an accuracy of 0.002 °C. Nominal resistance of the thermistors at 20 °C is 12 ± 1 kΩ. The resistances of the thermistors are measured with a Wheatstone bridge. The sensitivity at 20 °C is 0.475 ± 0.025 kΩ °C^{-1}. This corresponds to a sensitivity value of 3.9 ± 0.2% K^{-1}.

Using the measurement results of thermistor resistances, the temperature t is calculated by the formula [16]

$$t = \frac{1}{A + B\ln R + C(\ln R)^3} - 273.15 \qquad (1)$$

where t is the temperature in °C, R is the thermistor resistance in ohms and A, B and C are the individual calibration coefficients for each thermistor.

The thermistors are calibrated using three different fixed points: GaIn eutectic alloy at 15.646 °C, GaSn eutectic alloy at 20.482 °C and Ga at 29.765 °C. The calibration coefficients of A, B and C in equation (1) are calculated with these fixed points for the indicated thermistor. The most reproducible constant temperature of the eutectic alloy cells is their melting temperature, and the cells enable us to have phase transitions of at least 3 h.

The fixed points used in this work are calibrated in the Temperature Laboratory at UME with a standard platinum resistance thermometer (SPRT), which is traceable to the ITS90 scale. Each thermistor is calibrated using these fixed points (GaIn, GaSn and Ga). The expanded ($k = 2$) uncertainty of each thermistor, which includes the uncertainties of fixed points, is 2 mK.

The resistance of each thermistor is measured through a PC controlled system. The measurement results are calculated by a special computer program that includes the individual calibration coefficients of thermistors. Additionally, the time dependence of the temperature for each thermistor is obtained automatically in graphical and data formats.

4. The results of temperature measurements

The results of a typical temperature measurement are shown in figure 4(*a*). During this measurement, the temperature inside the laboratory is 21.0 ± 0.5 °C. The temperature of the circulator is set to 20 °C so that the water circulates at 20 ± 0.1 °C along the copper pipes. The temperature measurement is realized for about 20 h. The system reached

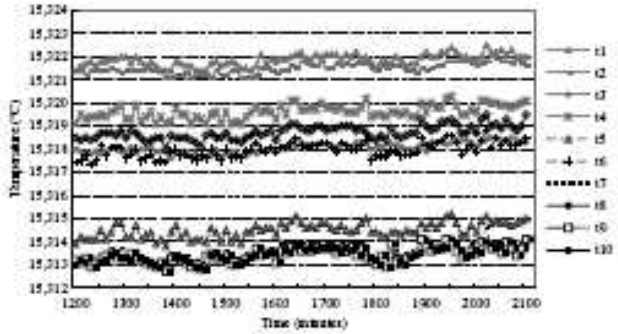

Figure 5. The temperature readings from all thermistors (the first four are surface thermistors whereas the other six are air thermistors) at about 15 °C for about 15 h. The temperature fluctuations of all thermistors remain in the range of 9 mK.

the temperature of about 20 °C at the end of the first 4 h and achieved stability after the first 14 h. The first four thermistors are surface thermistors, whereas the other six are air thermistors. As shown in figure 4(*a*), the time-dependent change of the temperature value for air thermistors is faster than the value for surface thermistors. This is due to the fact that the air thermistors measure the air temperature inside the interferometric chamber, whereas the surface thermistors measure the temperature of the gauge block, which is mounted on the two Airy points in the interferometric chamber. This result shows that the temperature of the gauge block reaches the set temperature later than the air temperature inside the chamber due to its mass and its lower efficiency of thermal contact with the chamber wall.

As shown in figures 4(*a*) and (*b*), after the temperature stabilization of the chamber and gauge block (about 840 min), the temperature variation of all thermistors remains in the range of 2 mK for about 2 h. In figure 4, the curves t1, t2, t3 and t4 correspond to the measurement results of the surface temperature, whereas curves t5–t10 correspond to the measurement results of the air temperature. As is seen in figure 4(*b*), the temperature variations of each thermistor separately are smaller than 1 mK for the same time interval.

A similar measurement is realized by setting the circulator's temperature to 15 °C. If we were to calculate the thermal expansion coefficient of the gauge block [1–3, 6, 17], the temperature of the chamber would be stepped along a range of 15–25 °C in definite increments. However in this study, the measurement is realized only at 15 °C, in order to test the system at a different temperature from 20 °C. The temperature measurement results at 15 °C are presented in figure 5. After temperature stabilization, the temperature variation of all thermistors remains in the range of 9 mK. It is observed that the temperature variation is about 4 mK for surface thermistors, whereas it is about 6 mK for air thermistors. In comparing the results in figures 4 and 5, away from room temperature, the temperature variation in the chamber becomes inhomogeneous due to the influence of the temperature gradient of the communication cables and connectors (flange) on the chamber wall. As deduced from the graph in figure 5, a small drift about 1 mK is observed over 15 h.

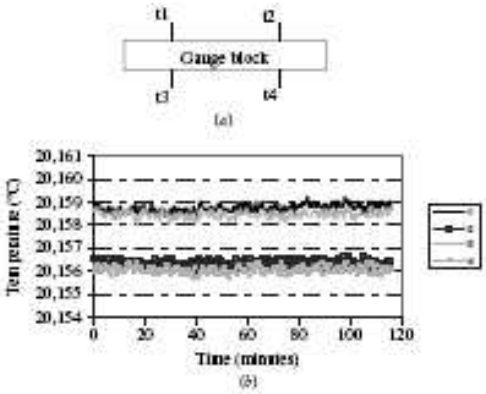

Figure 6. (*a*) The placements of the surface thermistors for examining the temperature difference of the upper and lower parts of the gauge block, (*b*) the temperature measurement results at about 20 °C for about 2 h. The temperature difference, which corresponds to the temperature gradient of the upper and lower parts of the block, between the sensors (t1 and t3, t2 and t4) is smaller than 0.5 mK.

Additional experiments are conducted to examine the temperature difference of the upper and lower parts of the gauge block. The measurements are done at 20 °C and the results are shown in figure 6. In this measurement, two surface thermistors are located under the block at the Airy points, whereas the other two are placed on top of the block at points opposite to the Airy points (figure 6(*a*)). The result of the temperature measurement for 2 h, after the stabilization of the temperature inside the chamber, is shown in figure 6(*b*). The temperature values of the two sensors (t1 and t3) are close, exhibiting a difference smaller than 0.5 mK. A similar result is seen for the other two sensors (t2 and t4). Therefore, the temperature of the upper part of the block is quite close to that of the lower part of the block. Meanwhile, the temperature difference between the two Airy points is about 2 mK.

To investigate the influence of the platen on the temperature gradient of the gauge block, similar experiments

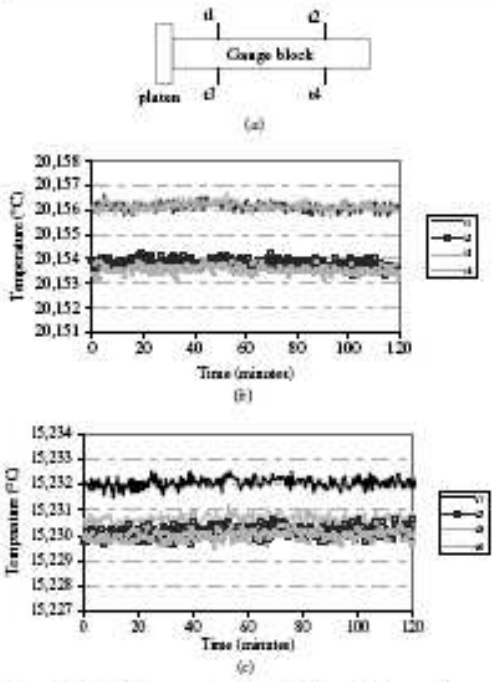

Figure 7. (*a*) The placements of the surface thermistors over the gauge block with the platen for the influence of the platen on the temperature gradient of the block, (*b*) the temperature measurement results at 20 °C and (*c*) at 15 °C for 2 h. The difference of the measured temperature values at the Airy points in the experiments at 20 °C or 15 °C with or without the platen is about 2 mK.

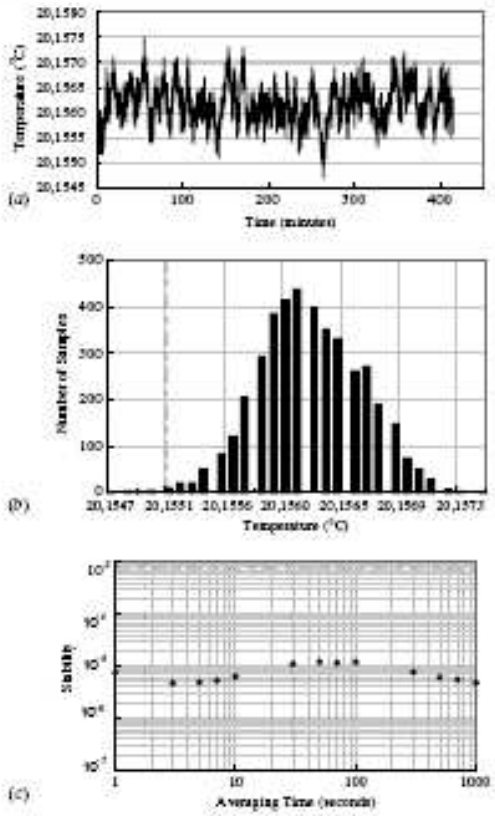

Figure 8. (*a*) The temperature data for one thermistor at 20 °C for about 7 h, (*b*) the histogram graph of the measurement and (*c*) the stability graph of Allan variance analysis.

are conducted while the platen is wrung to the gauge block. The dimensions of the platen used in this experiment are 50 mm × 35 mm × 10 mm. The measurements are done at 20 °C and 15 °C. The sensors are mounted on opposite sides at the Airy points of the gauge block (figure 7(*a*)). The results of the temperature measurement for 2 h, after the stabilization of the temperature inside the chamber, are shown in figures 7(*b*) and (*c*) for temperatures of 20 °C and 15 °C, respectively. As seen from figure 7(*b*), the temperature difference of the opposite sensors (t1–t3 or t2–t4) is about 0.5 mK, whereas the temperature difference between the Airy points is about 2 mK. In the experiment conducted at 15 °C (figure 7(*c*)), the temperature difference of the opposite sensors and of the Airy points is observed to be about 2 mK. We would like to note that when comparing the measurement results with or without the platen, a steeper temperature gradient is not observed between the Airy points.

In this experiment, the temperature measurement for each thermistor is realized during an average time interval of 1 min and thus, single measurement data for each thermistor are taken every 10 min because there are ten thermistors. In order to investigate the temperature stability in more detail, an additional measurement is realized using an air thermistor located at the centre of the chamber. Within a span of 7 h, we measure the temperature of the chamber using the thermistor at 1 s average time intervals. The graph of temperature versus time is shown in figure 8(*a*). The histogram of this measurement is shown in figure 8(*b*). This experimental result shows a symmetrical distribution of temperature fluctuation around the mean value of 20.1562 °C with a peak-to-peak temperature fluctuation of less than 3.0 mK and a standard deviation value of 0.4 mK.

The stability of temperature measurement results as shown in figure 8(*a*) is evaluated using Allan variance statistics [18]. Figure 8(*c*) shows the stability and the root Allan variance value as a function of the average time. When the temperature of the chamber is stabilized, the measured Allan variance of the temperature fluctuation shows a temperature stability of about 10^{-5} for average times from 1 s to 1000 s. As shown in figure 8(*a*), the white and flicker noise is dominant, whereas the drift is comparatively small. So non-decreasing variance as a function of averaging time in figure 8(*c*) will be explained as long-term stability that is limited and determined by the flicker noise and not the long-term drift.

5. Conclusion

An accurate temperature controlled Kösters interferometer for long gauge blocks is developed. A temperature variation of about 9 mK at 15 °C and 2 mK at 20 °C is obtained. This temperature variation is measured inside the interferometer by using six air and four surface thermistors with a PC controlled system.

The temperature measurement is analysed for one of the thermistors by using Allan variance and standard deviation statistics. A temperature stability of 2×10^{-5} for average times ranging from 1 s to 1000 s is obtained. The standard deviation of this 7 h measurement is obtained as 0.4 mK.

The experimental results presented in this work will be important for the length measurements of long gauge blocks. The length of the gauge block depends on the stabilities of the temperature and refractive index inside the chamber. A smaller uncertainty in temperature and refractive index measurements minimizes the total uncertainty.

Acknowledgment

The authors would like to thank H I Emre for his technical assistance.

References

[1] Lewis A J 1993 Absolute length measurement using multiple-wavelength phase stepping interferometry *PhD Thesis* University of London

[2] Lewis A J 1994 Measurement of length, surface from thermal expansion coefficient of length bars up to 1.5 m using multiple-wavelength phase-stepping interferometry *Meas. Sci. Technol.* 5 694–703

[3] Thalmann R 1995 Intercomparison of thermal expansion measurements *EUROMET Project* p 275

[4] Damedde H 1992 High precision calibration of long gauge blocks using the vacuum wavelength comparator *Metrologia* 29 349–59

[5] Haitjema H and Kotte G 1998 Long gauge block measurements based on a Twyman–Green interferometer and three stabilized lasers *Proc. SPIE* 3477 25–34

[6] Hughes E B 1993 Measurement of the linear thermal expansion coefficient of gauge blocks by interferometry *Proc. SPIE* 2088 179–89

[7] Groot M 1996 Surface temperature measurement with contact thermometers *High Temp.—High Pressures* 29 591–602

[8] Hamid R, Sahin E, Celik M, Zucco M, Robertsson L and Ma L S 2004 Absolute frequency measurement and comparison of the UME and the BIPM He–Ne/I_2 lasers *Conference Digest of Conference on Precision Electromagnetic Measurements (CPEM) (UK)* pp 261–2

[9] Ma L S, Robertsson L, Picard S, Chartier J M, Karlsson H, Prieto E and Windeler R S 2003 The BIPM Laser Standards at 633 nm and 532 nm simultaneously linked to the SI second using a femtosecond laser in an optical clock configuration *IEEE Trans. Instrum. Meas.* 52 232–5

[10] Hamid R, Cetintas M and Celik M 2004 Observation of Faraday resonances on the S–D two-photon transition of Rb atoms *Phys. Rev.* A 70 025805/1-4

[11] Downs M J and Birch K P 1983 Bi-directional fringe counting interference refractometer *Precis. Eng. Semin.* 5 105–10

[12] Tianchu L 1995 Design principles for laser interference refractometers *Measurement* 16 171–6

[13] Bönsch G and Potulski E 1998 Measurement of the refractive index of air and comparison with modified Edlen's formulae *Metrologia* 35 133–9

[14] Morice R, Andras E, Devin E and Kovacs T 2001 Contribution to the calibration and the use of surface temperature sensors *TEMPMEKO* pp 1111–6

[15] Pook J 1988 Choosing surface temperature sensors *Control Instrum.* 20 75–6

[16] Mangum B W 1983 Triple point of succinonitrile and its use in the calibration of thermistor thermometers *Rev. Sci. Instrum.* 54 1687–92

[17] Okuji M, Yamada N and Moriyama H 2000 Ultra-precise thermal expansion measurements of ceramic and steel gauge blocks with an interferometric dilatometer *Metrologia* 37 165–71

[18] Demtröder W 1996 *Laser Spectroscopy* 2nd edn (New York: Springer)

CURRICULUM VITAE

PERSONAL INFORMATION

Surname, Name: Şendoğdu Çuhadar Damla
Nationality: Turkish (TC)
Date and Place of Birth: 17 Kasım 1972, Erzincan
Marital Status: Married
Phone: +90 262 679 50 00
Fax: +90 262 679 50 01
email: damla.sendogdu@ume.tubitak.gov.tr

EDUCATION

Degree	Institution	Year of Graduation
MS	METU Physics, Ankara	2000
BS	Hacettepe Üniversity Physics Engineering, Ankara	1996

WORK EXPERIENCE

Year	Place	Enrollment
2002- Present	Tubitak UME	Researcher
1999-2001	METU Department of Physics	Research Assistant

PUBLICATIONS

1. Lazer Tek Çizgi Tarama Yöntemi ile 3 Boyutlu Cisimlerin Görüntülerinin Elde Edilmesi, Cuhadar D., Alaçakır A., Türk Fizik Derneği, 18. Fizik Kongresi, Adana, Ekim 1999
2. Köster İnterferometresi'nde Havanın Kırılma İndeksinin Edlen Formülü İle Hesaplanması ve Refraktometre İle Ölçülmesi, Hamid R., Şendoğdu D., Erdoğan C., 6. Ulusal Optik, Elektro-optik ve Fotonik Çalışma Toplantısı, Aralık 2004
3. The Temperature Stabilization and Temperature Measurement of a Kösters Interferometer, Hamid R., Sendogdu D. and Erdogan C., Meas. Sci. Technol., 16, pp. 2201-2207, 2005
4. Yapılandırılmış Işığın 3-Boyutlu Metroloji Uygulamaları, Birlikseven C., Çelik M., Şendoğdu D., Sahin E., Hamid R, 6. Ulusal Eskişehir Ölçüm Bilim Kongresi, Eskişehir, 17-18 Kasım 2005
5. The Kösters interferometer for long gauge block length measurements, Hamid R., Sendogdu D. and Erdogan C., in conference digest of Conference on Precision Electromagnetic Measurements (CPEM), Italy, 2006
6. Köster İnterferometresi'nde Mastar Blok Uzunluk Ölçümleri ve Kullanılan Veri İşleme Yöntemleri, Şendoğdu D., Hamid R., Erdoğan C., Birlikseven C., 8. Ulusal Fotonik Çalıştayı, Koç Üniversitesi, İstanbul, Eylül 2006